Measurement of -meson production in proton–proton and Pb–Pb collisions at $\sqrt{}$s_(NN) = 5.02 TeV with the ALICE experiment at the LHC

Florian Damas

To cite this version:

Florian Damas. Measurement of -meson production in proton–proton and Pb–Pb collisions at $\sqrt{}$s_(NN) = 5.02 TeV with the ALICE experiment at the LHC. Nuclear Experiment [nucl-ex]. École nationale supérieure Mines-Télécom Atlantique, 2021. English. NNT : 2021IMTA0214 . tel-04041433

HAL Id: tel-04041433
https://theses.hal.science/tel-04041433

Submitted on 22 Mar 2023

UNIVERSITE MATIERE
BRETAGNE MOLECULES
LOIRE ET MATERIAUX

IMT Atlantique
Bretagne-Pays de la Loire
École Mines-Télécom

THÈSE DE DOCTORAT DE

L'ÉCOLE NATIONALE SUPÉRIEURE MINES-TÉLÉCOM ATLANTIQUE
BRETAGNE PAYS DE LA LOIRE – IMT ATLANTIQUE
COMUE UNIVERSITÉ BRETAGNE LOIRE

ÉCOLE DOCTORALE N° 596
Matière, Molécules, Matériaux
Spécialité : Physique Subatomique et Instrumentation Nucléaire

Par
Florian DAMAS

Measurement of Υ-meson production in proton–proton and Pb–Pb collisions at $\sqrt{s_{\mathrm{NN}}}$ = 5.02 TeV with the ALICE experiment at the LHC

Thèse présentée et soutenue à Gif-sur-Yvette, le 02 février 2021
Unité de recherche : SUBATECH et Département de Physique Nucléaire de l'Irfu
Thèse n° 2021IMTA0214

Composition du Jury :

Président	**Pol-Bernard GOSSIAUX**	Professeur, IMT Atlantique, SUBATECH
Rapporteurs	**Elena GONZALEZ FERREIRO**	Professeure, Universidade de Santiago de Compostella, IGFAE
	Raphael GRANIER DE CASSAGNAC	Directeur de recherche CNRS, École Polytechnique, LLR
Examinatrices	**Giulia MANCA**	Maître de conférences, Università degli Studi di Cagliari, INFN
	Silvia NICCOLAI	Directrice de recherche CNRS, Université Paris-Saclay, IJCLab
Directeurs	**Javier CASTILLO CASTELLANOS**	Chercheur-Ingénieur, CEA, Irfu
	Gines MARTINEZ GARCIA	Directeur de recherche CNRS, SUBATECH
Encadrant	**Laurent APHECETCHE**	Chargé de recherche CNRS, SUBATECH

Contents

Chapter 1

Probing QCD properties with quarkonia

The production of quarkonia is commonly advertised as a key observable to study QCD properties in the laboratory. In high-energy nuclear collisions, interactions between heavy-quark pairs and their environment affect the formation of bound states, potentially leading to the suppression of their production. Measuring the modification of yields gives a privileged access to strongly-interacting matter features. This first chapter aims to introduce the theoretical background as well as the main physics motivations for this thesis.

1.1 Quantum chromodynamics

1.1.1 Overview of particle physics

At the subatomic scale, the behaviour of matter can be explained by the interaction of fermions via the exchange of vector bosons. The underlying laws of physics are formalised in the *standard model* of particle physics summarised with Figure 1.1 and reviewed by the Particle Data Group [1].

The elementary components of matter form two categories. Leptons are grouped into three generations of doublets consisting of an electric charge and a neutrino. A lepton quantum number is assigned to each family (electronic, muonic and tauonic) and conserved within the standard model[†]. Consequently, the leptons and anti-leptons from a same generation are always created in pairs. Quarks come in six different types called *flavours*: up, down, strange, charm, bottom and top – from lightest to heaviest – and carry a fraction of the elementary electric charge. Other properties are highlighted in Section 1.1.2. The quarks are the only particles sensitive to the four fundamental interactions:

- The strong interaction is unique to quarks and gluons and is discussed in the next part. One of the most important features is the residual force binding protons and neutrons together thus ensuring the cohesion of the latter inside atomic nuclei.

[†] Lepton number conservation is violated by neutrino oscillations between generations, implying that neutrinos cannot be massless [2].

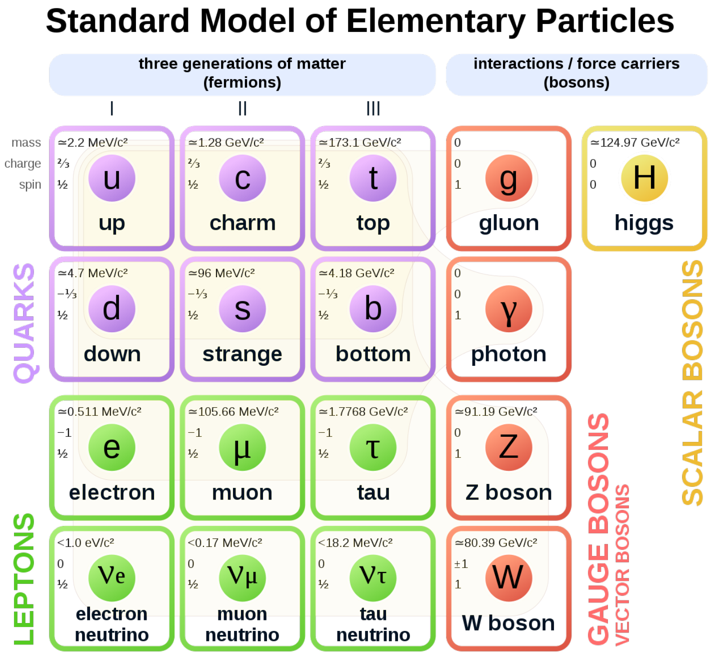

Figure 1.1: The standard model of particle physics in one picture. The anti-fermions are not represented. Figure taken from Wikipedia.

- Electric charges interact via the exchange of photons, the electromagnetism force-carrier. Quantum electrodynamics (QED) results from the quantisation of the electromagnetic fields and inspired the development of other quantum field theories [3].

- The weak interaction concerns all fermions. Among other phenomena, it is responsible for the radioactive β decay. The electroweak theory [4] unifies the weak and electromagnetic interactions in a single framework.

- Any massive body is source of gravitational field. Gravity is mathematically described by the general theory of relativity. No satisfactory quantum formulation exists to date.

In addition to these interactions, the Brout-Englert-Higgs mechanism gives rise to the mass of elementary particles [5, 6]. The existence of a scalar Higgs boson is a signature of this phenomenon and its experimental observation completes a self-coherent picture. Despite the success of the Standard Model, many fundamental questions are still to be resolved [7].

1.1.2 A theory of the strong interaction

Quantum chromodynamics (QCD) is the theory describing the dynamics of *colour-charged* particles, i.e. the quarks and gluons, together referred to as partons. The colour charge represents the gauge associated to the SU(3) symmetry group, with the gluon as mediator. Hence, (anti-)quarks come in three (anti-)colours and there exist 8 massless gluons carrying a colour and an anti-colour charge[§].

To obey local gauge invariance, the QCD Lagrangian can be read as

$$\mathcal{L}_{\text{QCD}} = -\frac{1}{4} G^{C}_{\mu\nu} G^{\mu\nu,C} + \sum_{\text{flavours}} \overline{\psi}_a ((i\partial\!\!\!/ - m)\delta_{ab} - g_{\text{S}} \gamma^{\mu} t^{C}_{ab} A^{C}_{\mu}) \psi_b, \tag{1.1}$$

where repeated indices are summed over. The first part describes the dynamics of the gluon fields A^{C}_{μ} like

$$G^{C}_{\mu\nu} = \partial_{\mu} A^{C}_{\nu} - \partial_{\nu} A^{C}_{\mu} + g_{\text{S}} f^{CDE} A^{D}_{\mu} A^{E}_{\nu}, \tag{1.2}$$

with f^{CDE} the structure constants of SU(3). This decomposition is similar to the Maxwell tensor for the electromagnetic fields within QED except for the last term. As they are colour-charged, gluons can interact with each other. Therefore, the Feynman diagrams within QCD contain three and four-gluon vertices besides the free propagator. The second part of the equation 1.1 corresponds to the Dirac Lagrangian for a quark ψ of colour a. The quark-gluon coupling term reveals the t^{C} generators of SU(3). These matrices can be interpreted as colour rotators in the interaction of a quark with a gluon.

The coupling factor g_{S} is the only free parameter of the QCD theory. One-loop corrections to propagators and vertices induce ultraviolet divergences[‡]. After renormalisation, the strength of the coupling depends of the considered energy scale

$$\alpha_{\text{S}}(Q^2) \equiv \frac{g_{\text{S}}^2}{4\pi} = \frac{12\pi}{(33 - 2N_{\text{f}}) \cdot \ln \frac{Q^2}{\Lambda^2_{\text{QCD}}}}, \tag{1.3}$$

for a number of active flavours N_{f} ranging from 3 to 6. The state-of-the-art determination of this evolution is shown in Figure 1.2 with $\alpha_{\text{S}}(Q^2 = m_{\text{Z}}^2)$ now estimated at the percent level accuracy [8].

The equation 1.3 introduces an energy scale $\Lambda_{\text{QCD}} \sim 200$ MeV separating two regimes of the strong interaction. At high energy / short distance, the coupling between colour charges is weak enough to make perturbative methods (pQCD) applicable. Such feature is called *asymptotic freedom* [9, 10]. Conversely, going towards low momentum transfer, α_{S} increases until it diverges for values below a few GeV. Quarks and gluons are strongly coupled and *confined* in colour-neutral objects generically named hadrons, with a typical size of the order of $\Lambda^{-1}_{\text{QCD}} \sim 1$ fm. Confinement is responsible for the absence of bare colour charges “in daily life”. The origin of this singular property remains to be elucidated from mathematical first principles [11].

Perturbation theory is only valid for typical energy scales beyond 1 GeV, roughly. The non-perturbative regime can be handled with a discretised formulation of QCD known as lattice QCD or lQCD [12]. This method consists of solving the equations on a regular space-time grid where the quarks sit on the nodes linked by the gluon fields. In spite of intensive numerical computations, lattice QCD allows one to calculate the hadron mass spectrum with a good precision as shown in Figure 1.3.

[§] $3 \otimes \overline{3} = 8 \oplus 1$ but the singlet is a colourless linear combination.

[‡] The calculation of Feynman integrals goes to infinity when summing high-energy terms.

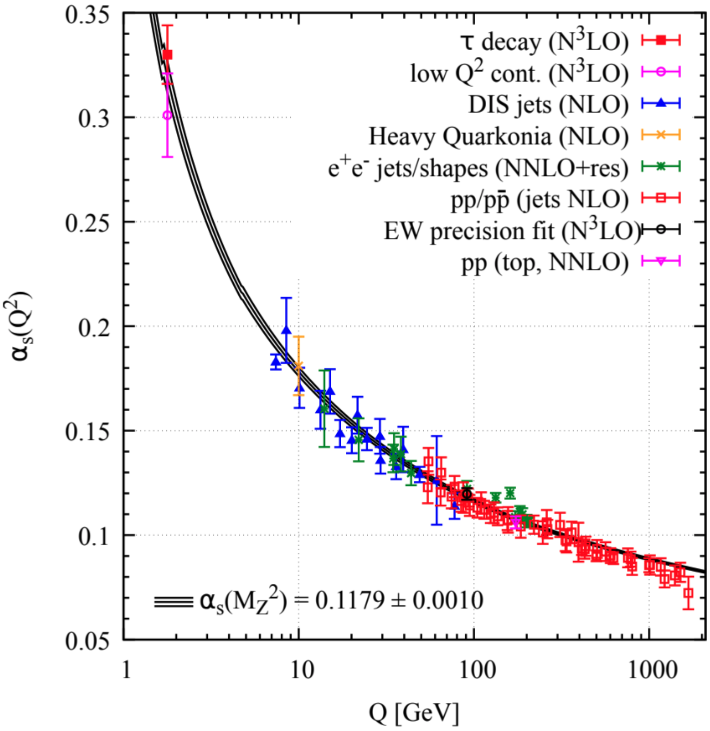

Figure 1.2: *Running* of the strong coupling as a function of the energy scale. The points correspond to perturbative calculations of α_S evaluated at the Z-boson pole mass, using measurements of processes at a typical momentum transfer Q, global fits as well as lattice results. More details are available in the *Quantum Chromodynamics* review [1] from which this figure is taken.

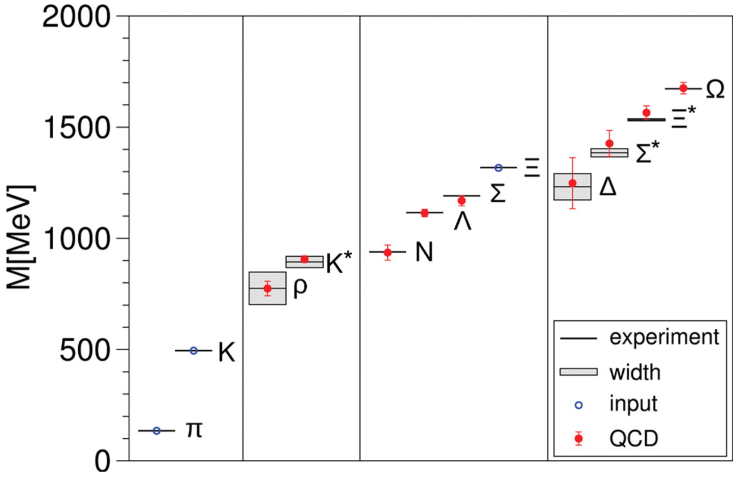

Figure 1.3: Mass spectrum of light hadrons from the review [13]. The points correspond to lattice QCD calculations, compared with experimental measurements. π, K and Ξ are represented with open circles and without any uncertainty because they serve as inputs to set the light-quark masses in the calculations.

1.1.3 Quark-gluon plasma

Deconfinement

Few years after the discovery of the asymptotic freedom, it was realised that, at a sufficiently high temperature $T \gtrsim \Lambda_{\mathrm{QCD}}$, hadronic matter transits to a state where quarks and gluons are no longer confined and can evolve freely [14, 15]. The deconfined phase of hadronic matter is known as the quark-gluon plasma (QGP). Recent lattice QCD calculations shown in Figure 1.4 predict that the phase transition occurs at a critical temperature $T_c = 154 \pm 9$ MeV [16]. The results indicate that none of the thermodynamic variables reaches the non-interacting limit of an ideal gas even for temperatures far above T_c, meaning that quarks and gluons are still strongly coupled inside a QGP medium.

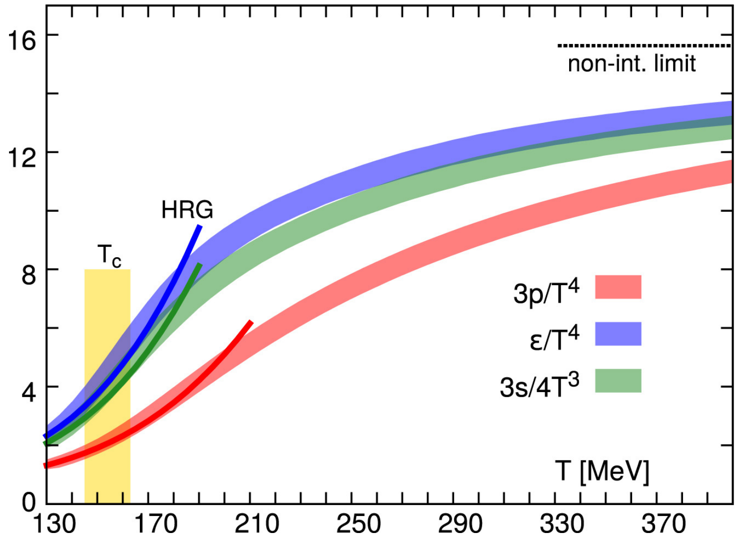

Figure 1.4: Normalised pressure (red), energy density (blue), and entropy density (green) of nuclear matter as a function of the temperature, estimated by lQCD calculations for up, down and strange flavours [16]. The darker lines are predictions from a hadron resonance gas (HRG) model as discussed in the reference. The vertical yellow band delimits the phase transition region. The black dotted line corresponds to the energy density limit for an ideal gas.

Relativistic heavy-ion collisions

The extreme conditions required for the deconfinement can be met in head-on collisions of ultra-relativistic nuclei at the LHC [17]. A phase of quark-gluon plasma is formed during the time evolution of the system as described by the Bjorken scenario [18].

0. In the centre-of-mass frame, the projectiles are contracted along their flying direction by a Lorentz factor of a few thousand. The incoming nuclei can be seen as compact discs of partons.

1. At the very beginning of the collision, the crossing partons interact between each other and produce bunches of colour charges. Some scatterings are characterised by large momentum transfer $Q \gg \Lambda_{\mathrm{QCD}}$. These *hard* processes lead to the production of particles with high transverse momenta, such as jets and heavy-flavour quarks.

2. As the nuclei intersect and move away from each other, the created partons scatter multiple times. The particle density and the temperature of the system diverge rapidly and an out-of-equilibrium phase settles in less than 1 fm/c.

3. Shortly after, if the temperature exceeds the critical one and if the energy density induced by the collision is sufficient, the system reaches a local thermal equilibrium known as the quark-gluon plasma. The hot medium starts to grow in all directions under the effect of the intense pressure gradient. This fireball behaves like a fluid whose evolution is driven by relativistic hydrodynamics [19].

4. As it expands, the plasma cools down and progressively falls apart into hadrons when $T \leq T_c$. Two phases coexist for a short time. After 10 fm/c, all that remains is an expanding gas of hadrons interacting with each other.

5. Inelastic scatterings cease as soon as the gas temperature drops below a *chemical freeze-out* temperature setting the nature of the hadron species. From ~ 20 fm/c, the particle density is too low to maintain elastic interactions. The kinematic distributions cannot change anymore and the particles stream away freely.

Given the short lifetime of the QGP created in such collisions, its characterisation is only possible via the analysis of particles escaping the system [20]. One basic observable is the abundance of light-flavour hadrons in the final state, i.e. produced during chemical freeze-out. By considering the hadron gas as a large system in thermal equilibrium, one can describe and compute the particle densities with a canonical ensemble formalism. Thermodynamic parameters of the fireball at the phase boundary are then extracted from a fit of the calculations to the measured yields, after having accounted for the decay of heavier resonances. Such exercise is illustrated in Figure 1.5 with the comparison of experimental data with predictions from a statistical hadronisation approach [21]. The best agreement gives a chemical freeze-out volume of 5280 ± 410 fm^3 and temperature of 156.5 ± 1.5 MeV, hence consistent with the critical temperature quoted previously.

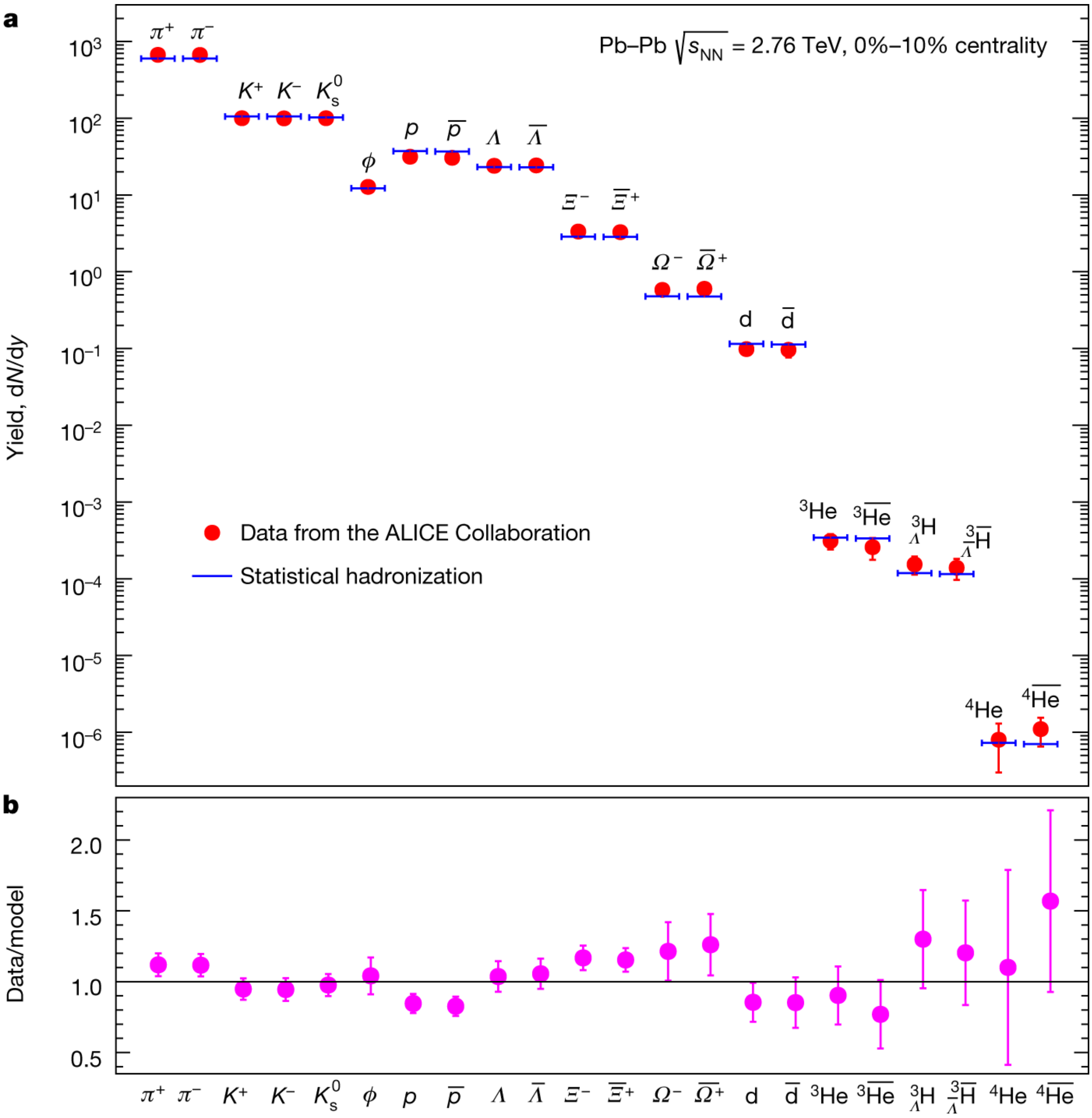

Figure 1.5: Production yield of light hadrons and nuclei in central Pb–Pb collisions at $\sqrt{s_{\rm NN}}$ = 2.76 TeV measured by ALICE and predicted by the statistical hadronisation model [21]. The bottom panel shows the data-to-calculations ratio for each species. The error bars only represent the experimental uncertainties.

Chapter 2

ALICE at the LHC

Before coming to the analysis, we must contextualise the experimental setup. The CERN Large Hadron Collider (LHC) accelerates protons and ions up to ultra-relativistic centre-of-mass energies per nucleon pair. Among the major experiments placed along the LHC ring, the ALICE (A Large Ion Collider Experiment) apparatus has been conceived to exploit the physics potential of nucleus–nucleus collisions at the LHC energies. In particular, its Muon spectrometer instrumented in the forward rapidity region is designed to measure quarkonia in the high-multiplicity environment of the most central collisions.

This chapter provides a description of the ALICE apparatus at the LHC, focusing on the detection systems relevant for the Measurement of Υ production in proton–proton and Pb–Pb collisions.

2.1 The CERN Large Hadron Collider

After the Second World War, physicists imagined an European laboratory for nuclear research in order to promote an international scientific collaboration. Since its foundation, CERN is a leading place for fundamental research and the development of innovative technologies. The greatest accomplishment to date remains the construction of the world's largest and most powerful accelerator, the Large Hadron Collider or LHC [22].

2.1.1 Accelerator complex

The LHC is a 27 kilometre-long circular collider lying in the LEP[†] tunnel beneath the France–Switzerland border. It represents the ultimate piece in a long acceleration chain illustrated in Figure 2.1.

Protons from gaseous dihydrogen are pulsed with a 50 MeV kinetic energy by the LINAC 2 to be distributed into the four rings of the Proton Synchrotron (PS) Booster. The so-formed bunches are accelerated up to 1.4 GeV before transfer to the PS. After evaporation of a pure sample of lead 208, the LINAC 3 provides Pb^{54+} ions of 4.2 MeV per nucleon. The Low Energy Ion Ring (LEIR) accumulates and accelerates them in order to provide bunches with sufficient injection energy for the PS. From this stage on, protons and ions follow the same pattern towards the LHC. The PS defines the final beam structure by splitting and merging bunches with a periodic spacing. Bunch trains are then

---

[†] Large Electron-Positron collider, predecessor of the LHC in operation until 2000

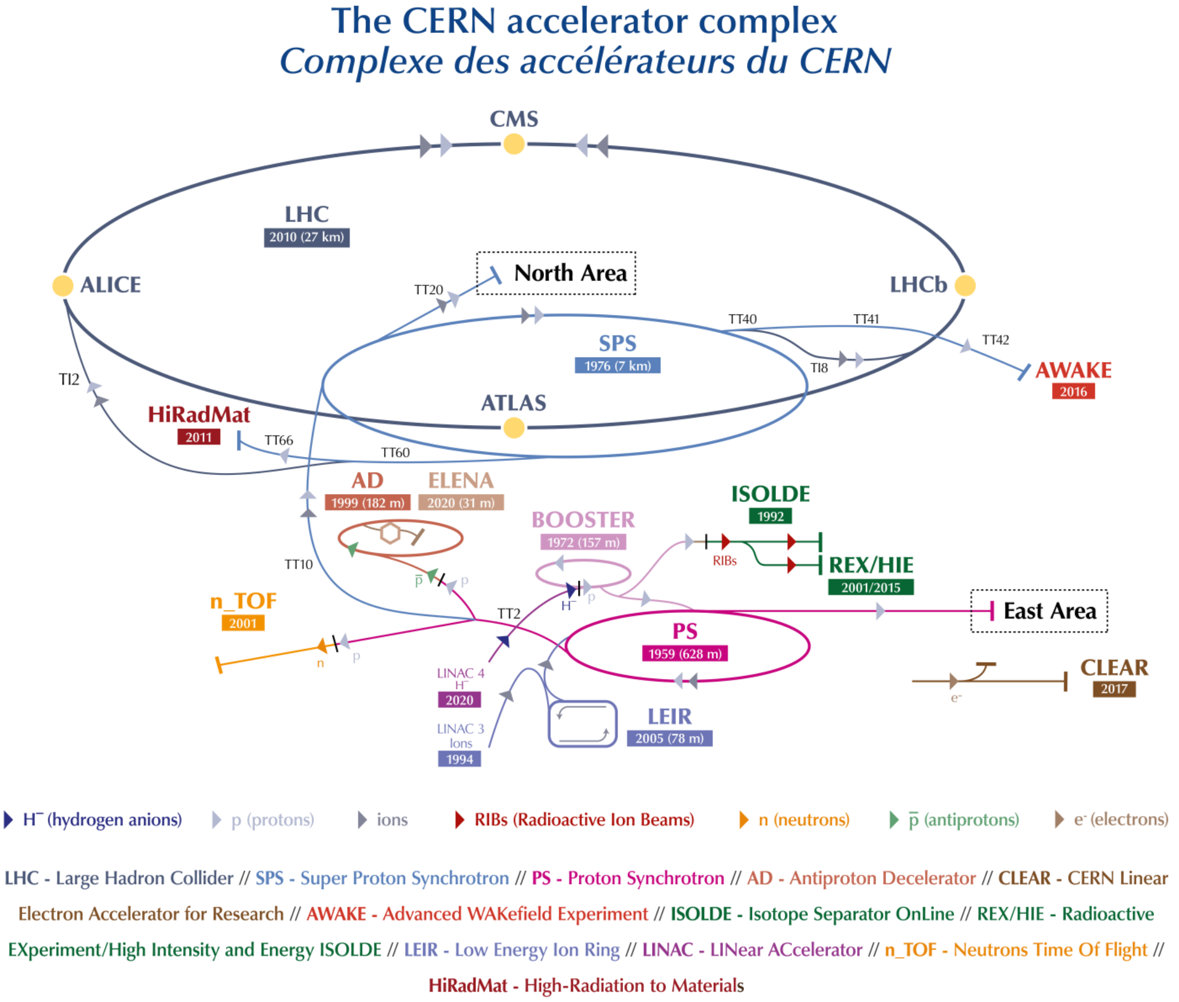

Figure 2.1: Chain of accelerators at CERN. From 2020, the LINAC 4 will replace the old LINAC 2 in preparation for the high-luminosity upgrade phase. The proton synchrotrons serve many other experiments and research facilities. Schema available on this link.

sent to the Super Proton Synchrotron (SPS) for another energy increase. The PS–SPS transfer line takes care of stripping out the last electrons of the lead ions. Finally, two beams feed the LHC ring at two separate injection points so as to circulate in opposite directions. The filling scheme depends on the collaborations' requests and on the machine conditions. For instance, at the end of the 2018 campaign, the heavy-ion physics scheme was consisting of 733 bunches of 2.10^8 Pb nuclei each with a 75 ns spacing [23].

The LHC is composed of various magnets and accelerating cavities. Superconducting dipoles bend the beam trajectory while quadrupoles focus the particles in the transverse plane. Ramping up to a few TeV requires a 8 Tesla magnetic field. Once they have reached the desired energy and quality criteria, the two beams intersect at four of the eight possible interaction points (IP) where detectors are installed.

2.1.2 The LHC experiments

A Large Ion Collider Experiment (ALICE) primarily aims to characterise the QGP properties in laboratory. The apparatus will be described in Section 2.2.

ATLAS [24] and CMS [25] are general-purpose experiments with similar layouts. Both apparatus cover a large phase space in order to discover the Higgs boson and investigate its properties as well as to detect manifestations of new physics at the TeV scale. The two experiments participate to the heavy-ion data takings from the start. Because the detectors are conceived to measure high transverse momenta, their program focuses on hard probes of the QGP, in particular jets, quarkonia and electroweak bosons. Recent results in Pb–Pb collisions can be found in the overviews [26, 27] for ATLAS and CMS respectively.

The LHCb [28] experiment is devoted to the study of rare processes within the heavy-flavour sector. Its single-arm spectrometer is fully instrumented in the forward direction ($2 < \eta < 5$) to reconstruct the hadronic decays of B mesons. The collaboration joined the LHC heavy-ion program at the beginning of Run 2. By injecting noble gases inside the beam pipe, the detector can also operate as a fixed-target experiment. The first results have demonstrated the feasibility of such collisions at the LHC [29].

In addition to the major detectors, the LHC hosts four other experiments:

- The TOTEM detectors [30] extend over 220 metres around both sides of the CMS apparatus in order to measure charged particles emitted with very small angles around the beam pipe. The main purpose of this experiment is to study the proton's structure.
- LHCf measures the production of neutrons and neutral pions in the very forward region with two calorimeters installed at ±140 m from the ATLAS's interaction point [31]. The results serve as inputs for the simulations of cosmic-ray showers in the atmosphere.
- Surrounding the LHCb's interaction region, MoEDAL is designed to search for the hypothetical existence of magnetic monopoles [32] and massive long-lived particles.
- The eighth experiment, FASER [33], will start to collect data during Run 3 with the unique capability to detect light and weakly-interacting particles at the LHC, as well as high-energy neutrinos in a planned upgrade [34].

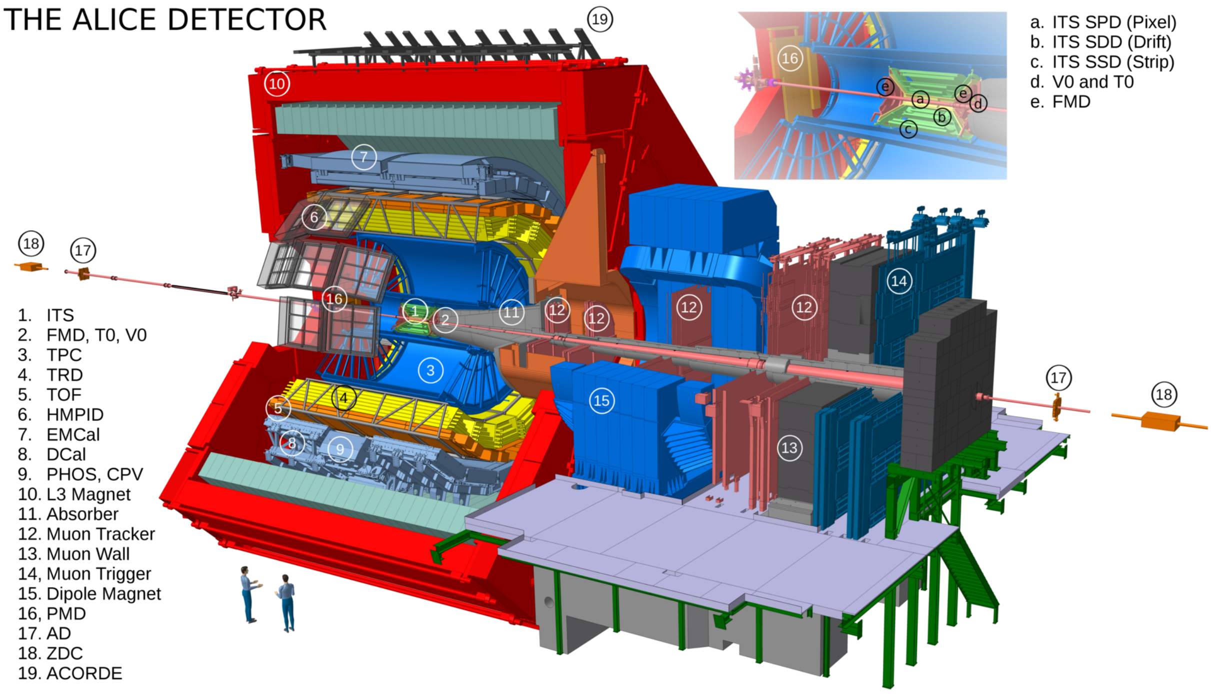

Figure 2.2: Sketch of the ALICE apparatus during the LHC Run 2. A zoom in the area of the interaction point is displayed in the top-right corner. The detectors are numbered on the left-hand side.

2.2 A Large Ion Collider Experiment

The high energy density reached at the LHC offers an unprecedented access to the extreme regime of strongly-interacting matter. However, running an experiment in ultra-relativistic heavy-ion systems is much more challenging than for proton–proton collisions. That is why the ALICE detector has been designed to measure the relevant observables of the QGP properties while handling the anticipated multiplicities [35, 36].

The apparatus, shown in Figure 2.2, can be decomposed into two main ensembles: the central barrel and the muon spectrometer. In addition, smaller detectors placed along the beam pipe provide information on global event characteristics. The nominal interaction point defines the origin of the ALICE coordinate system. The z-axis, parallel to the beam direction, points away from the muon arm. The horizontal x-axis is oriented towards the centre of the LHC and the y-axis is directed upwards so as to get an orthogonal reference frame. The pseudorapidity $\eta = -\ln(\tan(\frac{\theta}{2}))$ is defined according to the polar angle θ of a track with respect to the beam direction.

In the following, we introduce the different detectors used for the measurement of Υ production in proton–proton and Pb–Pb collisions.

2.2.1 Central barrel and forward detectors

Around midrapidity, the ALICE apparatus consists of several systems embedded in the L3 solenoid magnet with a magnetic field $B = 0.5$ T. The setup as well as the detection techniques permit to reconstruct and identify particles down to very low momenta.

Inner Tracking System [37]

Surrounding the interaction region, the inner tracking system (ITS) is an arrangement of silicon-based technologies: two pixel layers closest to the beam pipe (SPD), two cylinders made of drift detectors in the intermediate space (SDD) and two arrays of ladders equipped with strip sensors for the outermost planes (SSD). This configuration enables the separation of the secondary vertex from the collision point in the decay chain of short-lived hadrons.

The first and second SPD layers cover the pseudorapidity ranges $|\eta| < 2$ and $|\eta| < 1.4$ respectively. Their information determine the position of the primary vertex with a longitudinal resolution of the order of 100 µm.

T0 detector [38]

The T0 system is composed of two arrays of photo-multipliers on either sides of the interaction point. It provides fast timing information about the collisions with a resolution better than 50 ps and hence can discriminate beam-beam interactions from background events. The T0 detector is also used to estimate the luminosity in proton–proton collisions as well as the particle multiplicity.

V0 detector [39]

Installed behind the T0 arrays with respect to the nominal IP, the V0 consists of plastic scintillators distributed into two segmented disks, each of them covering a pseudorapidity interval $-3.7 < \eta < -1.7$ and $2.8 < \eta < 5.0$. The coincidence of the signals coming from the sub-detectors generates the main minimum-bias trigger of ALICE. Offline, the main purpose of the V0 is to determine the collision centrality via the measurement of the charged-particle multiplicity, cf. Section 3.1.2. Like the T0, it contributes to the rejection of beam-induced background and to the monitoring of the luminosity.

Zero-degree calorimeters [40]

In order to estimate the geometry of heavy-ion collisions, two sets of compact hadronic calorimeters (ZDC) are positioned at ±116 m along the beam direction. These devices measure the energy deposited in quartz fibres by spectator nucleons. An electromagnetic calorimeter installed at $z = 7$ m puts additional constraints on the centrality evaluation in case of peripheral nucleus–nucleus collisions. The detector is also used offline to remove background events corresponding to electromagnetic interactions of the colliding nuclei.

2.2.2 Muon spectrometer

Measuring the production of quarkonia in the busy environment of heavy-ion collisions is challenging. In particular, the detection of low-p_{T} charmonia decaying into lepton pairs requires excellent particle identification capabilities to separate electrons/muons from a large hadronic background. This is the reason why the ALICE collaboration has built a forward spectrometer specifically designed to reconstruct and identify the muon decay products of quarkonia [41, 42].

The detector performance enables the measurement of all the resonances populating the invariant mass spectrum of opposite-charge muon pairs, from the light vector mesons below 1 GeV/c^2 up to the Υ family around 10 GeV/c^2, as well as the Z-boson. Quarkonium states can be reconstructed down to zero p_T thanks to the Lorentz boost experienced by the muons at large rapidities. Moreover, the analysis of the single-muon continuum allows one to study the production of open heavy-flavour hadrons and $\mathrm{W}^\pm$ bosons via their semi-leptonic decay.

As the measurement of Υ mesons relies on the reconstruction of dimuon candidates, the muon spectrometer deserves a comprehensive description.

General layout

The spectrometer is located in the negative-z region according to the ALICE coordinate system. Its instrumentation covers the pseudorapidity range $-4.0 < \eta < -2.5$ in full azimuth and thus the same rapidity interval[§].

The different elements are represented in Figure 2.3. From the IP downwards, the muon spectrometer is composed of: a passive front absorber to stop the hadron flux, ten planes of detection chambers arranged into five stations, a dipole magnet surrounding the third tracking station, an iron wall to filter muons, and two trigger stations followed by a rear absorber.

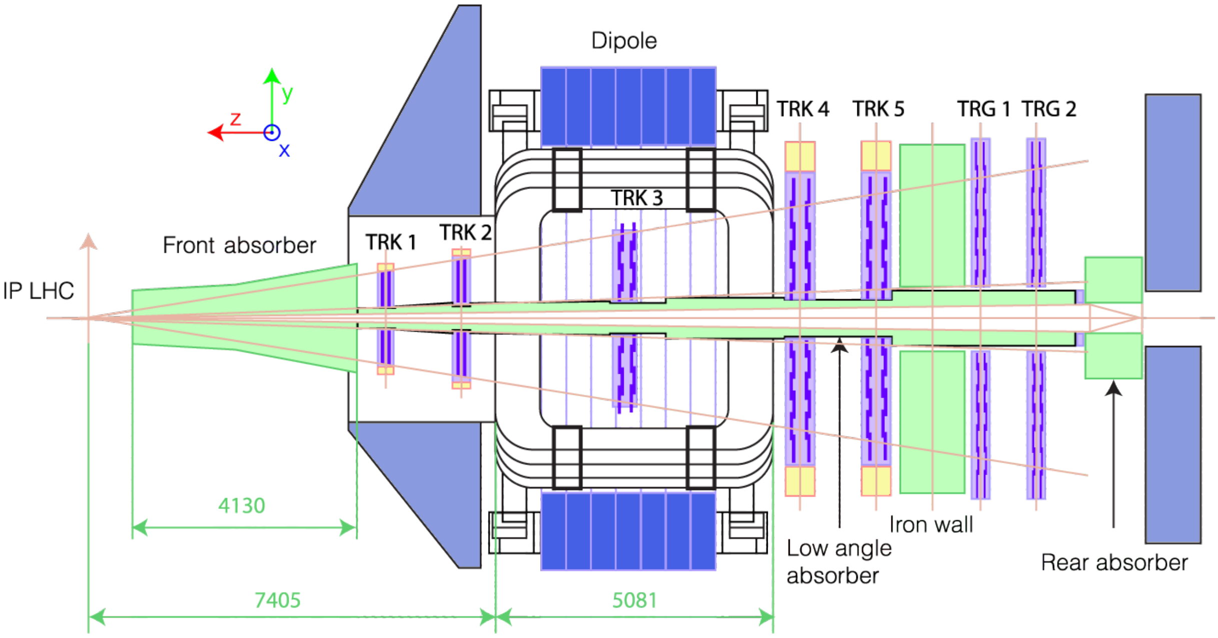

Figure 2.3: Cross-section view of the ALICE muon spectrometer in the (z, y) plane. The light green parts represent the different absorption elements. The tracking and trigger stations are drawn in purple. The dimensions given are in millimetres. Schema adapted from the original figure in the reference [35].

[§] In this thesis, we choose to adopt a positive notation justified by the symmetry of the collisions under consideration.

Absorption elements

To reduce the particle flux, the muon detection system is equipped with a set of passive materials. The structure of the absorbers is optimised to suppress the background level while limiting the drawbacks on the track reconstruction.

Recessed into the central barrel, the front absorber is a 4.13 metre long half-cone whose nose is 90 cm away from the nominal IP. The closest part of the IP region stops the flux of hadrons coming from the interaction vertex. The rear end consists of lead and polyethylene layers absorbing the low-energy particles produced inside the whole volume. The front absorber is mostly composed of carbon and concrete in order to minimise the multiple scattering of the muons of interest. An external lead layer protects the central barrel detectors from back-scatterings. The total thickness of the front absorber represents ten nuclear interaction lengths, λ_{int}.

All along the spectrometer, the LHC beam pipe is enveloped by a dense shielding made of lead, tungsten and stainless steel. This element intercepts the particles emitted at very small angles or originating from beam-gas interactions[‡].

Between the last tracking station and the first plane of trigger chambers, a 1.2 m thick iron wall ($\sim 7.2\ \lambda_{\text{int}}$) filters muons from particles traversing the front absorber. Only muons with a total momentum larger than 4 GeV/c can pass through the iron wall.

Finally, a second iron wall, placed behind the trigger system, protects the detection chambers from background events occurring downstream.

Tracking system

The specifications of the muon spectrometer are driven by the physics motivation to identify the three Υ resonances [41]. In addition, the detection elements must be able to cope with the particle multiplicity expected in the most central Pb–Pb events. These requirements constrain the technologies, the design as well as the layout of the muon detectors.

Particle trajectories are reconstructed from the information of their passage through cathode-pad chambers (CPC). The latter consist of a plane of anode wires parallel to the y-axis, sandwiched by cathodes segmented into readout pads. The wires, subjected to a high voltage of about 1600 V, are immersed in a gaseous volume. The working principle of a CPC is illustrated in Figure 2.4. An incident electrically-charged particle ionises the medium. Under the effect of the electric field induced by the wires, the free electrons are accelerated towards the anode plane and can ionise the gas again near the wires. The resulting ion cloud drifts towards the readout pads. The distribution of the collected charges gives a (x, y) hit position.

The CPC performance fulfils the operating data-taking conditions. The particle multiplicity imposes a high granularity for the cathode planes. The chambers are made of thin composite materials in order to minimise the deflection of muon tracks. A complete ionisation efficiency can be reached thanks to the gas mixture of 80%Ar–20%CO_2.

To achieve the 100 MeV/c^2 mass resolution needed to disentangle the Υ states, the muon tracks must be reconstructed with a 100 µm accuracy. The tracking system is formed by five stations installed over ten metres along the beam pipe. Each station

---

[‡] Collisions with the molecules of the residual vacuum inside the LHC beam pipe. In the IP region, the gas density is within the range 10^{-10}–10^{-11} mbar.

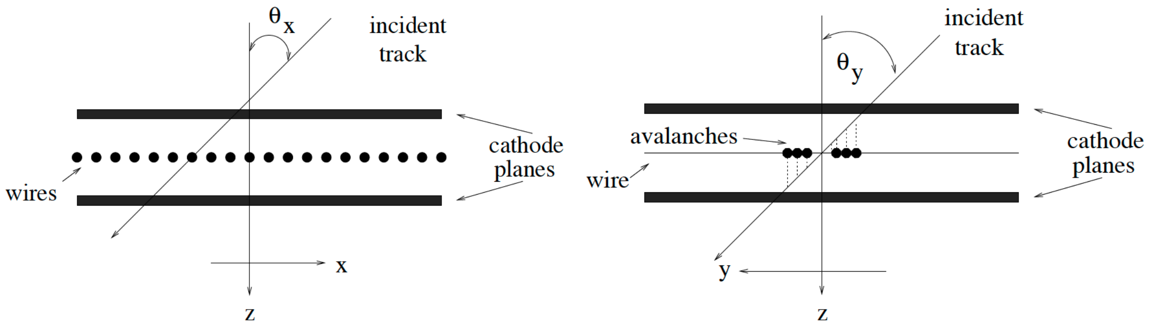

Figure 2.4: Working principle of a cathode-pad chamber. Schema taken from the technical design report of the muon spectrometer [41].

consists of two identical CPC planes. Their radius grows with the longitudinal position so as to define a cone whose origin is the nominal IP. This geometry ensures that muons within a 2°–9° angular acceptance are detected. The chambers cover a total active surface of about 100 m^2. As the hit density increases towards the beam pipe, the readout pads are segmented such that the chamber occupancy is uniform.

The first station is intended to measure as precisely as possible the transverse position of the muons at the exit of the front absorber. The four planes composing the first two stations have a quadrant configuration with the readout electronics distributed on their surface. For the other stations, a slat architecture was chosen in order to reduce the mechanical stress due to the large dimensions. The slat electronics are installed out of the active region. The chambers overlap to avoid dead zones inside the detection acceptance. The displacement of the station planes relative to a reference geometry is monitored with a ~ 40 µm precision [36].

To measure the momentum of the particles traversing the spectrometer, a large dipole magnet surrounds the third tracking station. Its dimensions fit within the geometric acceptance for muon detection. The dipole generates a horizontal magnetic field of 0.67 T at its centre, bending the charged-particle trajectories along the y-axis. The resulting field integral of 3 T·m between the IP and the iron wall is determined according to the requirement for the Υ mass separation.

In summary, the configuration of the tracking system provides 10×2 independent measurements of impact points for the track-finding algorithm [43]. This procedure builds track candidates, starting from stations 4 and 5 to the first ones. The reconstructed tracks are then extrapolated to the interaction region for association with a primary vertex determined by the SPD, and corrected for multiple scatterings inside the front absorber. The overall spatial resolution of the muon tracking system is a few hundred microns in the bending direction and about one millimetre in the non-bending plane.

Trigger system

After passing through the iron wall, the particle flux is still composed of muons from pion and kaon decays. To select events of interest such as the ones containing dimuons, the forward muon spectrometer is equipped with a dedicated system delivering fast trigger information to the central processor of ALICE.

The muon trigger decisions are based on the determination of the transverse momen-

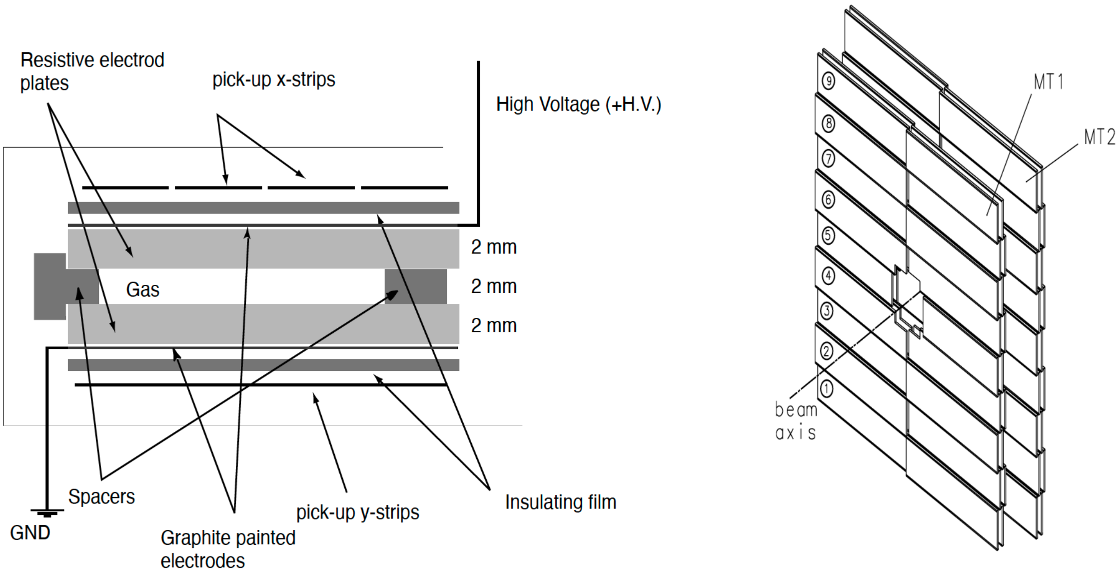

Figure 2.5: (left) Schematic cross-section view of a resistive-plate chamber. (right) Layout of the two trigger stations. Figures extracted from the technical design report [41].

tum via resistive-plate chambers (RPC). Similar to a CPC, these detectors measure a (x, y) position from the collection of free charges induced by the passage of a particle. A cross-section view of a RPC can be observed in the left panel of Figure 2.5. A 2 mm wide gas gap is enclosed by resistive plates made of bakelite. The two plates are connected to graphite electrodes maintaining a uniform electric field inside the gaseous volume. The hit coordinates are read out on both sides of the chamber by orthogonal strips: one face reads the position in the bending plane with horizontal strips and vice versa.

The trigger system consists of four planes with 18 RPCs each, for a total active area of about 140 m^2. The detection planes are arranged in two stations located at 16 and 17 metres from the IP. The layout of the trigger stations is shown in the right panel of Figure 2.5. As for the CPCs, the segmentation of the cathodes is finer for the chambers close to the beam pipe. The selection on muon p_{T} requires a space resolution better than one centimetre, achieved thanks to the granularity of the strips. The composition of the electrodes as well as of the gas mixture have been studied such that the RPC read-out capabilities match the interaction rate.

Figure 2.6 illustrates the working principle of the muon trigger system. A particle with an electric charge q originating from the IP is deflected from its trajectory by an angle θ_d by a magnetic field B at the coordinates $(X_F; Y_F; Z_F)$. Based on the measurement of the hit positions in the two stations, a local algorithm computes the deviation angle as

$$\theta_d = \frac{1}{Z_F}\left(\frac{Y_1 Z_2 - Y_2 Z_1}{Z_2 - Z_1}\right). \tag{2.1}$$

Under the small-angle approximation, the transverse momentum reads

$$p_{\mathrm{T}} \approx \left|\frac{qBL}{\theta_d}\right| \times \frac{\sqrt{X_F^2 + Y_F^2}}{Z_F}, \tag{2.2}$$

where L is the length of the dipole magnet, i.e. five metres. The local boards generate

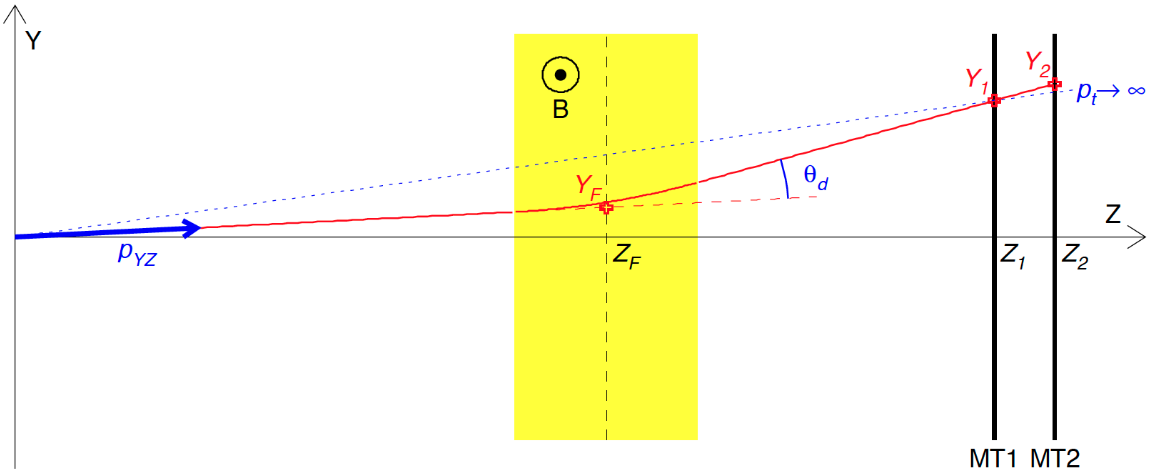

Figure 2.6: Working principle of the trigger system of the muon spectrometer.

a low- or a high-p_{T} trigger signal according to pre-defined thresholds whose values are a compromise between background rejection and detection efficiency for quarkonia. The single-muon information is gathered at a global level to deliver the six possible outputs to the central trigger processor of ALICE: at least one muon above the low(high)-p_{T} threshold, two low(high)-p_{T} muons with opposite charges and two low(high)-p_{T} with the same charge.

Chapter 3

Measurement of Υ production

This chapter details all the analysis steps towards the determination of the production yields. The Υ mesons are reconstructed via their decay into muon pairs detected with the ALICE muon spectrometer. After selection of events and tracks, the raw number of candidates can be extracted and then corrected for efficiencies. The results are finally normalised to the number of minimum bias events. We discuss the systematic uncertainties at each stage of the procedure.

As the analyses are similar for the two collision systems, we focus on the measurement in Pb–Pb collisions. More information about the proton–proton analysis is provided if relevant.

3.1 Data processing

3.1.1 Data samples

This thesis is based on data recorded at the end of 2015 and 2018 in Pb–Pb collisions at a centre-of-mass energy per nucleon pair $\sqrt{s_{\rm NN}} = 5.02$ TeV. Proton–proton data were collected at the same centre-of-mass energy in 2017.

The campaigns of data taking are separated into periods differing by at least one major change in the global configuration: collision system and/or energy, modification in the experimental setup, etc. According to the ALICE notation, the name of a period is written “LHCYYx” where “YY” corresponds to the operating year and “x” is an identifier letter. The analysed periods of Pb–Pb collisions are named LHC15o for 2015, LHC18q and LHC18r for 2018. The latter two differ by the dipole polarity. The same explanation applies to the LHC17p and LHC17q periods of proton–proton data.

Within a period, data taking is split into *runs* numbered in chronological order. A run is defined by stable recording conditions over a relatively long period of time, of the order of a few hours. The end of a run is triggered automatically when a system behaves abnormally or can be deliberately actuated by an operator. It is therefore important to ensure that possible malfunctions do not impact the quality of the data. A first selection consists in establishing a list of *good* runs from general information on the beam conditions and the apparatus configuration during the data taking. In the context of this work, the SPD, the V0 as well as the muon tracker and trigger systems must have participated as readout detectors. Once the data have been reconstructed, the quality assurance (QA) verifies its reliability for each sub-detector. The procedure for the muon spectrometer is explained in the thesis [44]. Problems not spotted during the data taking or reconstruction are identified by monitoring the performance (time evolution of the efficiencies, number of tracks per event, etc). Depending on the severity of the issues, complete runs can be discarded.

3.1.2 Centrality determination

In the first chapter, we have seen that the global QGP properties strongly depend on the initial conditions of the system. The modification of the Υ production should be studied as a function of a physical quantity linked to the geometry of the nucleus–nucleus collision. Generally, we refer to the *centrality*, defined as a fraction of the total inelastic cross section. The smaller the impact parameter, the larger the overlap area and therefore the more nucleons scatter to each other. Since no experiment is able to directly access the impact parameter, one must rely on an observable scaling with it. In the following, we introduce shortly the ALICE procedure for the centrality determination of Pb–Pb collisions. The complete description is provided in the public note [45].

The definition of the centrality is based on the multiplicity of charged particles measured by the V0 arrays. The multiplicity distribution is sliced into centrality classes according to the total integral. In parallel, Monte Carlo simulations of independent nucleon–nucleon collisions reproduce the measured distributions via calculations within a Glauber approach [46]. The number of particles generated per scattering follows a negative binomial distribution (NBD), assuming that the average multiplicity in soft and hard interactions is proportional to N_{part} and N_{coll}, respectively. The Glauber calculations are then fitted to the data as shown in Figure 3.1. Mapping the measured and simulated multiplicity distributions allows one to attribute geometrical quantities to each centrality class.

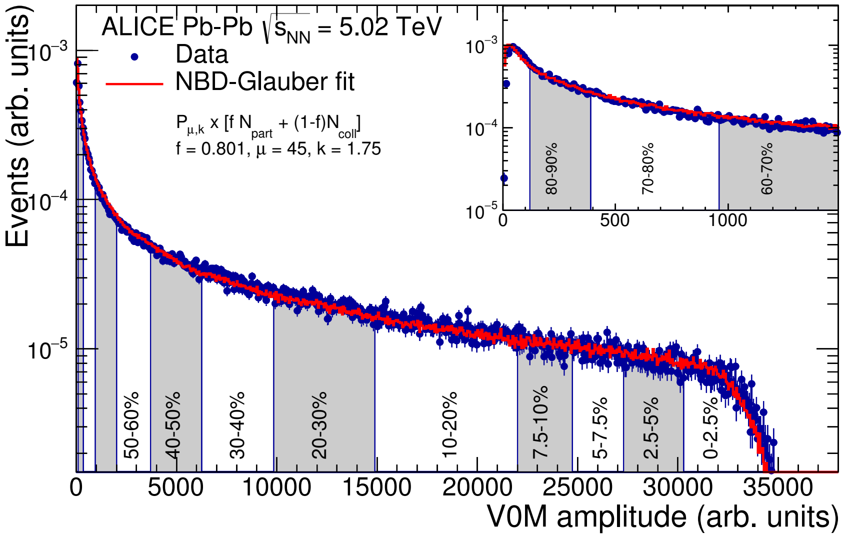

Figure 3.1: Distribution of the sum of amplitudes in the V0 detectors. The red line represents the result of the Glauber fit over the measured multiplicity. The legend formula corresponds to the NBD and the fit parameters. The top-right corner shows a zoom for the most peripheral collisions. Additional figure of the article [47], available at this link.

The average number of participants $\langle N_{\text{part}} \rangle$, of binary nucleon–nucleon collisions $\langle N_{\text{coll}} \rangle$ as well as the average nuclear overlap function $\langle T_{\text{AA}} \rangle$ used in the present analysis are reported in Table 3.1. The values are taken from the public note [45]. For the centrality classes not available in the note, the values and the corresponding uncertainties are taken as the average over narrower ranges. For example, the geometric quantities of the 70–90% centrality interval are evaluated from the 70–80% and 80–90% classes.

Centrality class	$\langle N_{\text{part}} \rangle \pm$ syst	$\langle N_{\text{coll}} \rangle \pm$ syst	$\langle T_{\text{AA}} \rangle \pm$ syst [mb^{-1}]
0–5%	383.4 ± 0.6	1763 ± 19.4	26.08 ± 0.18
5–10%	331.2 ± 1.0	1382 ± 15.2	20.44 ± 0.17
10–15%	283.0 ± 1.1	1090 ± 12.3	16.12 ± 0.14
15–20%	241.0 ± 1.2	857.3 ± 10.5	12.68 ± 0.12
20–30%	187.9 ± 1.3	592.7 ± 8.2	8.77 ± 0.10
30–40%	130.8 ± 1.3	343.8 ± 5.8	5.09 ± 0.08
40–50%	87.14 ± 0.93	185.7 ± 3.3	2.75 ± 0.05
50–70%	42.66 ± 0.69	65.96 ± 1.57	0.976 ± 0.023
70–90%	11.35 ± 0.16	10.89 ± 0.22	0.161 ± 0.004
0–30%	269.1 ± 1.0	1046 ± 11.7	15.48 ± 0.12
30–90%	54.32 ± 0.66	170.8 ± 2.1	1.68 ± 0.04
0–90%	125.9 ± 0.8	424.6 ± 5.5	6.28 ± 0.06

Table 3.1: Glauber fit quantities for the Pb–Pb analysis as a function of centrality. The uncertainties originate from the propagation of the uncertainties of MC input parameters. The numerical values are extracted from the note [45].

3.1.3 Event and track selections

From the list of exploitable runs for physics analyses, we select the events likely to contain the decay products of Υ mesons. Other kinds of events are considered for different purposes outlined throughout this chapter. The muon tracks must fulfil quality criteria prior to the formation of dimuon candidates.

Types of events

Recorded events of interest are sampled into trigger classes which are combinations of output signals from one or more detector. The coincidence of the minimum bias trigger, introduced in the V0 description 2.2.1, with muon trigger signals listed in Section 2.2.2, defines the classes

- ▷ *CMSL*: detection of a muon candidate hitting the trigger chambers with a transverse momentum above an online threshold set to 0.5 and 1 GeV/c for the proton–proton and Pb–Pb data takings, respectively. These values correspond to the p_{T} thresholds for which the muon trigger efficiency reaches 50%. The CMSL trigger class is essential for the Event-mixing technique.

- ▷ *CMUL*: a positive and a negative charge track candidate, each satisfying the CMSL condition. It is also referred to as the unlike-sign dimuon trigger later on.
- ▷ *CMLL*: two muons of same electrical charge satisfying the CMSL condition or like-sign dimuons. This class is used for a normalisation step in Section 3.2.1.

A so-called *physics selection* (PS) applied to each trigger class reduces the number of background events present in the data. The bunch crossings are isolated from beam–gas collisions thanks to the delayed signals of the V0 timing information [39]. In the case of Pb–Pb collisions, the ZDCs allow one to discard electromagnetic interactions between the colliding nuclei. Therefore, these two detectors must also have participated to the data takings and be examined by the QA.

The Pb–Pb analysis is restricted to the 0–90% most central collisions for which the minimum bias trigger is fully efficient. The number of runs and events after applying these selections are reported in Table 3.2. Less CMUL events are rejected for Pb–Pb collisions because events are triggered according to the multiplicity. Beam–gas interactions are therefore underrepresented within the data samples. During the LHC17q period, data were collected at a higher interaction rate, degrading the efficiency of the trigger chambers.

Collision system	Year	Period	Number of selected QA runs	$N_{\mathrm{events}}^{\mathrm{CMUL\&PS}}$	Event rejection by the PS
Pb–Pb	2015	LHC15o	137	126.5 M	0.2%
	2018	LHC18q	130	110.7 M	0.4%
		LHC18r	98	162.8 M	0.2%
pp	2017	LHC17p	38	6.7 M	1.0%
		LHC17q	13	11.7 M	3.4%

Table 3.2: Number of runs validated by the muon quality assurance as well as the number of CMUL triggered events after physics selection, per period for each collision system. The values for Pb–Pb data are quoted for the 0–90% centrality interval.

Selection criteria for muon tracks

Although the front absorber stops most of the hadrons flying towards the forward region, its composition also has drawbacks on the track reconstruction. Offline selections improve the quality of the muon samples and filter the dimuon candidates for the signal extraction. These additional selections are applied regardless of the trigger class considered and are common to both analyses.

- The pseudorapidity of each reconstructed track is within the $-4.0 < \eta < -2.5$ range, i.e. the geometrical acceptance of the spectrometer.
- A track reconstructed by the muon tracking system must match a track segment measured in the trigger stations above the low-p_{T} threshold. This requirement removes low-momentum muons, mainly coming from pion and kaon decays, as they are intercepted by the iron wall.
- When crossing the front absorber, the particles may undergo multiple scatterings, especially in the densest parts. A condition on the radial position at the end of the absorber, R_{abs}, such that $17.6 < R_{\mathrm{abs}} < 89.5$ cm rejects the tracks with a poor pointing resolution towards the interaction vertex.
- Finally, the muon tracks must originate from the collision point. This condition can be constrained by studying the $p \times$ DCA distribution, product of the track momentum and the extrapolated position in the transverse plane of the vertex. Beyond 6σ, the distribution consists of *fake tracks* generated by the reconstruction algorithm, as well as particles produced outside the interaction region.

Muons pairs are formed from tracks satisfying all these criteria. Only pairs within the $2.5 < y < 4.0$ rapidity interval are then considered. In the two analyses, the measurement is statistically limited to the dimuon p_{T} below 15 GeV/c since no Υ signal is found beyond this value as we can observe in Figure 3.2.

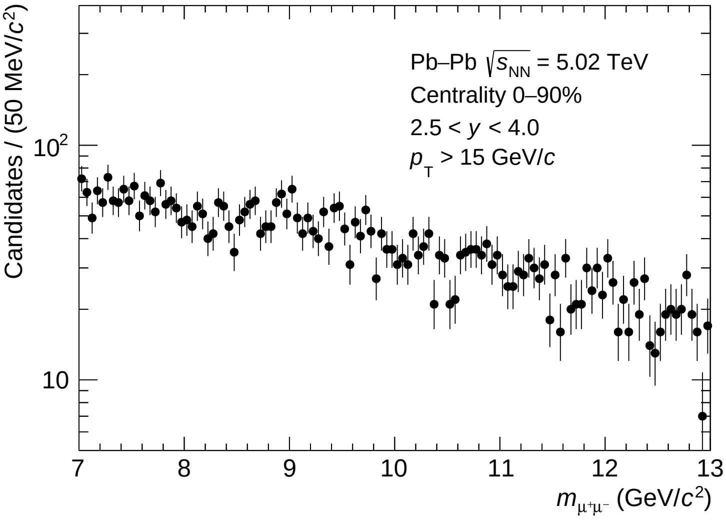

Figure 3.2: Invariant mass distribution of opposite-sign muon pairs in Pb–Pb collisions for dimuon $p_{\mathrm{T}} > 15$ GeV/c.

3.2 Signal extraction

The estimate of the number of Υ mesons decaying into opposite-sign muon pairs is based on the CMUL triggered events. Figure 3.3 shows the invariant mass distributions of the dimuon candidates in the 5–15 GeV/c^2 invariant mass interval. The data samples of each period are merged into a single one after evaluating the consistency between the signal parameters reported in Table 3.3. These parameters agree within less than two standard deviations. Henceforth, the combined Pb–Pb periods are labelled “Run 2”, but will also be analysed separately in order to cross check the results[†].

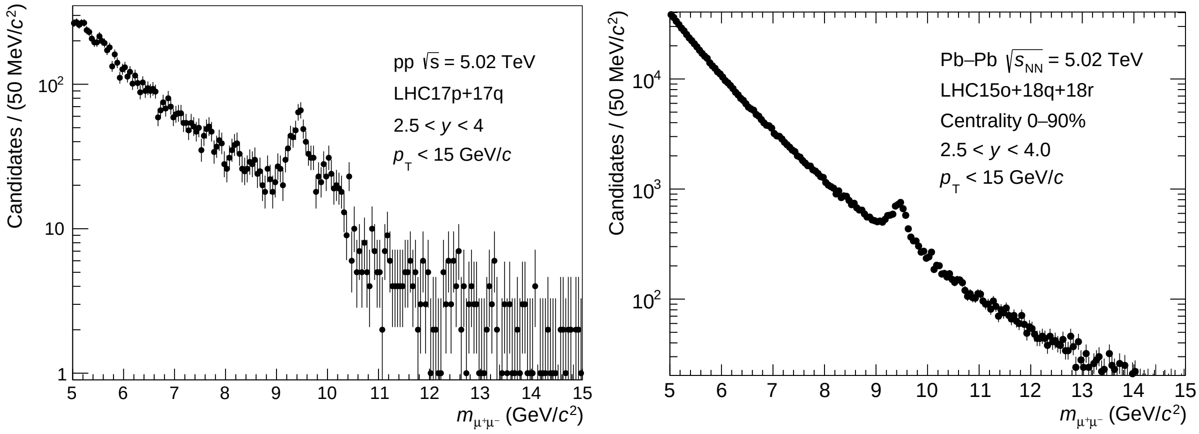

Figure 3.3: Unlike-sign dimuon invariant mass spectrum for (left) proton–proton and (right) Pb–Pb collisions after merging all the data-taking periods. The peak structure around 9.5 GeV/c^2 reveals the presence of Υ resonances.

Period	$m_{\Upsilon(1S)} \pm$ stat [GeV/c^2]	$\sigma_{\Upsilon(1S)} \pm$ stat [MeV/c^2]
pp 2017	9.446 ± 0.015	144 ± 13
LHC15o	9.463 ± 0.009	146 ± 11
LHC18q	9.452 ± 0.010	132 ± 11
LHC18r	9.449 ± 0.008	122 ± 8
Run 2	9.453 ± 0.005	130 ± 6

Table 3.3: Pole mass and width of the Υ(1S) signal shape per period of data taking. The results are obtained from the Fitting procedure for $2.5 < y < 4.0$ and $p_{\mathrm{T}} < 15$ GeV/c, within the 0–90% centrality class for the Pb–Pb case. The quoted uncertainties correspond to the average of the statistical uncertainties returned by the fits.

In Figure 3.3, the contribution from the Υ resonances can be seen as an excess above a background continuum decreasing towards higher invariant mass. The Υ(1S) signal shape is clearly visible whereas the two excited states are not separated due to the mass resolution. The signal-to-background ratio is smaller in Pb–Pb with respect to pp collisions. This observation may result from a larger contribution of dimuon sources and/or the expected suppression of the bottomonium production.

The evaluation of the raw yields is a key step of this thesis. The Υ signal is extracted from the modelling of the invariant mass distribution. In the following, we will see how to exploit the background composition in Pb–Pb collisions in order to describe it.

[†] The size of the pp data sets does not allow us to study the LHC17p and LHC17q periods individually.

3.2.1 Event-mixing technique

In the invariant mass region of the Υ resonances, the unlike-sign dimuon continuum is made of:

- Opposite-charge muon pairs produced by the Drell-Yan process, dominant above 10 GeV/c^2 at forward rapidity [48].
- Pairing of muons from the semi-leptonic decay of *correlated* heavy-flavour hadrons, i.e. produced by the same hard scattering.
- Random combination of muons originating from different processes, e.g. a pion decay product with the one of a beauty hadron.

For the latter source, the probabilities to associate two muons with opposite or identical charges are equal. Hence the uncorrelated background could be subtracted from the data by estimating the amount of like-sign dimuons per event. The event-mixing technique allows one to mimic the combinatorial background with, in principle, unlimited data.

Pooling and mixing

The first step consists of forming pools of events characterised by a similar collision centrality, on a run-by-run basis. The intervals are chosen to match the centrality classes wherein a significant Υ signal can be found. Previous studies showed that defining pools of events with a close z-position of the primary vertex does not improve the quality of the mixing [44]. We have checked that it was also the case in the present analysis. As a result, more muons per event pool are available.

Next, each muon track of a given event is paired with all the tracks from other events belonging to the same centrality pool. This *mixing* operation can be repeated with as many events as available. The mixing is based on CMSL triggered events in order to have an unbiased track selection. The pairing is performed with tracks meeting the selection criteria listed in Section 3.1.3. At the end of this step, the dimuon samples per run are merged while conserving the centrality pools.

Normalisation

The mixed-event distributions are then normalised thanks to like-sign muon pairs. This procedure relies on the assumption that the negative and positive dimuon spectra do not contain any source of correlated background.

Let N_{raw} be the number of dimuon firing the CMUL or CMLL trigger conditions for an interval of invariant mass $\mathrm{d}m$. The distribution integrals over the 5–15 GeV/c^2 mass window are related by the equation

$$\int_5^{15} N_{\text{mixed}}^{+-}\,\mathrm{d}m = \int_5^{15} 2R\sqrt{N_{\text{raw}}^{++}N_{\text{raw}}^{--}}\,\mathrm{d}m \text{ with } R = \frac{N_{\text{mixed}}^{+-}}{2\sqrt{N_{\text{mixed}}^{++}N_{\text{mixed}}^{--}}}. \tag{3.1}$$

The R factor accounts for the possible asymmetry in the acceptance and detection of muon charges. As indicated by Figure 3.4, the R factor is compatible with unity as this mass region is essentially composed of high-momentum tracks, well reconstructed by the

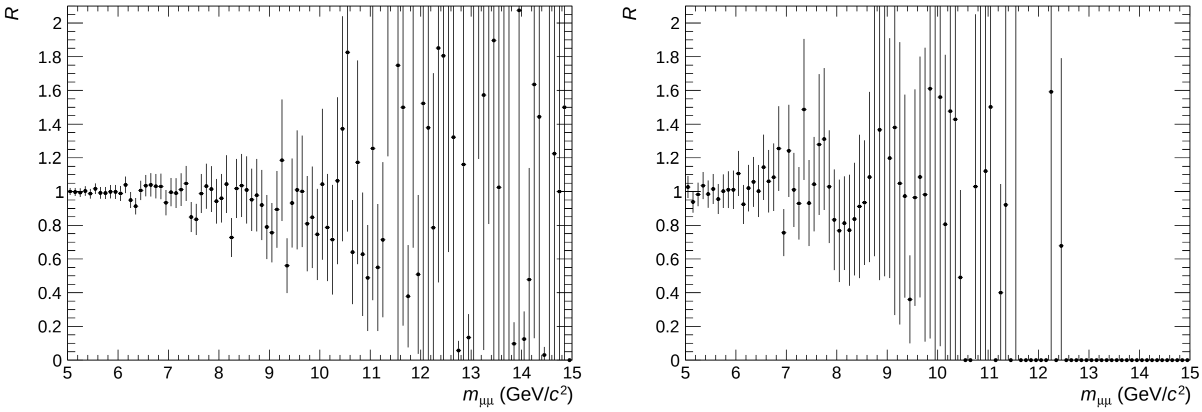

(a) 0–5% centrality

(b) 70–90% centrality

Figure 3.4: Distribution of the acceptance factor R as a function of the dimuon invariant mass for the LHC18q period.

spectrometer. The sizeable error bars depict the limited number of muon pairs with a large invariant mass. Few, if any, mixed-event dimuons enter the high-mass region for the most peripheral collisions.

Once normalised, the mixed-event distributions per centrality interval and period are added together if necessary. We control the quality of the normalisation procedure by comparing visually the p_{T}, rapidity and invariant mass distributions shown in Figure 3.5. It confirms that the like-sign dimuon continuum of the data can be totally reproduced with the event-mixing technique and thus be used to normalise the unlike-sign distribution.

Background subtraction

Finally, the mixed-event distribution is subtracted from the raw invariant mass spectrum. The result is displayed in Figure 3.6 for the complete Run 2 data set. The visible remaining background is composed of pairs of correlated muons. The large error bars in the low-mass region reflect the statistical uncertainties of the data. Due to the residual background, this spectrum is used as an alternative invariant mass distribution for the signal extraction of the Pb–Pb data analysis.

3.2.2 Fitting procedure

The number of reconstructed Υ states is extracted from the invariant mass spectrum of unlike-sign dimuon candidates. We perform an unbinned maximum log-likelihood fit with the RooFit package [49]. As noticed from Figure 3.3, the signal-to-background ratio is relatively low near the Υ mass region and the excited states are barely discernible. The precise evaluation of the number of signal events requires a comprehensive study of the invariant mass distribution.

The modelling of the signal shape must take into account the detector effects on the reconstruction of dimuon candidates. Muons are expected to lose energy when crossing the front absorber. As a result, the invariant mass distribution is shifted towards lower mass and the signal shape is asymmetric. The extended Crystal Ball distribution (CB2) consists of a Gaussian function for the detector resolution, modified by a power-law *tail*

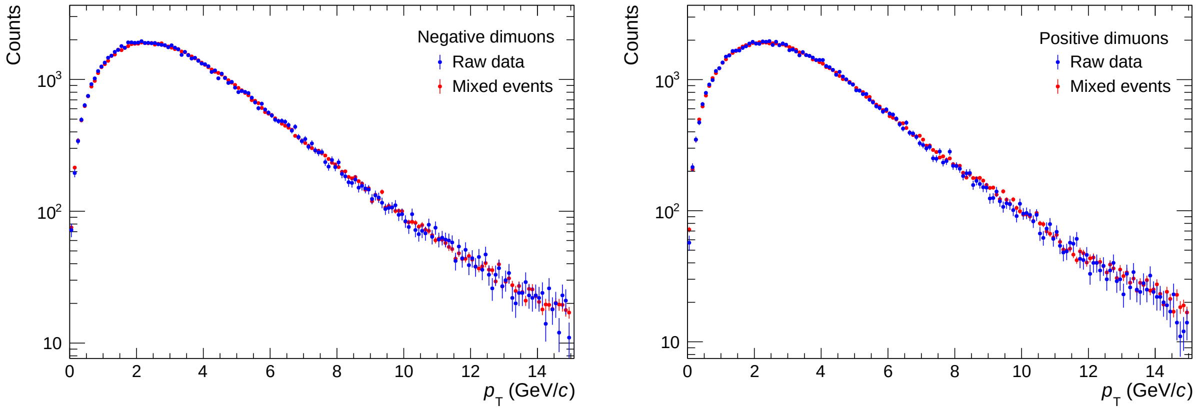

(a) Negative dimuon p_{T} spectrum

(b) Positive dimuon p_{T} spectrum

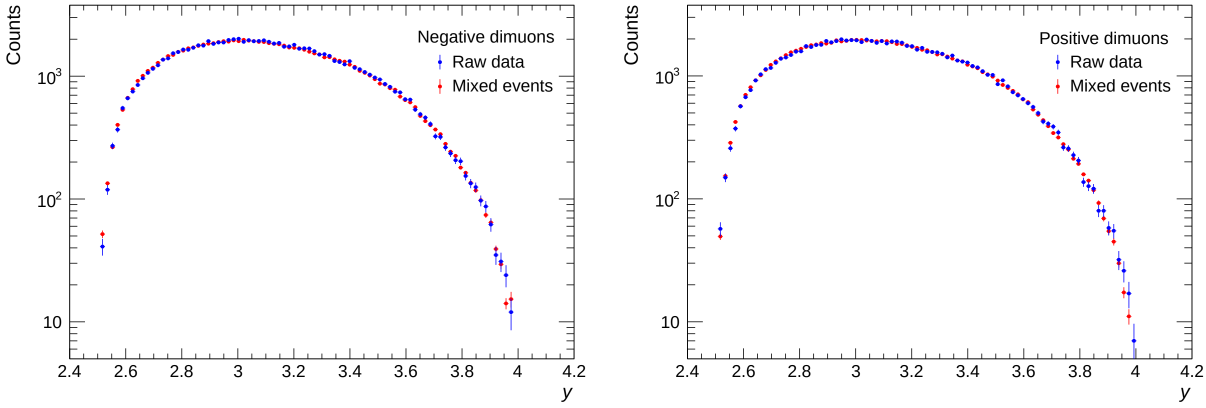

(c) Rapidity distribution of negative-sign dimuons

(d) Rapidity distribution of positive-sign dimuons

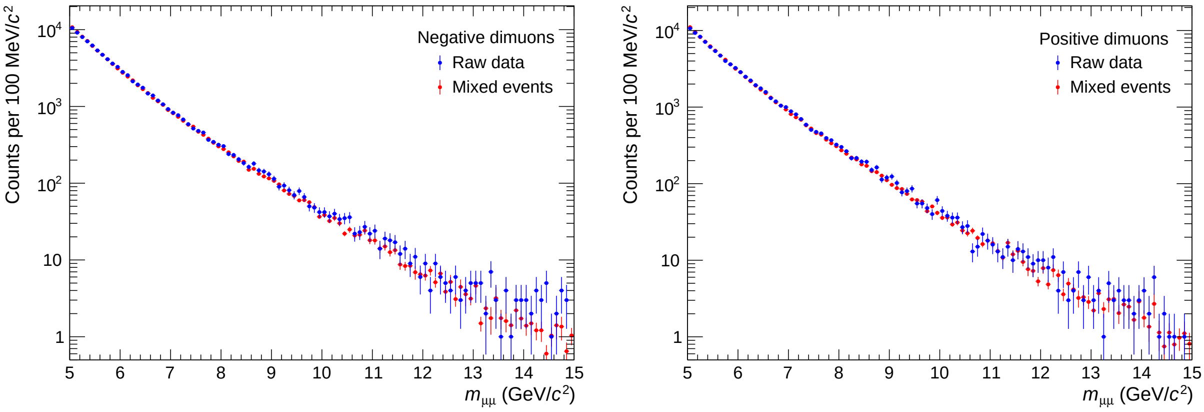

(e) Invariant mass distribution of negative-sign muon pairs

(f) Invariant mass distribution of positive-sign muon pairs

Figure 3.5: (top) Transverse momentum, (middle) rapidity and (bottom) invariant mass distributions of like-sign dimuons in the 0–90% centrality interval for the LHC15o period.

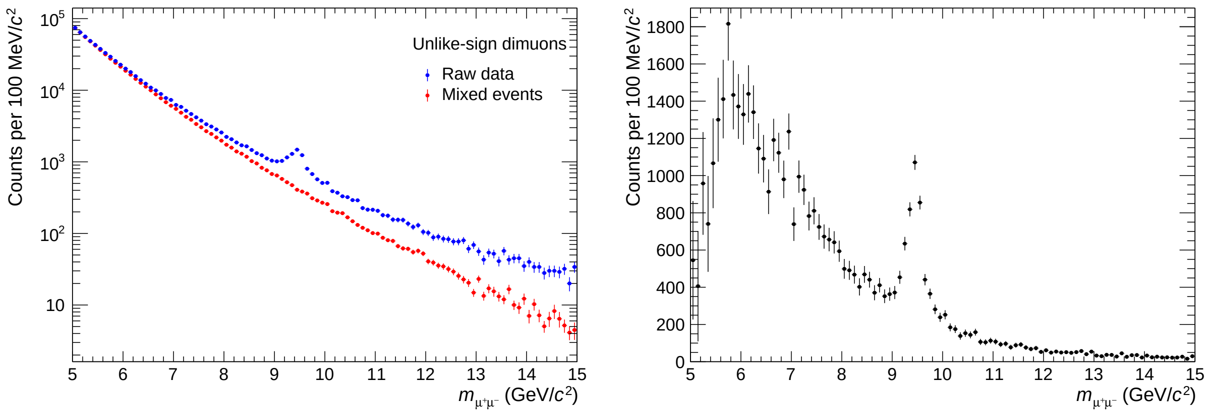

Figure 3.6: Unlike-sign dimuon invariant mass distribution (left) before and (right) after subtraction of the mixed-event continuum. The data points come from the full Run 2 data sample for the 0–90% most central collisions.

on each side. Its analytical formulation can be found in Appendix A.1. The high-mass tail is a response of the misalignment of the different detection elements. Due to the significant background in the Υ mass region, the four tail parameters have to be fixed in the procedure. The parameter values are obtained from the Monte Carlo simulations introduced in Section 3.3.1. These simulations allow the data-taking conditions of the apparatus to be reproduced. The significance $S/\sqrt{S+B}$, where S and B are respectively the signal and background integrals determined over 3σ around the peak mean value, of the Υ(1S) signal is sufficient to let the mean $m_{\Upsilon(1\mathrm{S})}$ and the width $\sigma_{\Upsilon(1\mathrm{S})}$ of the Gaussian core free in the fit. For the excited states, these variables are constrained like

$$m_{\Upsilon(\mathrm{nS})} = m_{\Upsilon(1\mathrm{S})} \times \frac{m^{\mathrm{PDG}}_{\Upsilon(\mathrm{nS})}}{m^{\mathrm{PDG}}_{\Upsilon(1\mathrm{S})}}, \quad \sigma_{\Upsilon(\mathrm{nS})} = \sigma_{\Upsilon(1\mathrm{S})} \times \frac{\sigma^{\mathrm{MC}}_{\Upsilon(\mathrm{nS})}}{\sigma^{\mathrm{MC}}_{\Upsilon(1\mathrm{S})}} \quad (\mathrm{n} = 2, 3), \tag{3.2}$$

where “PDG” labels the world-averaged values tabulated by the Particle Data Group [1]. The mass scaling with the excited-to-ground state ratio should propagate the potential reconstruction biases. For the width, we suppose that any difference in the signal resolution would be reproduced by the Monte Carlo simulation. The width scaling ratios obtained in the Pb–Pb study approximately amount to 1.04 and 1.07 for Υ(2S) and Υ(3S) respectively. In the pp case, the results are 1.05 and 1.08. These values are compatible with the mass ratios[§]. The tail parameters are equal for the three CB2 distributions modelling each of the resonances. Finally, we describe the background shape with empirical functions listed in the next part. The normalisation factors of the signal shapes and of the background functions are free parameters of the fit model. This fitting procedure is the same irrespective of the kinematic region studied, the analysis or the period of Pb–Pb data taking.

Example fits for the two collision systems are shown in Figure 3.7. Although the fit is performed in the integrated acceptance, the number of Υ mesons extracted from the proton–proton data is relatively low. The number of events will limit the differential study to a few p_{T} and rapidity intervals. Regarding the Pb–Pb analysis, the event-mixing technique improves the estimate of the background. Invariant mass distributions for several

---

[§] At first order, the mass resolution evolves linearly with the invariant mass.

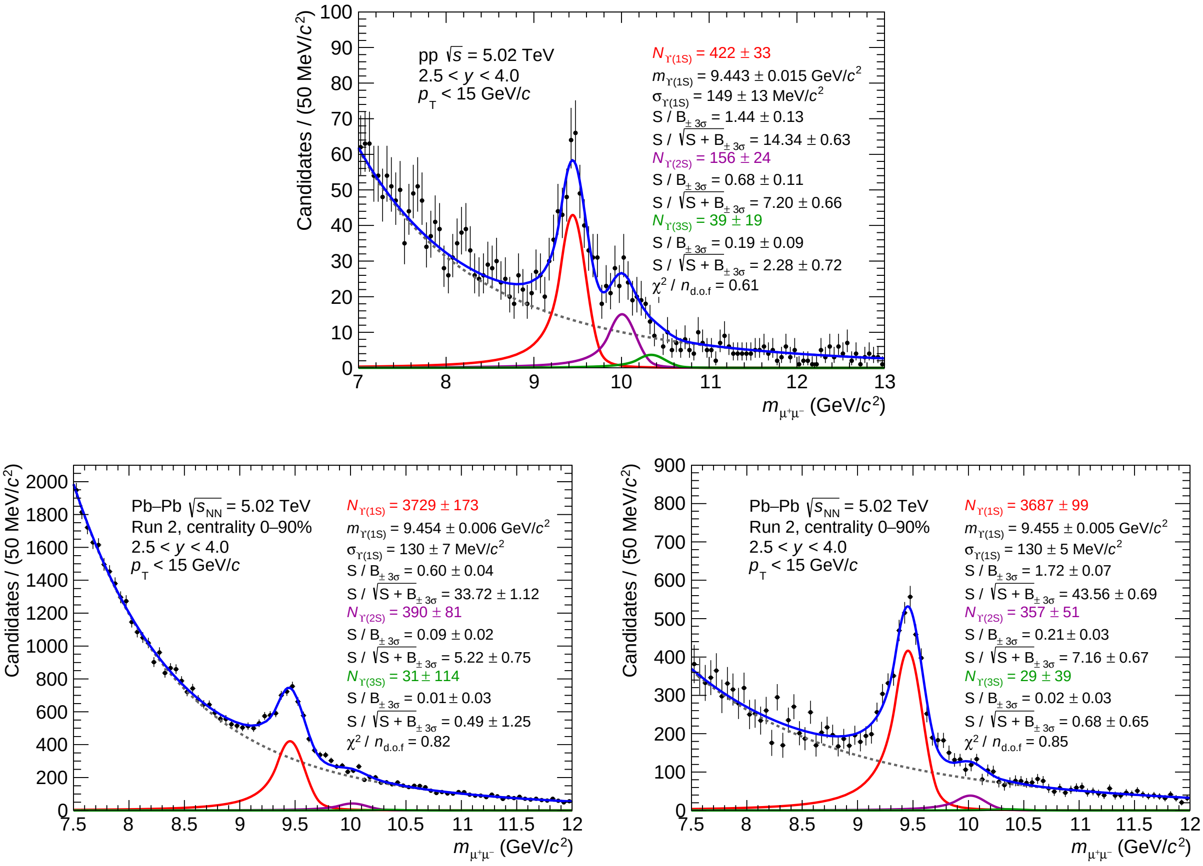

Figure 3.7: Log-likelihood fits to unlike-sign dimuon invariant mass spectra of (top) pp and (bottom) Pb–Pb collisions. The lower panels show results before and after subtraction of the mixed-event distribution. The red, magenta and green solid curves represent the ϒ(1S), ϒ(2S) and ϒ(3S) signal shapes respectively. The dashed grey lines correspond to background functions. The sum of these contributions is drawn with a blue solid line.

centrality classes can be found in Figure 3.8. The signal-to-background ratio decreases with the strong increase of the combinatorial component towards central collisions. The significance is sufficient to extract the ϒ(1S) yield for the 70–90% most peripheral events. The number of ϒ(3S) signal is compatible with 0 within the large statistical uncertainty.

3.2.3 Systematic uncertainties

Along the description of the procedure, we may have introduced biases on the components of the fitting model. The choice of some constraints does not rely on any physical argument. Each source of uncertainty must be studied in order to estimate the impact on the signal extraction.

Set of tail parameters

Due to the significant background in the ϒ mass region, the tail parameters of the CB2 distributions cannot be left free in the fit. These parameters are fixed to values obtained from the signal shape reconstructed in Monte Carlo simulations wherein detector effects

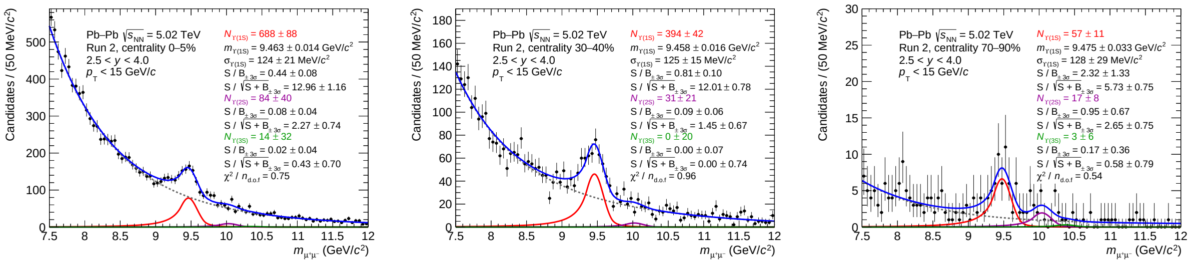

(a) 0–5% centrality (b) 30–40% centrality (c) 70–90% centrality

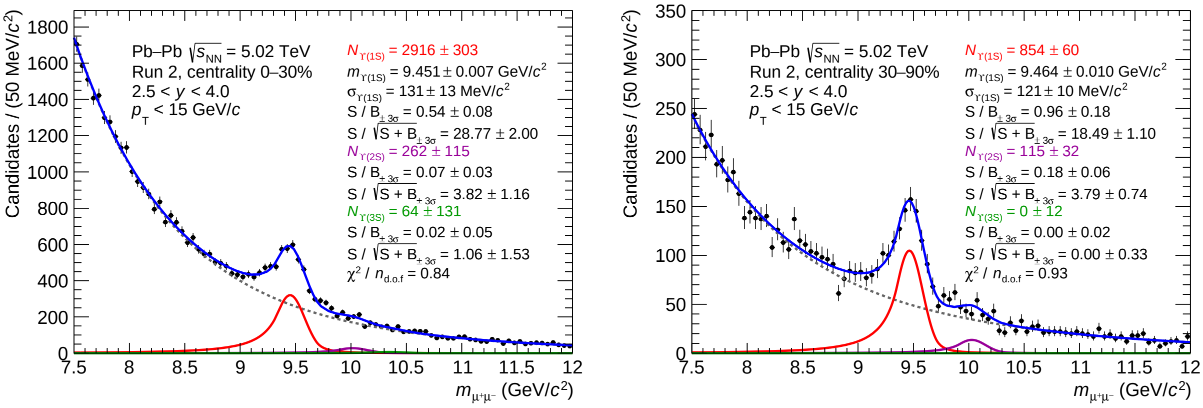

(d) 0–30% centrality (e) 30–90% centrality

Figure 3.8: Raw dimuon invariant mass spectra for various Pb–Pb collision centrality classes, from central to peripheral intervals (from left to right). The lower panels show the distributions where a Υ(2S) signal can be extracted. The legend is the same than for Figure 3.7.

are replicated. Traditionally, the passage of particles through material is handled by the Geant transport code. In the Pb–Pb analysis, the tail parameters are estimated alternatively from MC simulations using Geant3 [50] and Geant4 [51] packages. All the numerical values are tabulated in Appendix A.1. The reconstructed signal shapes are compared in Figure 3.9. The left tail distribution extends down to low masses because of multiple scatterings inside the front absorber as well as radiative decays of muons.

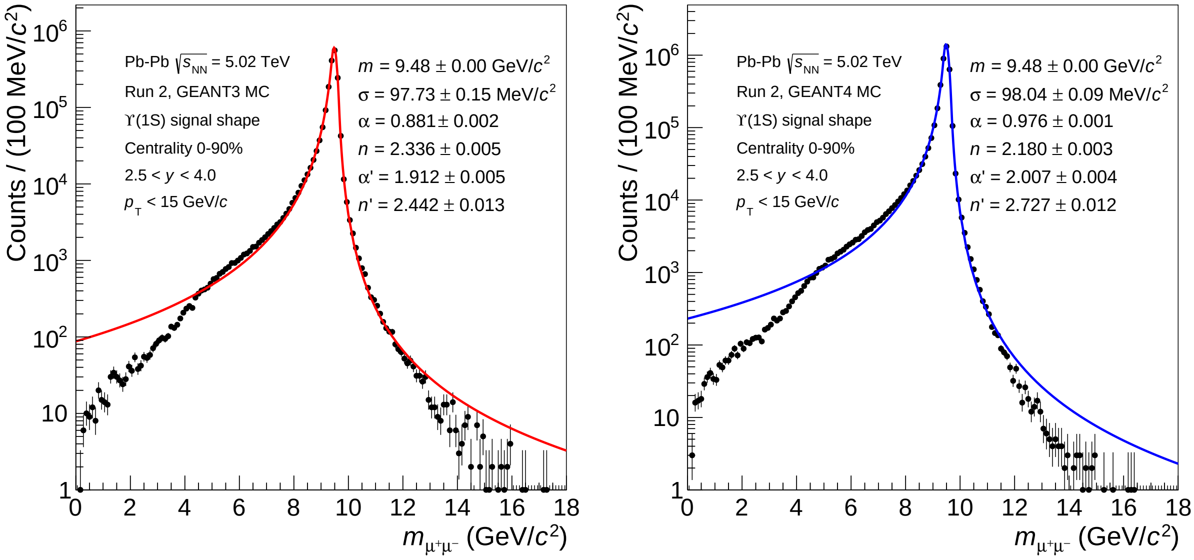

(a) Geant3 (b) Geant4

Figure 3.9: CB2 fit of the reconstructed Υ(1S) signal shape in Monte Carlo simulations for Pb–Pb collisions. The signal parameters are listed in the top-right corner of each panel. The quoted uncertainties denote the limited size of the simulation sample.

In the pp-collisions study, the default set of tail parameters originates from MC simulations with Geant3 as transport code. We also consider these parameters for the Pb–Pb analysis. Another set is obtained from the large samples of 13 TeV data‡ where the tail parameters can be left free in the fitting procedure. To do so, random CB2 distributions are generated based on the covariance matrix and the uncertainties returned by the fit result. The created sets displayed in Figure 3.10 are then used to fit the $\sqrt{s}$ = 5.02 TeV invariant mass spectrum for a reference fitting model. The systematic uncertainty attributed to the set of tail parameters in pp collisions is estimated as the root mean square (RMS) of these fit results. It amounts to 4.7%, 6.1% and 14.5% for Υ(1S), Υ(2S) and Υ(3S), respectively. These values are the same for the differential study and are added separately.

The tail parameters are extracted for each kinematic interval considered in the present analyses. For the Pb–Pb study as a function of the centrality, the tail parameters from pp $\sqrt{s}$ = 5.02 TeV events as well as from Geant4 are the integrated ones since the centrality dependence is not emulated in these simulation setups.

---

‡The corresponding integrated luminosity is about 2.9 pb^{-1}.

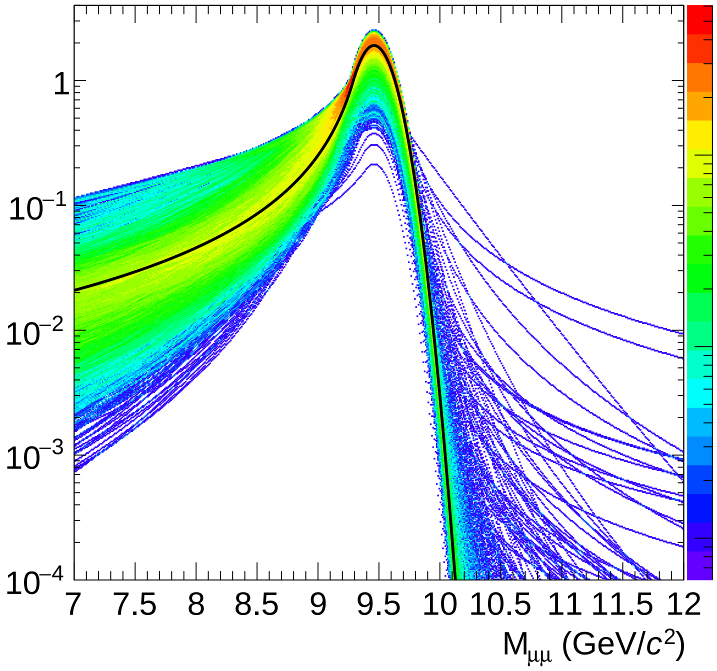

Figure 3.10: CB2 distributions generated from the fit result of the signal extraction in pp collisions at $\sqrt{s} = 13$ TeV. The black line represents the average distribution.

Width scaling ratio

The width of the two excited states is constrained to the Υ(1S) signal shape, cf. equation 3.2, assuming a linear proportionality with the ratio of the mass resolutions obtained from the Monte Carlo simulation. We test this relation for three limits, namely

- *simple scaling* $\rightarrow \sigma_{\Upsilon(\mathrm{nS})} = \sigma_{\Upsilon(1\mathrm{S})} \times \frac{\sigma^{\mathrm{MC}}_{\Upsilon(\mathrm{nS})}}{\sigma^{\mathrm{MC}}_{\Upsilon(1\mathrm{S})}}$,
- *no scaling* $\rightarrow \sigma_{\Upsilon(\mathrm{nS})} = \sigma_{\Upsilon(1\mathrm{S})}$,
- *double scaling* $\rightarrow \sigma_{\Upsilon(\mathrm{nS})} = \sigma_{\Upsilon(1\mathrm{S})} \times (2 \cdot \frac{\sigma^{\mathrm{MC}}_{\Upsilon(\mathrm{nS})}}{\sigma^{\mathrm{MC}}_{\Upsilon(1\mathrm{S})}} - 1)$.

The second is the extreme case in which the resolutions are equivalent. The last limit is chosen arbitrarily because there is no maximum value that the scaling factor can take[‖]. The values correspond to a 5% variation of the detector resolution, accounting for residual discrepancies between Monte Carlo and data as in the p–Pb analysis [52]. Although this source of uncertainty is not well controlled, the contribution on the signal extraction is small with respect to the other ones. The procedure is the same in both analysis.

Background function

In Pb–Pb collisions, the background dominates over the Υ signal of the raw spectrum. The composition of the dimuon continuum discussed in Section 3.2.1 is complex and

---

[‖] Up to a certain physical point.

not uniform with the invariant mass. To model the background shape, we use ad-hoc functions with four free parameters: the sum of two decreasing exponentials (2Exp) and the so-called variable-width Gaussian (VWG). As its name suggests, the latter consists of a Gaussian function whose width varies linearly with the invariant mass. These functions, formulated in Appendix A.2, are employed in all kinematic regions except the two highest p_{T} bins. From Figure 3.11, one observes that the slope in the low-mass region becomes convex for $p_{\mathrm{T}} \gtrsim 5$ GeV/c. This change is explained by the muons from pion and kaon decays making up the combinatorial background and dominating at low invariant mass and low transverse momentum. For these two bins, we replace the sum of exponentials by the product of an exponential with a second-order polynomial. After subtraction of the mixed-event distribution, the residual background is fitted with a single exponential (Exp) and a power law (Pow). In the pp analysis, the functions are the sum of two exponentials, a single exponential as well as a power law.

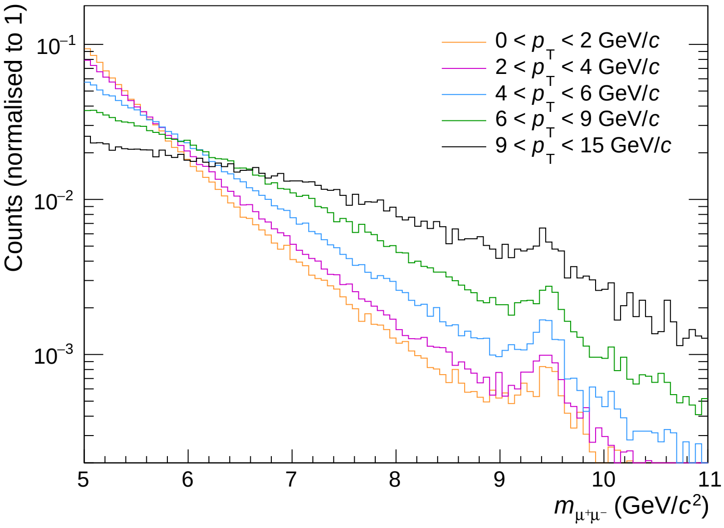

Figure 3.11: Invariant mass distributions in Pb–Pb collisions for different dimuon p_{T} ranges. The distributions are normalised to their integral.

Summary

The fits are alternatively performed within two mass windows to cover invariant mass regions where the background shape is different. The ranges are optimised to be extreme enough while guaranteeing the fit quality.

We evaluate the uncertainties on the signal extraction from the combination of all the tests aforementioned. In total, 18 and 72 fits are performed in the proton–proton and Pb–Pb analyses respectively. A result is considered if the minimisation has converged and if the quality of the covariance and error matrices is "accurate" according to RooFit. The global result is taken as the linear average of the individual fit results. The statistical and systematic uncertainties are calculated as

$$\sigma_{\mathrm{stat}} = \frac{\sum_i^n \sigma_i}{n}, \quad \sigma_{\mathrm{syst}} = \sqrt{\frac{\sum_i^n (x_i - \mu)^2}{n-1}}, \tag{3.3}$$

where x_i is the result of the test i, σ_i the statistical error returned by the fit, n the number of tests and μ the linear average of the test results.

One may notice some constraints of the fitting model have not been discussed. It turns out that the mass scaling of the equation 3.2 has a negligible contribution with respect to the other sources of uncertainties. For the signal shape, the ALICE analyses on quarkonium production generally employ the NA60 distribution [53] as an alternative to the CB2. However, the NA60 has more parameters and the large overlap of the Υ signal shapes leads to fit convergence issues. That is why only the CB2 is considered in the present studies. Since the two distributions differ by the description of the tails, using different sets of tail parameters should cover the uncertainty for the signal function.

3.2.4 Results

The number of Υ states is extracted as a function of the dimuon rapidity y and transverse momentum p_T, as well as within centrality classes for the Pb–Pb collisions. We choose the differential kinematic intervals wherein the significance of Υ(1S) is at least 5 and better than 3 for Υ(2S). Results can be found in Tables 3.6 and 3.7 for the centrality classes, Tables 3.8, and 3.9 for rapidity intervals and Tables 3.10 and 3.11 for p_T ranges. Let us focus on the centrality-integrated results obtained in the Pb–Pb data analysis. The numerical values are reported in Table 3.4 for the different periods. The results are proportional to the number of CMUL-triggered events except for Υ(2S) in LHC18q. This *excess* can be interpreted as a statistical fluctuation because the significance is only about two in the other periods. It is also observed in Table 3.5 for the excited-to-ground state yield ratio. We evaluate the latter quantity on a fit-by-fit basis in order to account for correlations in the procedure.

Period	$N_{\Upsilon(1S)} \pm$ stat $\pm$ syst	$N_{\Upsilon(2S)} \pm$ stat $\pm$ syst
LHC15o	1173 ± 69 (5.9%) ± 50 (4.3%)	68 ± 35 (50.6%) ± 31 (45.2%)
LHC18q	950 ± 63 (6.6%) ± 54 (5.7%)	146 ± 35 (23.8%) ± 16 (10.9%)
LHC18r	1454 ± 77 (5.3%) ± 59 (4.1%)	91 ± 46 (50.8%) ± 25 (27.1%)
Run 2	3581 ± 119 (3.3%) ± 156 (4.4%)	325 ± 61 (18.8%) ± 60 (18.4%)

Table 3.4: Raw number of Υ(1S) and Υ(2S) extracted per period of Pb–Pb data taking. The quoted statistical and systematic uncertainties are evaluated via the formulas of the equation 3.3.

Although at least partially correlated with the statistical uncertainty, the systematic uncertainties on the Υ(2S) yield are relatively important. From the distribution of the fitting results in Figure 3.12, the main source of uncertainty is the difference between the direct and event-mixing methods. The point-to-point variation is due to the change of the background shape in the two invariant mass windows considered. The statistical uncertainties are smaller for the results after background subtraction as the fitting model contains less free parameters. However, this improvement is compensated by the description of the residual background. It seems that the single exponential fits systematically

Period	$N_{\Upsilon(2S)}/N_{\Upsilon(1S)} \pm$ stat $\pm$ syst
LHC15o	0.058 ± 0.030 (52.0%) ± 0.025 (42.9%)
LHC18q	0.154 ± 0.038 (24.4%) ± 0.014 (9.2%)
LHC18r	0.062 ± 0.029 (46.3%) ± 0.016 (25.9%)
Run 2	0.090 ± 0.017 (19.2%) ± 0.014 (15.2%)

Table 3.5: Υ(2S)-to-Υ(1S) yield ratio per period of Pb–Pb data taking.

Centrality class	$N_{\Upsilon(1S)} \pm$ stat $\pm$ syst
0–5%	699 ± 61 (8.7%) ± 34 (4.9%)
5–10%	601 ± 53 (8.7%) ± 41 (6.9%)
10–15%	464 ± 44 (9.5%) ± 22 (4.6%)
15–20%	359 ± 37 (10.4%) ± 27 (7.4%)
20–30%	642 ± 50 (7.8%) ± 39 (6.1%)
30–40%	384 ± 34 (8.9%) ± 15 (3.9%)
40–50%	232 ± 27 (11.7%) ± 11 (4.8%)
50–70%	164 ± 22 (13.5%) ± 7 (4.3%)
70–90%	52 ± 10 (20.1%) ± 4 (7.4%)

Table 3.6: Raw number of Υ(1S) extracted in centrality classes of Pb–Pb data, for the $2.5 < y < 4.0$ and $p_{\mathrm{T}} < 15$ GeV/c ranges.

underestimate the number of Υ(2S). The same observation applies to Υ(1S), hence to the excited-to-ground state ratio as well. This raises the question of whether the event-mixing technique is suited to our study. It benefits significantly to the Υ(1S) signal extraction in central collisions where the combinatorial background is the most important. Conversely, the method loses interest for peripheral events and is even for rapidity and p_{T}-differential intervals. Regarding the excited states, the resulting systematic uncertainty for Υ(2S) is much larger than the statistical gain while the impact for Υ(3S) is not perceptible.

3.2.5 Upper limit on Υ(3S) signal in Pb–Pb collisions

As expected, the production of the Υ(3S) excited state is strongly suppressed. No signal is observed in any of the kinematic regions accessible in the present Pb–Pb data sample. The total number of candidates amounts to 13 ± 61 (stat) ± 14 (syst). To have an idea of the magnitude of the suppression, we estimate an upper limit on the Υ(3S) raw yield. Traditionally, one defines confidence intervals covering the *true* value up to a certain degree of belief. Several methods exist depending on the purpose or the experimental context, most of them based on prior hypotheses for the probability distribution of the parameter

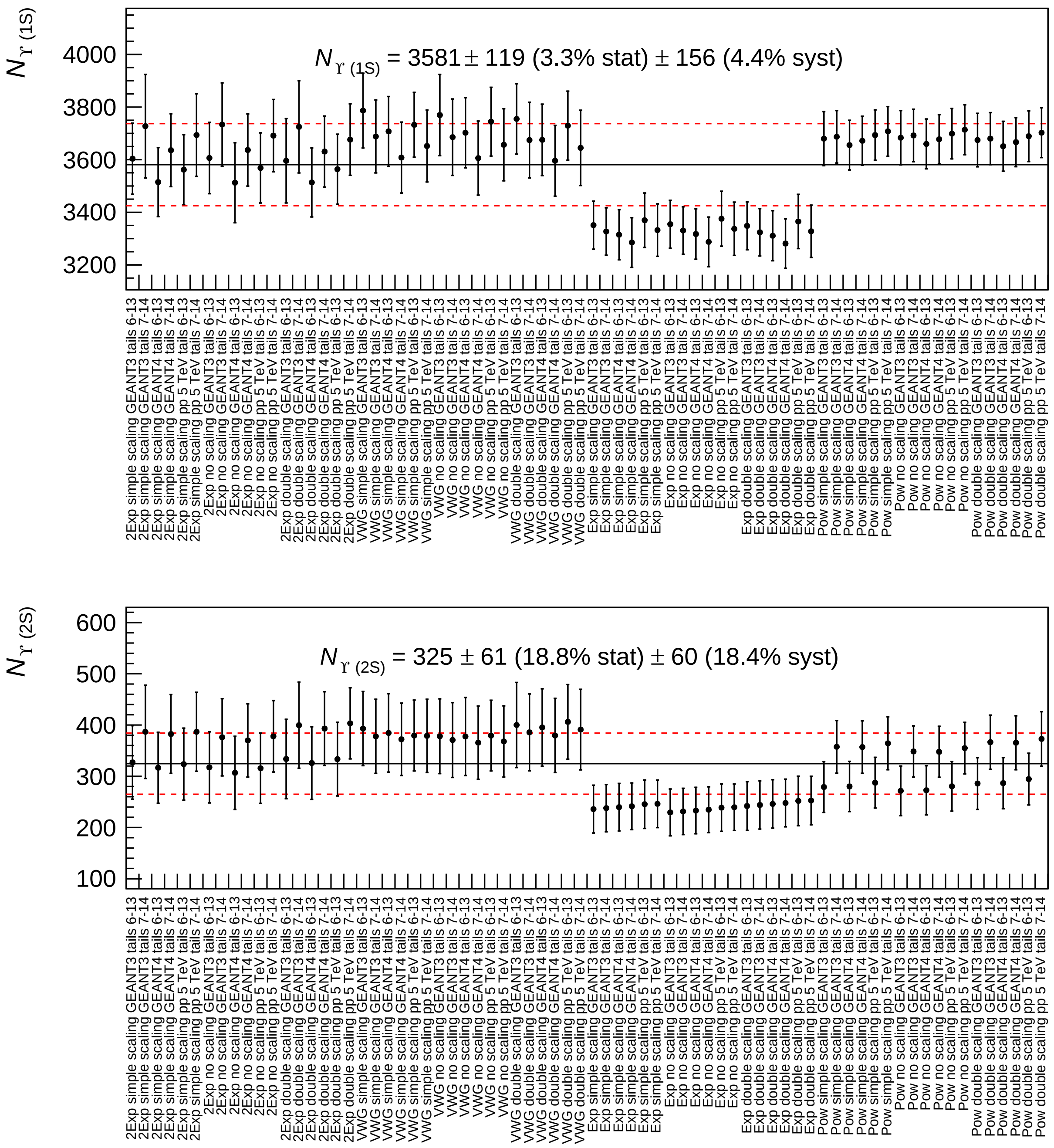

Figure 3.12: Number of Υ(1S) and Υ(2S) extracted in the full Run 2 data set, for each combination of fitting test mentioned in Section 3.2.3. The vertical error bars represent the statistical uncertainties returned by the fits. The black line shows the linear average of the results while the dashed red lines correspond to ±1 σ_{syst} of the signal extraction procedure.

Centrality class	$N_{\Upsilon(2S)} \pm \mathrm{stat} \pm \mathrm{syst}$	$N_{\Upsilon(2S)}/N_{\Upsilon(1S)} \pm \mathrm{stat} \pm \mathrm{syst}$
0–30%	216 ± 53 (24.7%) ± 51 (23.4%)	0.078 ± 0.020 (25.2%) ± 0.016 (20.4%)
30–90%	107 ± 27 (25.3%) ± 15 (14.0%)	0.129 ± 0.033 (25.6%) ± 0.014 (10.9%)

Table 3.7: Raw number of Υ(2S) and Υ(2S)-to-Υ(1S) yield ratio extracted in centrality classes of Pb–Pb data, for the $2.5 < y < 4.0$ and $p_T < 15$ GeV/c ranges.

Rapidity interval	$N_{\Upsilon(1S)} \pm \mathrm{stat} \pm \mathrm{syst}$
$2.5 < y < 2.8$	508 ± 50 (9.9%) ± 52 (10.2%)
$2.8 < y < 3.1$	1152 ± 66 (5.8%) ± 41 (3.6%)
$3.1 < y < 3.3$	830 ± 60 (7.3%) ± 33 (3.9%)
$3.3 < y < 3.6$	808 ± 50 (6.2%) ± 32 (3.9%)
$3.6 < y < 4.0$	325 ± 34 (10.6%) ± 17 (5.4%)

Table 3.8: Raw number of Υ(1S) extracted in rapidity intervals of Pb–Pb data, for the 0–90% centrality class and for $p_T < 15$ GeV/c.

Rapidity interval	$N_{\Upsilon(2S)} \pm \mathrm{stat} \pm \mathrm{syst}$	$N_{\Upsilon(2S)}/N_{\Upsilon(1S)} \pm \mathrm{stat} \pm \mathrm{syst}$
$2.5 < y < 3.3$	129 ± 48 (37.1%) ± 50 (39.0%)	0.054 ± 0.021 (39.0%) ± 0.020 (37.9%)
$3.3 < y < 4.0$	170 ± 34 (20.1%) ± 16 (9.7%)	0.140 ± 0.031 (22.5%) ± 0.008 (5.5%)

Table 3.9: Raw number of Υ(2S) and Υ(2S)-to-Υ(1S) yield ratio extracted in rapidity intervals of Pb–Pb data, for the 0–90% centrality class and for $p_T < 15$ GeV/c.

p_T range [GeV/c]	$N_{\Upsilon(1S)} \pm \mathrm{stat} \pm \mathrm{syst}$
$0 < p_T < 2$	634 ± 57 (9.0%) ± 54 (8.5%)
$2 < p_T < 4$	1173 ± 67 (5.7%) ± 65 (5.5%)
$4 < p_T < 6$	830 ± 51 (6.2%) ± 30 (3.6%)
$6 < p_T < 9$	548 ± 49 (9.0%) ± 50 (9.1%)
$9 < p_T < 15$	362 ± 43 (12.0%) ± 26 (7.1%)

Table 3.10: Raw number of Υ(1S) extracted in p_T ranges of Pb–Pb data, for the 0–90% centrality class and in the $2.5 < y < 4.0$ interval.

p_{T} range [GeV/c]	$N_{\Upsilon(2\mathrm{S})} \pm \mathrm{stat} \pm \mathrm{syst}$	$N_{\Upsilon(2\mathrm{S})}/N_{\Upsilon(1\mathrm{S})} \pm \mathrm{stat} \pm \mathrm{syst}$
$0 < p_{\mathrm{T}} < 4$	130 ± 41 (31.4%) ± 34 (25.8%)	0.071 ± 0.023 (32.2%) ± 0.015 (21.3%)
$4 < p_{\mathrm{T}} < 15$	186 ± 48 (25.6%) ± 16 (8.5%)	0.104 ± 0.027 (25.6%) ± 0.009 (8.5%)

Table 3.11: Raw number of Υ(2S) and Υ(2S)-to-Υ(1S) yield ratio extracted in p_{T} ranges of Pb–Pb data, for the 0–90% centrality class and in the $2.5 < y < 4.0$ interval.

of interest*. Considering our situation, we estimate the upper limit via the Feldman-Cousins approach [54]. This method has the advantage of avoiding non-physical regions, i.e. the number of Υ(3S) cannot take negative values. In addition, the free parameters of our fitting model are incorporated as *nuisance parameters* within the limit estimator.

For practical reasons, the upper limit cannot be evaluated for all the test combinations. We thus select the fitting model giving the largest statistical uncertainty for the Υ(3S) yield and the worst significance. This strategy does not account for the uncertainties on the signal extraction procedure, in particular for the description of the background shape. However, the statistical uncertainty dominates all other sources of unknowns. By placing ourselves in the worst-case scenario, we are overestimating the upper limit. A rigorous evaluation would require a complete analysis on its own, as carried out for the suppression of ψ(2S) production [55]. Integrated in the total acceptance, the number of Υ(3S) is inferior to 137 at a 95% confidence level. This estimation is in line with the interval obtained with the profile likelihood ratio shown in Figure 3.13.

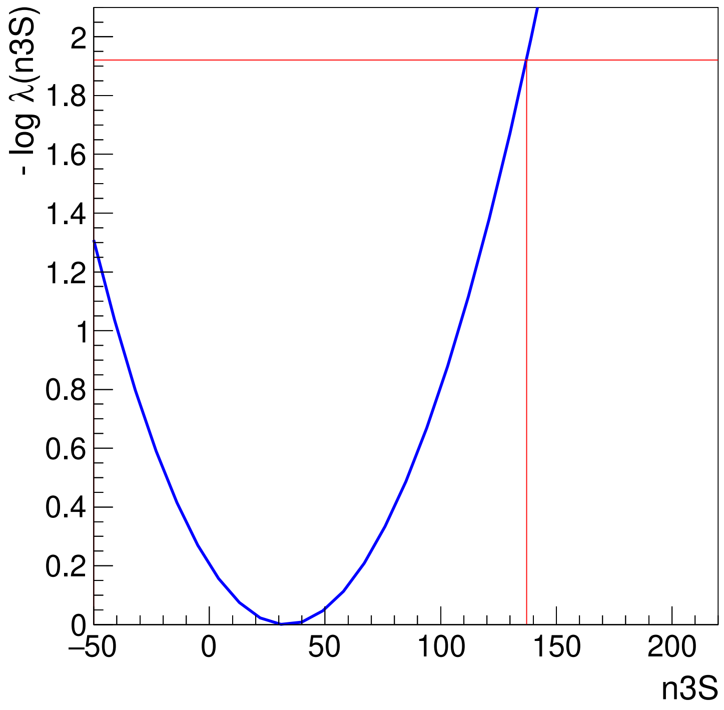

Figure 3.13: Profile likelihood ratio of the number of Υ(3S) signal in Pb–Pb collisions. The red straight lines define the 95% confidence interval.

---

*See the PDG's review on *Statistics* [1] to go further.

3.3 Acceptance and efficiency corrections

The results presented in the previous section correspond to an estimate of the number of Υ states reconstructed by the muon spectrometer. These raw yields must then be corrected for the geometrical acceptance and the detection efficiency of the decay muons, noted $A \times \varepsilon$. This correction factor is evaluated from dedicated Monte Carlo simulations wherein the data-taking conditions can be reproduced.

3.3.1 Configuration of the Monte Carlo simulations

First, Υ signals are generated according to rapidity and p_{T} distributions obtained from the interpolation of CDF [56] and LHCb [57] measurements. We assume an unpolarised production as the available data suggest [58, 59]. The generated resonances are then decayed into muon pairs using the EvtGen package [60], together with PHOTOS [61] to account for final-state radiation. Muons are transported through a realistic modelling of the ALICE apparatus via the GEANT3 code [50]. The event and track reconstruction algorithm is identical to the one for data. Monte Carlo simulations are processed on a run-by-run basis in order to replicate the variation of the detector performance during the data takings.

In the simulation of Pb–Pb collisions, we emulate the nuclear modification of the initial distributions. The p_{T} and rapidity input shapes are modified by nPDF parametrisations. The Υ dimuon decays are *embedded* into recorded minimum bias events. This approach allows us to consider the occupancy of the detection elements which increases with increasing event multiplicity, thus for the most central collision events.

3.3.2 Evaluation and results

The acceptance and efficiency correction, in a given kinematic interval, is calculated as the ratio of the number of reconstructed Υ mesons over the number of generated ones. We select the Υ reconstructed from muon tracks as in Section 3.1.3. The averaged efficiencies are weighted by the number of CMUL events per run to account for the time evolution of the detector response and for the relative amount of data available in each run. Figure 3.14 shows the $A \times \varepsilon$ of Υ(1S) as a function of the run number for a Pb–Pb data taking period. The large drops of efficiency are caused by trips of high-voltage channels of the muon tracking chambers. In the Pb–Pb analysis, we also weight by the mean number of binary collisions $\langle N_{\mathrm{coll}} \rangle$ in each centrality interval[¶] since embedding simulations are carried out with minimum bias events.

The integrated values are reported in Table 3.12 for the two analyses. The results are found to be similar for the three resonances and larger for proton–proton collisions. Looking at the Pb–Pb data taking periods, the efficiencies slightly decrease with time. This observation can be explained by more frequent high-voltage trips, especially at the end of Run 2. The $A \times \varepsilon$ of Υ(3S) is not available for the LHC15o period because the resonance was not incorporated in the simulation at that time. That is why we quote the value averaged over the 2018 samples. As the results are similar for the three resonances, the efficiency of Υ(3S) in Run 2 will be taken equal to the value for Υ(1S).

[¶] assuming that Υ production scales with the number of hard nucleon–nucleon scattering

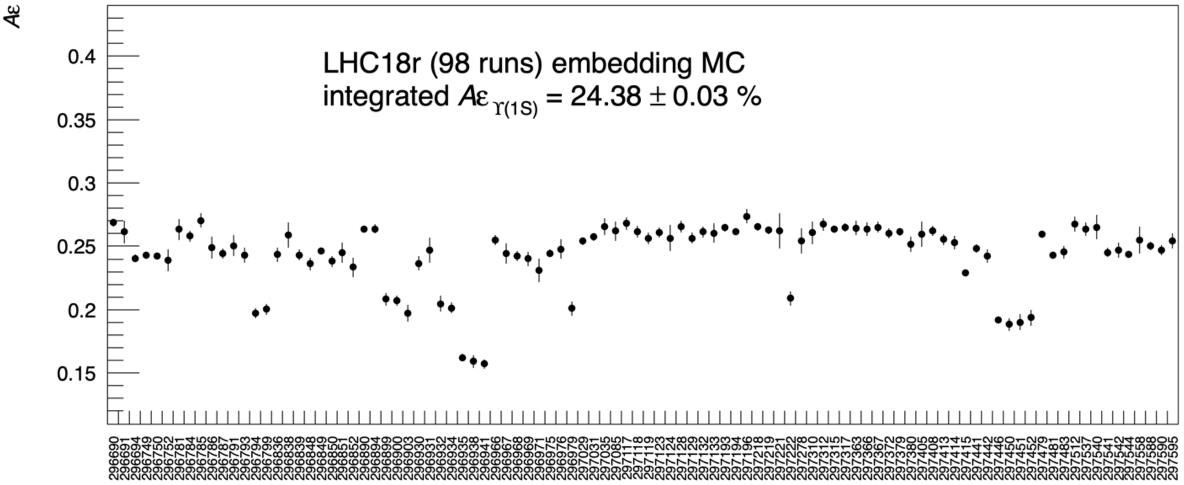

Figure 3.14: Acceptance times efficiency of Υ(1S) as a function of the run number in the LHC18r period. The quoted result corresponds to the run and centrality-weighted average. The vertical error bars denote the limited size of the simulated sample.

Period	$(A \times \varepsilon)_{\Upsilon(1S)} \pm$ stat	$(A \times \varepsilon)_{\Upsilon(2S)} \pm$ stat	$(A \times \varepsilon)_{\Upsilon(3S)} \pm$ stat
pp 2017	28.93 ± 0.05	28.79 ± 0.06	28.95 ± 0.11
LHC15o	26.83 ± 0.03	26.68 ± 0.04	-
LHC18q	25.56 ± 0.03	25.44 ± 0.04	25.65 ± 0.05
LHC18r	24.38 ± 0.03	24.48 ± 0.03	24.58 ± 0.04
Run 2	25.72 ± 0.02	25.65 ± 0.02	25.03 ± 0.03 (2018)

Table 3.12: Weighted-averaged integrated $A \times \varepsilon$ (in %) of Υ states for the different periods. The statistical uncertainties denote the limited size of the simulated samples.

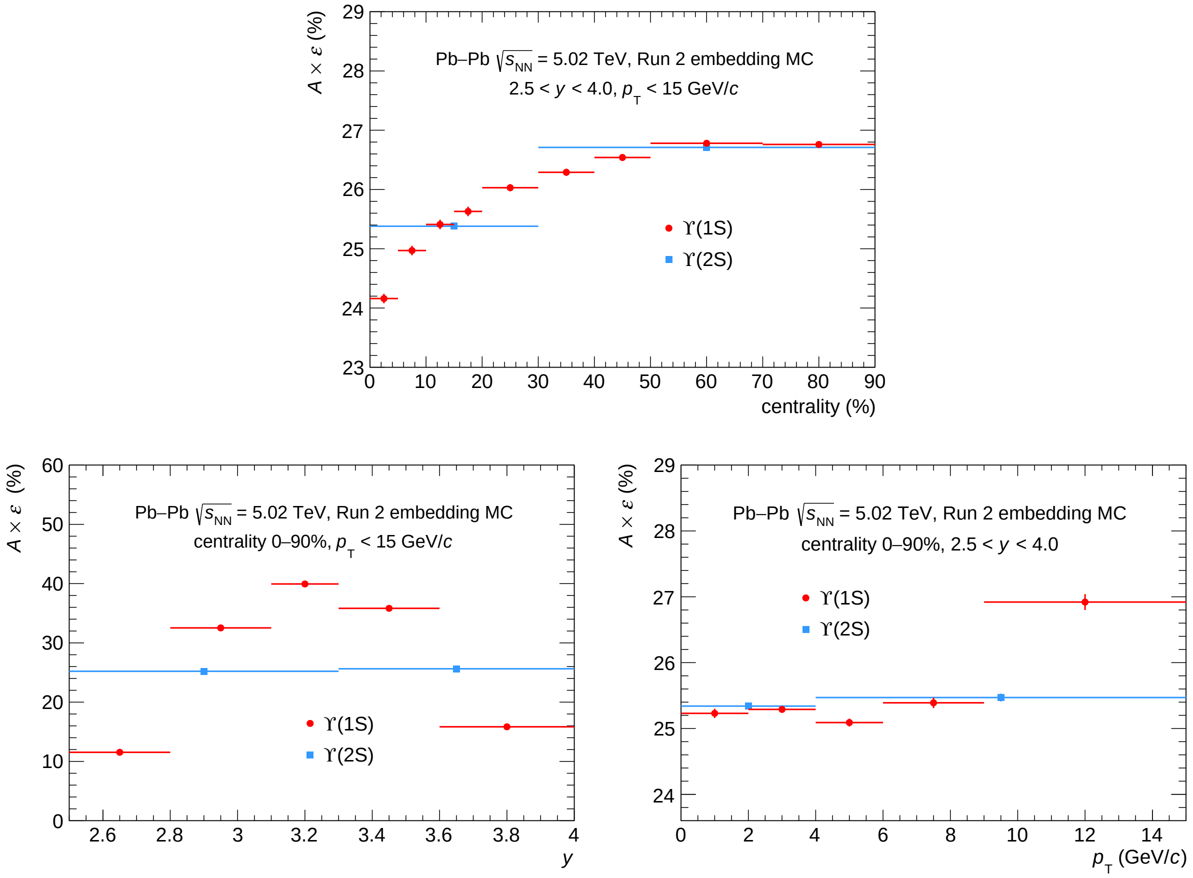

Figure 3.15: Acceptance and efficiency corrections in (top) centrality classes, (left) rapidity intervals and (right) p_{T} ranges for $\Upsilon(1\mathrm{S})$ and $\Upsilon(2\mathrm{S})$ in Pb–Pb collisions. The vertical error bars denote the limited size of the simulated samples.

The distribution of $A \times \varepsilon$ in differential intervals for Pb–Pb collisions is represented in Figure 3.15. We observe a relative decrease of about 10% from peripheral to central collisions. This trend is due to the rise of the occupancy in the muon chambers for high-multiplicity events. The variations as a function of the rapidity reflect the geometrical acceptance of the muon spectrometer. The reconstruction efficiency increases with dimuon p_{T} as the mean transverse momentum of the decay muons shifts further away from the trigger threshold. These dependencies are similar in the pp analysis.

3.3.3 Systematic uncertainties

We attribute a systematic uncertainty to each stage of the evaluation of the acceptance and efficiency correction. Since the sources are identical for the $\Upsilon(1\mathrm{S})$ and $\Upsilon(2\mathrm{S})$ states, their uncertainties cancel out in the yield ratio.

Monte Carlo input shapes

As mentioned in the beginning of the present section, the initial distributions for the generation of Υ signals are obtained from previous measurements. These input shapes do not account for correlations between the p_{T} and rapidity-differential measurements, nor for their statistical uncertainties. We can study these two contributions separately in the pp analysis. For the correlation, we reweight each initial rapidity (p_{T}) distribution by the ratio of p_{T} (y)-differential cross section over the y(p_{T})-integrated one from LHCb measurements at $\sqrt{s} = 13$ TeV [62]. The $A\times\varepsilon$ correction is evaluated for each combination of distributions and the systematic uncertainty is taken as the root mean square (RMS) of the results. For the other source, we generate several distributions by smearing the original ones within the statistical uncertainties of the present measurements, according to a Gaussian drawing. Again, the corresponding systematic uncertainty is the RMS of the $A \times \varepsilon$ obtained with these new distributions. The numerical values found for the two contributions are reported in Table 3.13. The final systematic uncertainties on the MC input shapes are the quadratic sums of the two contributions. The values are the same for all Υ states in the pp analysis.

Rapidity interval	p_{T} range [GeV/c]	Source of uncertainty	
		p_{T}-y correlation	statistical uncertainty
$2.5 < y < 4.0$	$0 < p_{\mathrm{T}} < 15$	0.76	1.50
$2.5 < y < 3.25$		0.97	2.00
$3.25 < y < 4.0$		0.84	3.42
$2.5 < y < 4.0$	$0 < p_{\mathrm{T}} < 2$	0.53	1.57
	$2 < p_{\mathrm{T}} < 4$	0.84	1.47
	$4 < p_{\mathrm{T}} < 6$	0.51	1.38
	$6 < p_{\mathrm{T}} < 15$	0.93	1.35

Table 3.13: Systematic uncertainties (in %) of the two contributions on MC input shapes in proton–proton collisions.

For Pb–Pb collisions, we modify the signal distributions to emulate the nuclear modification in the initial state. The default input shape is the EKS98 parametrisation [63] implemented in the ALICE simulation framework. Here, we decide to assign the systematic uncertainty on the choice of nPDF set. Other simulations are produced with the EPS09 shadowing [64] or without any modification of the pp distributions. The $A\times\varepsilon$ corrections obtained from these simulations are shown in Figure 3.16. The uncertainty is estimated as the maximum relative difference between these results. It amounts to less than 1% in all differential intervals, whatever the Υ state, and is fully correlated with the centrality.

Tracking efficiency

Our estimate of the acceptance and efficiencies relies on Monte Carlo simulations, assuming that all the detector conditions during the data taking are reproducible. In the following, we study the residual discrepancies with the data in order to assign systematic uncertainties. The latter are identical to all Υ states unless otherwise specified.

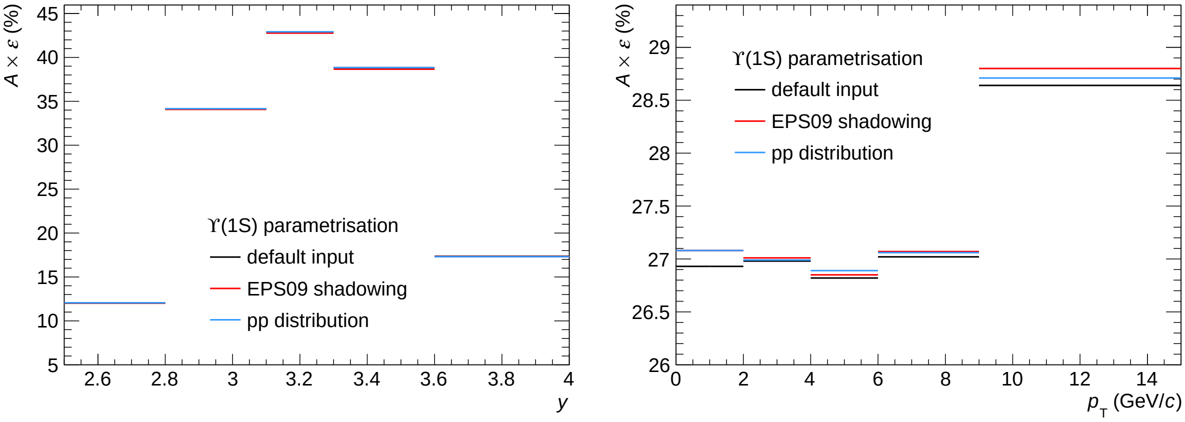

Figure 3.16: Acceptance and efficiency of Υ(1S) in (left) rapidity and (right) p_{T} intervals in Pb–Pb collisions, for the different initial distributions introduced in the text.

Let us start with the tracking efficiency, determined via the method detailed in the thesis [65]. This estimate is based on the reconstruction of single-muon tracks from data and MC simulations. The initial p_{T} and rapidity distributions are tuned on data to be the most realistic ones. This tuning procedure is done on a run-by-run basis, for different trigger classes and for several centrality classes. Reconstructed tracks must satisfy the quality criteria listed in Section 3.1.3. To determine the muon tracking efficiency, the method exploits the redundancy of the track information to evaluate the efficiency of each plane of tracking chambers individually. The overall efficiencies are compared via the ratio of data over MC results in Figure 3.17 for various muon selections and centrality classes. The systematic uncertainty on the muon tracking efficiency is defined such that almost all the points lie within two standard deviations from unity. In this example, the uncertainty is found to be 1.5%, hence 3% at the dimuon level. This factor 2 is conservative. The simulation of single muons does not account for correlations between them while they are naturally present in CMUL events. Consequently, we overestimate the systematic uncertainty as the discrepancy of the tracking efficiency between data and Monte Carlo simulations is artificially increased.

In summary, the systematic uncertainty related to the tracking efficiency is 3% for the three periods of Pb–Pb data taking. We consider that it is fully correlated with the centrality but uncorrelated as a function of p_{T} and rapidity. With the drop of tracking efficiency in high-multiplicity events, we add another source of uncertainty ranging from 0 to 1% from peripheral to the most central collisions. In the pp analysis, the tracking systematic uncertainty amounts to 2%.

Trigger efficiency

The systematic uncertainty on the trigger efficiency can be decomposed into two main contributions:

- **trigger response function**: the probability of triggering on a muon is continuous as a function of its measured transverse momentum. We investigate the difference of shape of the response function between data and MC simulations. The corresponding systematic uncertainty is taken as the relative difference of $A \times \varepsilon$ calculated

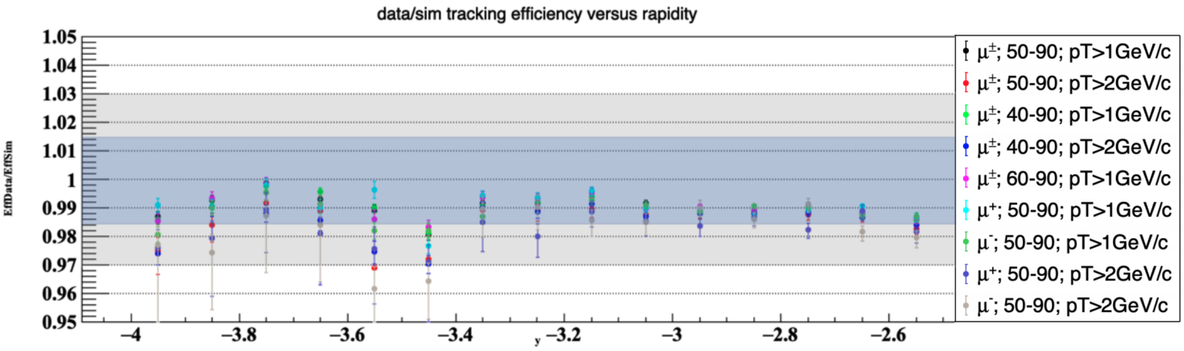

Figure 3.17: Ratio of muon tracking efficiency in data and MC simulations as a function of the rapidity for the 2018 Pb–Pb data-taking periods [66]. The points correspond to combinations of muon charge and p_{T} selections, as well as centrality classes, for CMSL triggered events. The blue and grey bands represent the one and two standard deviations from unity, respectively.

from simulations carried out with the two response functions. For the Υ states, it amounts to less than 1% as the mean p_{T} of the decay muons is far from the trigger threshold.

- **intrinsic efficiency of the trigger chambers**: by default, the MC simulations are performed with an efficiency map of each RPC local board obtained from data. We can create another map by varying the muon p_{T} selection and then running new simulations. The systematic uncertainty is estimated as the relative difference of the $A \times \varepsilon$ from the default and the modified efficiency maps. The result is 0.9% for proton–proton collisions, with minor fluctuations between differential intervals. The uncertainty is found to be larger in the Pb–Pb analysis and strongly depends on the dimuon p_{T} and rapidity.

The quadratic sum of these two sources is reported in Table 3.14 for Pb–Pb collisions. The systematic uncertainty on the trigger efficiency is correlated with the centrality and uncorrelated with p_{T} and rapidity for the two analyses.

Trigger-tracker matching condition

In Section 3.1.3, we require that a track reconstructed by the muon tracking system must match a tracklet in the trigger stations. This condition is based on a selection on the χ^2 of the matching between the two parts of the spectrometer. The reconstruction efficiency of muon tracks is studied as a function of this selection in data and MC simulations. The change of efficiency when varying the threshold within 6σ is taken as the systematic uncertainty. It amounts to 1% for dimuons in the two analyses as the selection value did not change during Run 2. We assume that this uncertainty is correlated with the centrality and uncorrelated as a function of p_{T} and rapidity.

Rapidity interavl	p_{T} range [GeV/c]	Systematic uncertainty (in %)
$2.5 < y < 4.0$	$0 < p_{\mathrm{T}} < 15$	3.0
$2.5 < y < 2.8$		4.0
$2.8 < y < 3.1$		3.5
$3.1 < y < 3.3$		3.2
$3.3 < y < 3.6$		3.0
$3.6 < y < 4.0$		1.5
$2.5 < y < 3.3$	$0 < p_{\mathrm{T}} < 15$	3.7
$3.3 < y < 4.0$		1.4
$2.5 < y < 4.0$	$0 < p_{\mathrm{T}} < 2$	2.6
	$2 < p_{\mathrm{T}} < 4$	1.6
	$4 < p_{\mathrm{T}} < 6$	1.2
	$6 < p_{\mathrm{T}} < 9$	1.1
	$9 < p_{\mathrm{T}} < 15$	0.5
$2.5 < y < 4.0$	$0 < p_{\mathrm{T}} < 4$	2.0
	$4 < p_{\mathrm{T}} < 15$	1.1

Table 3.14: Systematic uncertainty on the trigger efficiency in Pb–Pb collisions.

3.4 Event normalisation

Once corrected for acceptance and efficiency, the number of Υ states should be normalised to the total number of events analysed. However, the CMUL-triggered events constitute a subset of the minimum bias sample. To rectify this selection bias, we introduce a so-called normalisation factor F_{norm} in the conversion to an equivalent number of MB events like

$$N_{\text{equi MB}} = \sum_{\text{run } i} F^{i}_{\text{norm}} \times N^{i}_{\text{CMUL}}, \tag{3.4}$$

where N_{CMUL} corresponds to the number of opposite-charge dimuon counters in the 0–90% centrality range, after physics selection.

3.4.1 Normalisation factor

The normalisation factor can be calculated in several ways depending on the MB trigger considered. The approach is identical for both pp and Pb–Pb collision systems.

Offline methods

The first method consists of computing the *direct* ratio between the total number of physics-selected MB events and the ones receiving a trigger input from the unlike-sign dimuon condition, i.e.

$$F_{\text{norm}}^{\text{offline 1}} = \frac{N_{\text{MB}}}{N_{\text{MB\&0MUL}}}. \tag{3.5}$$

As the probability to fire simultaneously these two triggers is low, we can insert an intermediate trigger with a higher trigger rate such that

$$F_{\text{norm}}^{\text{offline 2}} = \frac{N_{\text{MB}}}{N_{\text{MB\&0MSL}}} \times \frac{N_{\text{CMSL}}}{N_{\text{CMSL\&0MUL}}}. \tag{3.6}$$

The label MB&0MSL denotes the sample of minimum bias events containing an input from the single muon low-p_{T} trigger. The CMSL&0MUL label follows a similar explanation. This *indirect* calculation benefits from a greater number of MSL inputs in MB events with respect to MUL inputs, thus providing a smaller statistical uncertainty.

The two offline methods use CINT7 as minimum bias trigger. This class corresponds to the coincidence of the signals from the V0 detectors mentioned in Section 2.2.1. For the 2018 Pb–Pb data, it is replaced by the CINT7ZAC trigger, i.e. the combination of CINT7 and 1ZAC triggers. The latter input originates from the ZDC calorimeters enabling the rejection of the electromagnetic contributions.

Online method

The last method exploits the lowest level of trigger input information prior to any event selection. The normalisation factor reads

$$F_{\text{norm}}^{\text{online}} = \frac{L0_{\text{ref}} \times \mathcal{P}_{\text{ref}}}{L0_{\text{CMUL}} \times \mathcal{P}_{\text{CMUL}}}, \tag{3.7}$$

where $L0_{\text{ref}}$ is the number of counters recorded for a reference interaction trigger. The purity factor $\mathcal{P}$ represents the fraction of events after the offline physics selection for a given trigger class.

In proton–proton collisions, the minimum bias trigger is provided by the V0 system. For the Pb–Pb data, the purity factors are restricted to the 0–90% most central events to cope with the analysis. Therefore, the C0V0M class based on V0 outputs is used as minimum bias trigger in the Pb–Pb case.

Pile-up correction

The normalisation factor must account for pile-up events, when more than one collision occur within the time window of a single bunch crossing. Each calculation of F_{norm} introduced before is multiplied by a so-called pile-up factor

$$PU = \frac{\mu}{1 - \exp(-\mu)} \text{ with } \mu = -\ln\left(1 - \frac{\mathcal{P}_{\text{MB}} \times L0_{\text{rate MB}}}{N_{\text{colliding}} \times f_{\text{LHC}}}\right). \tag{3.8}$$

The term $\mathcal{P}_{\text{MB}}$ is the purity factor for the MB trigger considered in the method, $L0_{\text{rate MB}}$ the number of MB counters at the level 0 per unit of data-taking time. The quantity

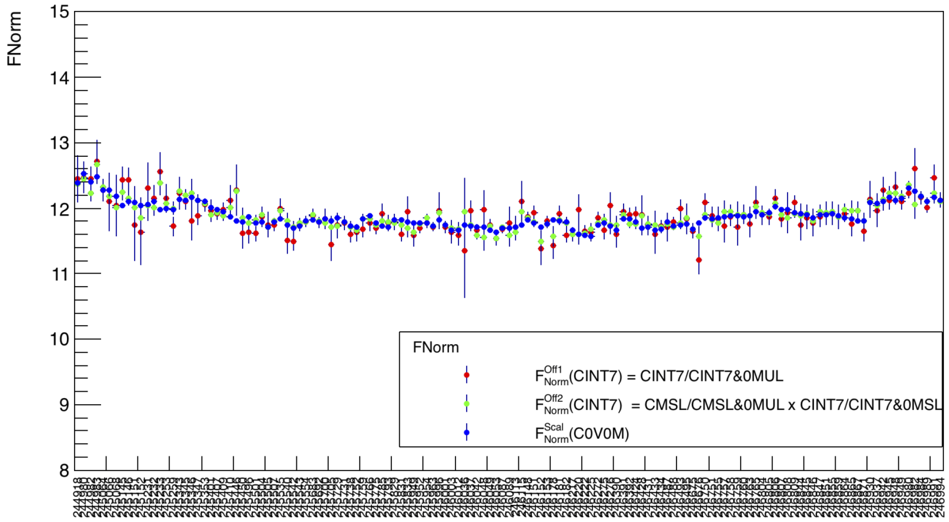

Figure 3.18: Normalisation factor as a function of the run number in the LHC15o period, for the calculation methods labelled in the legend. The vertical error bars represent the statistical uncertainties. Figure taken from the thesis [65].

$N_{\text{colliding}}$ corresponds to the number of colliding bunches per run and $f_{\text{LHC}} = 11245$ Hz, the revolution frequency of the LHC. For the 2017 proton–proton data taking at $\sqrt{s} = 5.02$ TeV, the pile-up correction ranges from 1 during LHC17p to 1.02 for the runs at high interaction rate of the LHC17q period. This factor is inferior to 1.005 for Pb–Pb collisions.

Results

The normalisation factors are computed on a run-by-run basis. Figure 3.18 shows the evolution of F_{norm} for the LHC15o period. The results obtained with the different methods are compatible with each other. The overall results are reported in Table 3.15. For the final result, we take the online method for the central value as it gives the best statistical precision, and we compute the weighted average like

$$F_{\text{norm}} = \frac{\sum\limits_{\text{run } i} F_{\text{norm}}^{\text{online, } i} \times N^{i}_{\text{CMUL\&PS}}}{\sum\limits_{\text{run } i} N^{i}_{\text{CMUL\&PS}}}. \tag{3.9}$$

The associated systematic uncertainty is the maximum difference of F_{norm} between the online and the offline methods. The statistical uncertainty is negligible with respect to the systematic one. For "Run 2", we take the largest relative systematic uncertainty among the periods, i.e. 0.5%, as systematic uncertainty.

3.4.2 Luminosity of proton–proton collisions

The ultimate goal of the pp analysis is to determine the cross section for Υ production. Therefore, we must normalise the yields to the interaction rate delivered by the LHC, the luminosity. For the present data sample, the integrated luminosity is evaluated as

Period	$F_{\text{norm}} \pm$ syst
LHC17p	1486.1
LHC17q	1317.3
LHC15o	11.88 ± 0.03 (0.3%)
LHC18q	13.55 ± 0.06 (0.5%)
LHC18r	13.65 ± 0.02 (0.1%)
Run 2	13.02 ± 0.05 (0.5%)

Table 3.15: Averaged normalisation factor per period. The uncertainty is negligible for pp data.

$$L_{\text{int}} = \frac{F_{\text{norm}} \times N_{\text{CMUL\&PS}}}{\sigma_{\text{vdM}}}, \tag{3.10}$$

where the numerator is identified as the equivalent number of minimum bias events, cf. equation 3.4, and the denominator represents the cross section of a reference MB trigger. The latter has been evaluated via a van der Meer (vdM) scan whose procedure is available in the note [67]. The method relies on the evolution of the interaction rate when translating the beams with respect to each other, during special filling schemes. For these periods, the reference process was measured by the T0 and V0 detectors. The cross section is $\sigma_{\text{vdM}}^{\text{T0}} = 20.82 \pm 0.01\ (\text{stat}) \pm 0.37\ (\text{syst})$ mb. The V0 measurement serves for the verification of the method. The corresponding integrated luminosity amounts to $L_{\text{int}} = 1230 \pm 22\ \text{nb}^{-1}$ with a systematic uncertainty originating from the propagation of the terms in the equation 3.10.

Chapter 4

Results and discussion

Here we are at the core of this thesis. The production of Υ mesons in proton–proton collisions is studied via the cross section. Not only does this observable serves as a *benchmark* to quantify the suppression in nucleus–nucleus collisions, but above all it makes it possible to constrain the state-of-the-art production models. For the Pb–Pb analysis, we report the yields as a function of p_{T} and rapidity, as well as the yield ratio between the Υ(2S) and Υ(1S) states as a function of collision centrality. We then determine the nuclear modification factors for several centrality classes and kinematic intervals. Results are compared to model calculations in order to interpret our data and presented together with other measurements performed at the LHC when possible.

Through this chapter, the results are reported with two types of uncertainty. The first value refers to the statistical uncertainty from the signal extraction while the second component is a systematic uncertainty. In the figures, the measurements are represented with vertical error bars for the statistical uncertainties and with boxes for the uncorrelated systematic uncertainties. We will always adopt this convention unless otherwise stated.

4.1 Cross section in proton–proton collisions

Let us begin with the results in proton–proton collisions. We define the cross section of the production of Υ states as the number of resonances measured in a kinematic interval, normalised to the total luminosity recorded. In this section, we examine the production cross section within the forward acceptance of the ALICE muon spectrometer.

4.1.1 Direct measurement

This measurement represents the first *direct* determination of the Υ production cross section in proton–proton collisions at $\sqrt{s} = 5.02$ TeV, in the forward region. The rapidity and p_{T}-differential cross sections are obtained as

$$\frac{\mathrm{d}\sigma_{\Upsilon}}{\mathrm{d}y} = \frac{N_{\Upsilon\to\mu^+\mu^-}}{(A\times\varepsilon)_{\Upsilon}\cdot BR(\Upsilon\to\mu^+\mu^-)\cdot L_{\mathrm{int}}\cdot\Delta y} \tag{4.1}$$

and

$$\frac{\mathrm{d}^2\sigma_{\Upsilon}}{\mathrm{d}y\mathrm{d}p_{\mathrm{T}}} = \frac{N_{\Upsilon\to\mu^+\mu^-}}{(A\times\varepsilon)_{\Upsilon}\cdot BR(\Upsilon\to\mu^+\mu^-)\cdot L_{\mathrm{int}}\cdot\Delta y\Delta p_{\mathrm{T}}}, \tag{4.2}$$

respectively, where

- $N_{\Upsilon\rightarrow\mu^+\mu^-}$ denotes the number of reconstructed Υ mesons within a given rapidity and p_{T} interval, extracted via the procedure described in Section 3.2.2.
- $(A\times\varepsilon)_{\Upsilon}$ represents the correction for the acceptance and reconstruction efficiency of the decay muons estimated in Section 3.3.
- $BR(\Upsilon\rightarrow\mu^+\mu^-)$ is the dimuon branching fraction, i.e. the probability for a given resonance to decay into an opposite-sign muon pair. The values, tabulated by the Particle Data Group [1], are $(2.48\pm0.05)\%$ for Υ(1S), $(1.93\pm0.17)\%$ for Υ(2S), and $(2.18\pm0.21)\%$ for Υ(3S).
- $L_{\mathrm{int}} = 1230\pm22\ \mathrm{nb}^{-1}$ corresponds to the integrated luminosity of the analysed data sample, cf. Section 3.4.2.
- Δy and Δp_{T} are the widths of the rapidity and transverse momentum intervals, respectively.

The Υ(nS)-to-Υ(1S) cross-section ratios simply read

$$\frac{\sigma_{\Upsilon(\mathrm{nS})}}{\sigma_{\Upsilon(\mathrm{1S})}} = \frac{N_{\Upsilon(\mathrm{nS})\rightarrow\mu^+\mu^-}}{N_{\Upsilon(\mathrm{1S})\rightarrow\mu^+\mu^-}} \times \frac{(A\times\varepsilon)_{\Upsilon(\mathrm{1S})}}{(A\times\varepsilon)_{\Upsilon(\mathrm{nS})}} \times \frac{BR(\Upsilon(\mathrm{1S})\rightarrow\mu^+\mu^-)}{BR(\Upsilon(\mathrm{nS})\rightarrow\mu^+\mu^-)} \text{ with n} = 2, 3. \tag{4.3}$$

Before coming to the results, let us go over each source of systematic uncertainty involved in the computation of the cross section.

Summary of the systematic uncertainties

The number of Υ states is estimated from a fit to the unlike-sign dimuon invariant mass distribution. In Section 3.2.3, we have inspected the contribution of the fitting model components. The main source of uncertainty arises from the set of tail parameters of the CB2 signal shapes. The systematic uncertainty on the signal extraction procedure is evaluated from the combination of all possible fit tests. We assume that the results are not correlated with p_{T} or rapidity.

Each step of the $A\times\varepsilon$ calculation was studied along Section 3.3.3 by changing one by one the elements of the Monte Carlo simulations. The systematic uncertainties are then determined from the spread of the results. For the initial distributions, we account for the p_{T}-y correlations as well as for the statistical uncertainties of the measurement points used to generate the MC input shapes. The assessment of the tracking, trigger and matching efficiency uncertainties is based on the discrepancies between data and MC efficiencies at the muon track level. All the sources of uncertainties on $A\times\varepsilon$ are considered as uncorrelated as a function of p_{T} and rapidity.

The determination of the integrated luminosity relies on the inelastic cross section measured via the T0 and V0 detectors. The associated systematic uncertainty is the sum of many factors detailed in the note [67]. The luminosity and branching fraction uncertainties are fully correlated with p_{T} and rapidity.

All the sources of systematic uncertainties for the computation of the cross section are enumerated in Table 4.1. The total systematic uncertainty is the quadratic sum of the

Source of uncertainty	$\Upsilon(1S)$			$\Upsilon(2S)$	$\Upsilon(3S)$
	integrated	vs p_T	vs y	integrated	integrated
Signal extraction	6.5	6.1–7.0	6.2–7.6	7.8	19.1
MC input shapes	1.7	1.5–1.7	2.2–3.5	1.7	1.7
Tracking efficiency	2	2	2	2	2
Trigger efficiency	2	1.0–2.2	1.0–2.6	2	2
Matching efficiency	1	1	1	1	1
Luminosity	1.8	1.8*	1.8*	1.8	1.8

Table 4.1: Summary of the relative systematic uncertainties (in %) on Υ production cross sections in pp collisions at $\sqrt{s} = 5.02$ TeV. The ranges correspond to the minimum and maximum uncertainty as a function of the kinematic variable. Values marked with an asterisk denote the uncertainties correlated with p_T and rapidity.

values in a given column. In the evaluation of the Υ(nS)-to-Υ(1S) ratios, we assume that only the uncertainties of the signal extraction and the branching fraction do not cancel out. The Υ(nS) and Υ(1S) branching fraction uncertainties are summed in quadrature.

Integrated cross sections

The inclusive production cross sections of the Υ states in pp collisions at $\sqrt{s} = 5.02$ TeV, integrated over $2.5 < y < 4.0$ for $p_T < 15$ GeV/c, are

- $\sigma_{\Upsilon(1S)} = 45.5 \pm 3.9 \pm 3.5$ nb,
- $\sigma_{\Upsilon(2S)} = 22.4 \pm 3.2 \pm 2.7$ nb,
- $\sigma_{\Upsilon(3S)} = 4.9 \pm 2.2 \pm 1.0$ nb.

For the record, the first uncertainty corresponds to the statistical uncertainty whereas the second one is the quadratic sum of the systematic uncertainties discussed previously. The excited-to-ground state cross-section ratios amount to

- $\sigma_{\Upsilon(2S)}/\sigma_{\Upsilon(1S)} = 0.488 \pm 0.042 \pm 0.045$,
- $\sigma_{\Upsilon(3S)}/\sigma_{\Upsilon(1S)} = 0.105 \pm 0.048 \pm 0.015$.

With the end of Run 2, we can present these results with all the LHC measurements performed at forward rapidity at various centre-of-mass energies. To avoid redundancy, we display in Figure 4.1 the product of the branching fraction and the cross section, written as

$$BR(\Upsilon \to \mu^+\mu^-) \times \sigma_\Upsilon = \frac{N_{\Upsilon\to\mu^+\mu^-}}{(A \times \varepsilon)_\Upsilon \cdot L_{\text{int}}}. \tag{4.4}$$

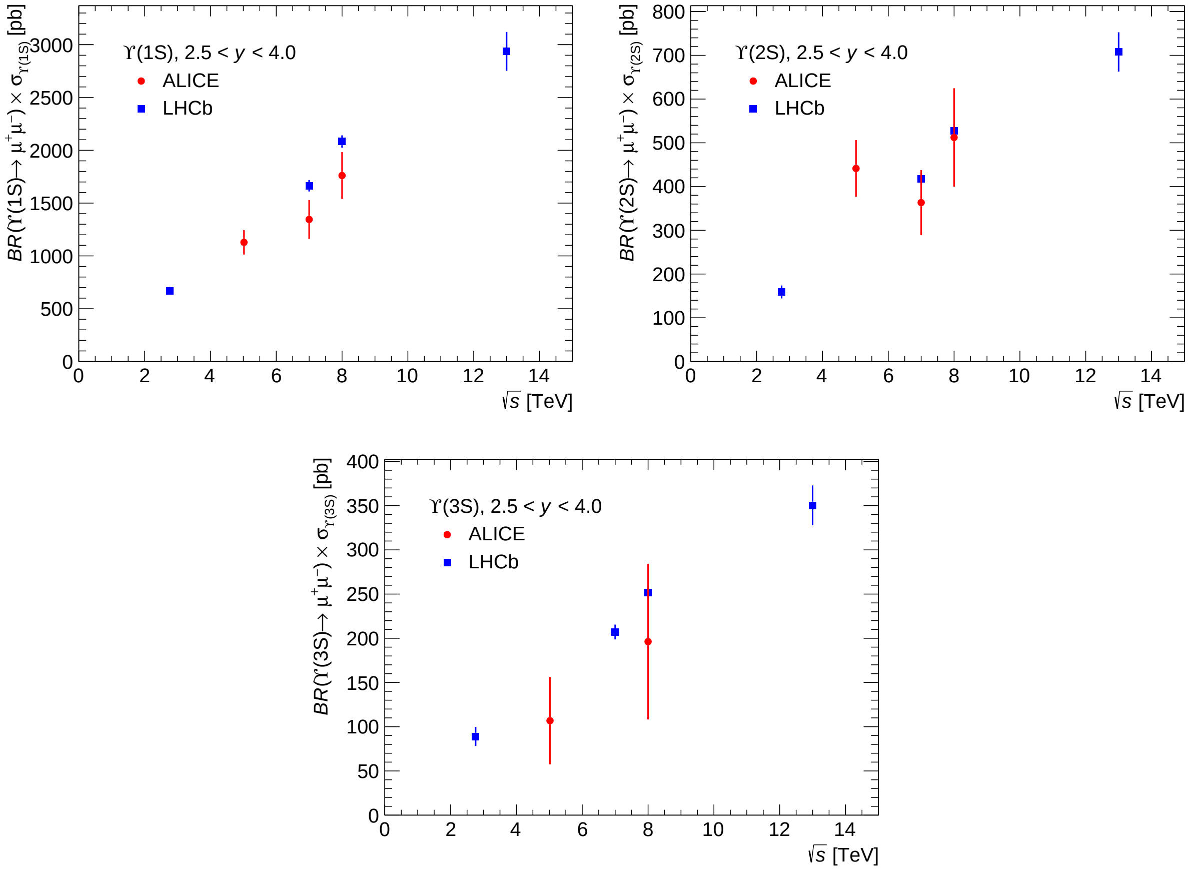

Figure 4.1: Product of the dimuon branching fraction and the cross section of (top-left) $\Upsilon(1S)$, (top-right) $\Upsilon(2S)$ and (bottom) $\Upsilon(3S)$ as a function of the centre-of-mass energy in proton–proton collisions, integrated in the $2.5 < y < 4.0$ interval. The vertical error bars represent the quadratic sum of the statistical and systematic uncertainties. Data points are from ALICE [68, 69] and LHCb [62, 70, 71] measurements. The LHCb points at 7 and 8 TeV correspond to the sum of rapidity-differential cross sections for $p_T < 30$ GeV/c.

LHCb data are taken as the sum of rapidity-differential cross sections within $2.5 < y < 4.0$ to match the acceptance of the ALICE muon spectrometer. At the TeV scale, the cross sections increase linearly with the centre-of-mass energy. The result for $\Upsilon(2S)$ stands like an outlier, albeit with large uncertainties.

Rapidity and p_T-differential cross sections

Given the statistical significance, we can only measure the production of $\Upsilon(1S)$ in two rapidity intervals and in four p_T ranges. The results are reported in Table 4.2 and shown in Figure 4.2.

The rapidity-differential cross sections are shown together with the CMS measurements at midrapidity [72]. Thanks to the complementarity of the acceptances, we can observe the rapidity dependence of Υ production from $y = 0$ up to 4. These experimental results are compared with two calculations derived from the colour-evaporation model (CEM). While the improved version of the model (ICEM) is a leading-order calculation [73], the other approach computes the hadroproduction at next-to-leading order (CEM NLO)

Rapidity interval	$\frac{\mathrm{d}\sigma_{\Upsilon(1\mathrm{S})}}{\mathrm{d}y}$ [nb]	p_{T} range [GeV/c]	$\frac{\mathrm{d}^2\sigma_{\Upsilon(1\mathrm{S})}}{\mathrm{d}y\mathrm{d}p_{\mathrm{T}}}$ [nb/(GeV/c)]
$2.5 < y < 3.25$	$44.6 \pm 4.4 \pm 3.4$	$0 < p_{\mathrm{T}} < 2$	$2.12 \pm 0.49 \pm 0.18$
$3.25 < y < 4.0$	$15.5 \pm 2.6 \pm 1.3$	$2 < p_{\mathrm{T}} < 4$	$5.35 \pm 0.76 \pm 0.41$
		$4 < p_{\mathrm{T}} < 6$	$4.54 \pm 0.65 \pm 0.32$
$2.5 < y < 4.0$	$30.3 \pm 2.3 \pm 3.5$	$6 < p_{\mathrm{T}} < 15$	$0.71 \pm 0.12 \pm 0.05$

Table 4.2: Rapidity and p_{T}-differential cross section of $\Upsilon(1\mathrm{S})$ production in proton–proton collisions at $\sqrt{s} = 5.02$ TeV.

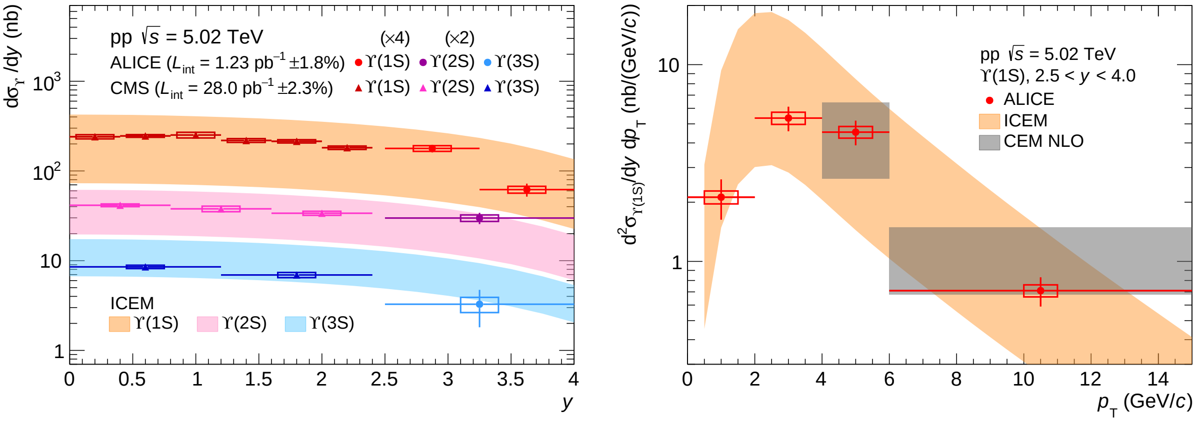

Figure 4.2: (left) rapidity-differential cross section of $\Upsilon(1\mathrm{S})$, $\Upsilon(2\mathrm{S})$ and $\Upsilon(3\mathrm{S})$ production, and (right) p_{T}-differential cross section of $\Upsilon(1\mathrm{S})$ production in proton–proton collisions at $\sqrt{s} = 5.02$ TeV. The global uncertainties on the luminosities and on the branching fractions are not represented. The results are compared with calculations described in the text. The $\Upsilon(1\mathrm{S})$ and $\Upsilon(2\mathrm{S})$ rapidity-differential cross sections are multiplied by a factor to improve the readability. The CMS measurements are available at this link.

up to α_{S}^5 [74]. Both calculations account for the feed-down contributions from heavier bottomonium decays.

The two calculations are represented in Figure 4.2 with bands arising from the propagation of uncertainties on the factorisation and renormalisation scales. They describe the measured $\Upsilon(1\mathrm{S})$ p_{T}-spectrum within large uncertainties. The results indicate that the forward ALICE acceptance covers the rapidity region where the production drops from the midrapidity plateau spanned by the CMS experiment. This observation is in line with the ICEM expectations. The measured $\Upsilon(2\mathrm{S})$ cross sections lie on the higher limit of the model whereas the $\Upsilon(3\mathrm{S})$ one on its lower limit.

4.1.2 Interpolated cross sections

The nuclear modification factor quantifies the production yield in nucleus–nucleus with respect to proton–proton collisions. That is why we often mention the pp cross section as a *reference* observable. A relatively small uncertainty is essential if we aim to investigate the suppression features. The statistical uncertainties of the direct measurement are of the order of the ones in the Pb–Pb analysis and thus limit the potential of the R_{AA} study. Moreover, the Υ production could only be measured in a few differential intervals.

The reference cross sections are thus determined via an interpolation procedure based on various measurements performed at the LHC. We save the discussion of the procedures for Appendix B and only report the final results here. From now on, we refer to the product of the dimuon branching fraction with the cross section, noted $\sigma_{\Upsilon\to\mu^+\mu^-}$ and expressed in picobarns.

Rapidity-differential cross sections

The rapidity-differential cross sections in $2.5 < y < 4.0$, integrated over $p_{\mathrm{T}} < 15$ GeV/c, are estimated in Appendix B.1.2. The results can be found in Table 4.3. The reference cross section for Υ(3S) is 99.4 ± 4.7 pb. The cross-section ratio between the Υ(2S) and Υ(1S) states, not corrected for the branching fractions, amounts to 0.243 ± 0.003. The results as a function of rapidity, evaluated in Appendix B.2, are also reported in Table 4.3 and displayed in the left panel of Figure 4.3.

Rapidity interval	$\frac{\mathrm{d}\sigma_{\Upsilon(1\mathrm{S})\to\mu^+\mu^-}}{\mathrm{d}y}$ [pb]	Rapidity interval	$\frac{\mathrm{d}\sigma_{\Upsilon(2\mathrm{S})\to\mu^+\mu^-}}{\mathrm{d}y}$ [pb]
$2.5 < y < 4.0$	801.2 ± 42.3	$2.5 < y < 4.0$	201.5 ± 15.2
$2.5 < y < 2.8$	1032.7 ± 50.7	$2.5 < y < 3.3$	241.0 ± 19.5
$2.8 < y < 3.1$	908.9 ± 59.7		
$3.1 < y < 3.3$	796.4 ± 66.6		
$3.3 < y < 3.6$	678.8 ± 70.7	$3.3 < y < 4.0$	146.9 ± 21.2
$3.6 < y < 4.0$	512.7 ± 73.2		

Table 4.3: Interpolated rapidity-differential cross sections of Υ(1S) and Υ(2S) production at $\sqrt{s} = 5.02$ TeV. The results are for $p_{\mathrm{T}} < 15$ GeV/c.

p_{T}-differential cross sections

In Appendix B.1.4, we interpolate the double-differential cross section of Υ production in the p_{T} intervals matching the Pb–Pb analysis. The results are given in Table 4.4 and shown in the right panel of Figure 4.3.

4.2 Production in Pb–Pb collisions

We now turn to the results of the Pb–Pb data analysis. Similar to the differential cross sections in proton–proton collisions, the yields normalised by the average nuclear overlap function are presented together with the CMS measurements. The ratio of production yields between the Υ(2S) and Υ(1S) states is compared with calculations as a function of the centrality.

p_{T} range [GeV/c]	$\frac{\mathrm{d}^2\sigma_{\Upsilon(1\mathrm{S})\to\mu^+\mu^-}}{\mathrm{d}y\mathrm{d}p_{\mathrm{T}}}$ [pb/(GeV/c)]	p_{T} range [GeV/c]	$\frac{\mathrm{d}^2\sigma_{\Upsilon(2\mathrm{S})\to\mu^+\mu^-}}{\mathrm{d}y\mathrm{d}p_{\mathrm{T}}}$ [pb/(GeV/c)]
$0 < p_{\mathrm{T}} < 2$	74.0 ± 4.7	$0 < p_{\mathrm{T}} < 4$	21.5 ± 1.7
$2 < p_{\mathrm{T}} < 4$	121.9 ± 7.7		
$4 < p_{\mathrm{T}} < 6$	97.4 ± 5.6		
$6 < p_{\mathrm{T}} < 9$	49.1 ± 4.3	$4 < p_{\mathrm{T}} < 15$	9.73 ± 0.73
$9 < p_{\mathrm{T}} < 15$	12.5 ± 2.0		

Table 4.4: Interpolated double-differential cross section of Υ(1S) and Υ(2S) production as a function of p_{T} at $\sqrt{s} = 5.02$ TeV, within the $2.5 < y < 4.0$ interval.

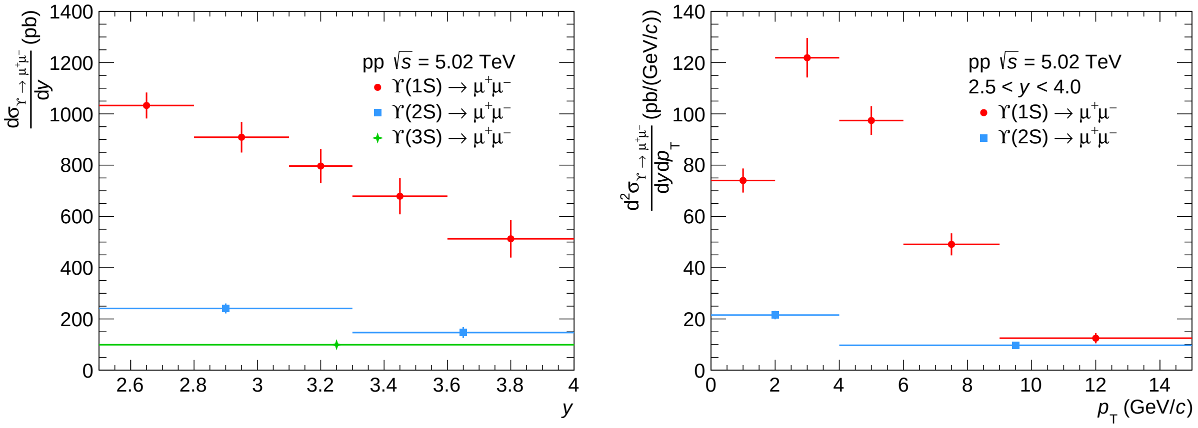

Figure 4.3: Interpolated (left) y-differential cross sections, and (right) p_{T}-differential cross sections in proton–proton collisions at $\sqrt{s} = 5.02$ TeV.

4.2.1 Definition of observables

The yields, corrected for acceptance and efficiencies, are normalised to the number of equivalent minimum bias events in the data sample analysed. In view of the determination of the nuclear modification factors, we do not correct for the dimuon branching fraction. The rapidity and p_{T}-differential yields for the 0–90% centrality class thus read

$$\frac{\mathrm{d}^2 Y_{\Upsilon\to\mu^+\mu^-}}{\mathrm{d}y\mathrm{d}p_{\mathrm{T}}} = \frac{N_{\Upsilon\to\mu^+\mu^-}}{(A\times\varepsilon)_{\Upsilon}\cdot N_{\text{equi MB}}\cdot\Delta y\Delta p_{\mathrm{T}}} \tag{4.5}$$

where

- $N_{\Upsilon\to\mu^+\mu^-}$ is the number of Υ mesons extracted within a given centrality, rapidity and p_{T} interval in Section 3.2.2.
- $(A\times\varepsilon)_{\Upsilon}$ represents the acceptance and efficiency correction evaluated from the embedding MC simulation in Section 3.3.
- After physics selection of the CMUL triggered events within the 0–90% centrality interval, we find approximately 5.2 billion equivalent MB events over the full Run 2

data. For a total Pb–Pb interaction cross section $\sigma_{\text{Pb–Pb}} = 7.67 \pm 0.16$ b [45], that corresponds to an integrated luminosity $L_{\text{int}} = \frac{N^{0\text{–}90\%}_{\text{equi MB}}}{0.9} \frac{1}{\sigma_{\text{Pb–Pb}}} = 757 \pm 16\ \mu\text{b}^{-1}$.

- Δy and Δp_{T} are the widths of the rapidity and transverse momentum intervals, respectively.

If we aim to compare the results with other measurements, we must pay attention to different centrality ranges between experiments. The yields are further divided by the nuclear overlap function T_{AA} averaged over a given centrality interval. The resulting observable can be interpreted as an *effective cross section* of the production in binary nucleon–nucleon collisions.

We define the yield ratio between the $\Upsilon(2\text{S})$ and $\Upsilon(1\text{S})$ states as

$$\frac{N_{\Upsilon(2\text{S})}}{N_{\Upsilon(1\text{S})}} = \frac{N_{\Upsilon(2\text{S})\to\mu^+\mu^-}}{N_{\Upsilon(1\text{S})\to\mu^+\mu^-}} \times \frac{(A\times\varepsilon)_{\Upsilon(1\text{S})}}{(A\times\varepsilon)_{\Upsilon(2\text{S})}} \times \frac{BR(\Upsilon(1\text{S})\to\mu^+\mu^-)}{BR(\Upsilon(2\text{S})\to\mu^+\mu^-)}. \tag{4.6}$$

For this observable, the yields are corrected for the branching fractions for comparison with theoretical calculations.

4.2.2 Summary of the systematic uncertainties

The evaluation of the yields and of the nuclear modification factors involve many sources of systematic uncertainties. We will review them all and give their degree of correlation with the centrality, transverse momentum and rapidity.

Signal extraction

The systematic uncertainties related to the signal extraction procedure are estimated from the distribution of the fit results in Section 3.2.4. In the Pb–Pb analysis, they are mainly caused by differences in the background description between the direct fit and the application of the event-mixing technique. At maximum, the relative uncertainty varies from 3.6% to 10% for $\Upsilon(1\text{S})$, and from 9.7% to 39% for $\Upsilon(2\text{S})$ as a function of rapidity. The signal extraction is the dominant source of systematic uncertainty for the excited states, with a partial correlation to the statistical uncertainties. The systematic uncertainties are slightly reduced when considering the yield ratio between two states. These uncertainties are considered as uncorrelated to any kinematic variable and centrality.

$A \times \varepsilon$ correction

To generate the Υ signals, the initial p_{T} and rapidity distributions are modified or not with nPDF parametrisations. The associated systematic uncertainty is evaluated as the maximum relative difference between the $A \times \varepsilon$ values obtained when switching the input shapes of the Monte Carlo simulations. For the tracking, trigger and matching efficiencies, we have studied the discrepancies with respect to the data and propagated the results from single muon tracks to Υ mesons. The dimuon reconstruction efficiency is the main source of systematic uncertainty for the $A \times \varepsilon$ corrections.

These contributions are uncorrelated with p_{T} and rapidity, and fully correlated with the centrality. In addition, the tracking systematic uncertainty contains an uncorrelated component as a function of the centrality. It is negligible in the peripheral collisions and increases up to 1% for the most central events. We assume that these uncertainties are identical for all Υ states and thus cancel out in the computation of ratios between excited and ground states.

Centrality determination

The centrality classes are defined with respect to a reference point estimated with a 0.5% accuracy. This uncertainty can affect the number of Υ mesons measured per interval by shifting the boundaries of the centrality classes. To propagate this effect, we could extract the raw yields using different centrality estimators and determine an uncertainty based on the variation of the results. However, the statistical fluctuations are too large to make a sensible estimate with the present measurement. As the variation and the overall magnitude are found to be similar for J/ψ, we take the values obtained in the analysis [65] wherein the statistical uncertainties are much smaller. This extraction relies on the assumption that the shape of the centrality dependence of the dimuon invariant mass spectrum is similar for both quarkonia.

The systematic uncertainty is about 0.2% from the most central intervals to the 40–50% centrality class, and increases up to 5.5% for the most peripheral interval. This uncertainty is negligible for the measurements integrated over the whole 0–90% interval. Hence we will only consider this uncertainty for the centrality dependence of the nuclear modification factor.

Other sources

The number of minimum bias events is derived from the calculation of the normalisation factor in Section 3.4.1. The associated uncertainty is the maximum difference of $F_{\rm norm}$ obtained via the three methods. The systematic uncertainty on the normalisation factor is 0.5% over Run 2 and is correlated with all kinematic variables.

Nuclear overlap functions have been reported in Table 3.1 with their corresponding systematic uncertainties. The latter vary with the centrality and are fully correlated with $p_{\rm T}$ and rapidity.

For the reference cross sections, we assume that the uncertainties are uncorrelated with $p_{\rm T}$ and rapidity. These uncertainties will be added in quadrature to the other systematic uncertainties of the nuclear modification factors. They are the main contributors of the global uncertainty for the $R_{\rm AA}$ as a function of the centrality.

Summary

All the sources of systematic uncertainties entering in the computation of yields nuclear modification factors for Υ(1S) and Υ(2S) are summarised in Tables 4.5 and 4.6 respectively. The total systematic uncertainty is the quadratic sum of the values in a given column. Values marked with an asterisk denote the uncertainties correlated with the variable. The ranges indicate the minimum and the maximum uncertainty as a function of the kinematic variable. The symbol "$\oplus$" denotes the quadratic sum of a correlated and an uncorrelated component.

Table 4.5: Summary of the relative systematic uncertainties (in %) on the yield and $R_{\rm AA}$ of Υ(1S), integrated over the 0–90% centrality class as well as a function of centrality, $p_{\rm T}$ and rapidity.

Source of uncertainty	integrated	vs centrality	vs $p_{\rm T}$	vs rapidity
Signal extraction	4.4	3.9–7.4	3.6–9.1	3.6–10.2
MC input shapes	0.4	0.4*	0.1–0.6	0.2–0.4
Tracking efficiency	3	3* $\oplus$ (0–1)	3 $\oplus$ 1*	3 $\oplus$ 1*
Trigger efficiency	3	3*	0.5–2.6	1.5–4.0
Matching efficiency	1	1*	1	1
Normalisation factor	0.5	0.5*	0.5*	0.5*
Nuclear overlap function	1	0.7–2.4	1*	1*
Centrality determination	-	0.1–5.5	-	-
Reference cross section	5.3	5.3*	5.7–15.8	4.9–14.3

The systematic uncertainties for the ratios between the Υ(2S) and the Υ(1S) states can be found in Table 4.7. As for the cross-section ratios in pp collisions, the uncertainties from the signal extraction and from branching fractions do not cancel. The table also reports the most important sources of systematic uncertainty for Υ(3S).

4.2.3 Effective cross sections

The production yields in Pb–Pb collisions at $\sqrt{s_{\rm NN}} = 5.02$ TeV, divided by $\langle T_{\rm AA}\rangle$ for the 0–90% centrality interval and integrated over $2.5 < y < 4.0$ for $p_{\rm T} < 15$ GeV/c, are

- $Y_{\Upsilon(1S)\to\mu^+\mu^-}/\langle T_{\rm AA}\rangle = 424.4 \pm 14.0\ (\ 3.3\%) \pm 26.8\ (\ 6.3\%)$ pb,
- $Y_{\Upsilon(2S)\to\mu^+\mu^-}/\langle T_{\rm AA}\rangle = 38.5 \pm 7.2\ (18.8\%) \pm 7.3\ (18.9\%)$ pb,
- $Y_{\Upsilon(3S)\to\mu^+\mu^-}/\langle T_{\rm AA}\rangle = 1.6 \pm 7.4 \pm 1.7$ pb,

with $\langle T_{\rm AA}\rangle = 6.28 \pm 0.06$ mb^{-1} for the 0–90% centrality class, cf. Table 3.1. For the latter resonance, we can propagate the upper limit on the number of candidates estimated in Section 3.2.5 with the systematic uncertainties of the $A\times\varepsilon$ correction, of the normalisation factor and of the nuclear overlap function. Consequently, the effective cross section of Υ(3S) production is below 17.1 pb at a 95% confidence level.

For the rest of this part, the global uncertainties are not included in the quoted results, unless otherwise specified, nor represented in the figures.

Rapidity and $p_{\rm T}$-differential measurements

The luminosity accumulated over Run 2 enables to perform a detailed measurement of the Υ(1S) production as a function of rapidity and $p_{\rm T}$, as well as the first differential measurement of the Υ(2S) state in the forward rapidity region in heavy-ion collisions.

Table 4.6: Summary of the relative systematic uncertainties (in %) on the yield and R_{AA} of Υ(2S), integrated over the 0–90% centrality class as well as a function of centrality, p_{T} and rapidity.

Source of uncertainty	integrated	vs centrality	vs p_{T}	vs rapidity
Signal extraction	18.4	14.0–23.4	8.5–25.8	9.7–39.0
MC input shapes	0.3	0.3*	0.2–0.3	0.7
Tracking efficiency	3	3* $\oplus$ (0–1)	3 $\oplus$ 1*	3 $\oplus$ 1*
Trigger efficiency	3	3*	1.1–2.0	1.4–3.7
Matching efficiency	1	1*	1	1
Normalisation factor	0.5	0.5*	0.5*	0.5*
Nuclear overlap function	1	0.8–2.6	1*	1*
Centrality determination	-	0.1–0.3	-	-
Reference cross section	7.5	7.5*	7.5–7.7	8.1–14.4

Table 4.7: Summary of the relative systematic uncertainties (in %) on the Υ(2S)-to-Υ(1S) yield ratios as a function of centrality as well as on the yield and R_{AA} of Υ(3S).

Source of	Υ(2S)/Υ(1S)		Υ(3S)
uncertainty	integrated	vs centrality	integrated
Signal extraction	15.2	10.9–20.4	118
Reference cross section	1.2	1.2*	4.7

The effective rapidity and p_{T}-differential cross sections of the Υ(1S) production for the 0–90% centrality class are reported in Tables 4.8 and 4.9, respectively. The measurements for Υ(2S) in rapidity and p_{T} intervals can be found in Tables 4.10 and 4.11 respectively. The total systematic uncertainty correlated with the centrality amounts to 1.5% from the normalisation factor, the averaged nuclear overlap function, and the correlated component of the tracking efficiency uncertainty.

Rapidity interval	$\frac{1}{\langle T_{\mathrm{AA}}\rangle}\frac{\mathrm{d}Y_{\Upsilon(1\mathrm{S})\to\mu^+\mu^-}}{\mathrm{d}y}$ [pb]
$2.5 < y < 2.8$	447.3 ± 44.3 (9.9%) ± 51.0 (11.4%)
$2.8 < y < 3.1$	359.8 ± 20.9 (5.8%) ± 21.4 (5.9%)
$3.1 < y < 3.3$	316.7 ± 23.1 (7.3%) ± 18.9 (6.0%)
$3.3 < y < 3.6$	229.1 ± 14.2 (6.2%) ± 13.4 (5.9%)
$3.6 < y < 4.0$	156.3 ± 16.3 (10.4%) ± 10.1 (6.4%)

Table 4.8: Rapidity-differential cross section of the Υ(1S) production within the 0–90% centrality interval in Pb–Pb collisions at $\sqrt{s_{\mathrm{NN}}} = 5.02$ TeV.

p_{T} range	$\frac{1}{\langle T_{\mathrm{AA}}\rangle}\frac{\mathrm{d}^2Y_{\Upsilon(1\mathrm{S})\to\mu^+\mu^-}}{\mathrm{d}y\mathrm{d}p_{\mathrm{T}}}$ [pb/(GeV/c)]
$0 < p_{\mathrm{T}} < 2$ GeV/c	25.5 ± 2.3 (9.0%) ± 2.4 (9.5%)
$2 < p_{\mathrm{T}} < 4$ GeV/c	47.1 ± 2.7 (5.7%) ± 3.1 (6.5%)
$4 < p_{\mathrm{T}} < 6$ GeV/c	33.6 ± 2.1 (6.2%) ± 1.7 (4.9%)
$6 < p_{\mathrm{T}} < 9$ GeV/c	14.6 ± 1.3 (9.0%) ± 1.4 (9.7%)
$9 < p_{\mathrm{T}} < 15$ GeV/c	4.6 ± 0.5 (12.0%) ± 0.4 (7.8%)

Table 4.9: p_{T}-differential measurement of the Υ(1S) production within the $2.5 < y < 4.0$ and 0–90% centrality intervals in Pb–Pb collisions at $\sqrt{s_{\mathrm{NN}}} = 5.02$ TeV.

Rapidity interval	$\frac{1}{\langle T_{\mathrm{AA}}\rangle}\frac{\mathrm{d}Y_{\Upsilon(2\mathrm{S})\to\mu^+\mu^-}}{\mathrm{d}y}$ [pb]
$2.5 < y < 3.3$	19.5 ± 7.2 (37.1%) ± 7.7 (39.3%)
$3.3 < y < 4.0$	28.9 ± 5.8 (20.1%) ± 3.0 (10.4%)

Table 4.10: Rapidity-differential cross section of the Υ(2S) production within the 0–90% centrality interval in Pb–Pb collisions at $\sqrt{s_{\mathrm{NN}}} = 5.02$ TeV.

The results are presented in Figure 4.4 with the CMS measurements integrated over the 0–100% centrality interval [72]. This larger range motivates the normalisation of the yields to the nuclear overlap function: with $\langle T_{\mathrm{AA}}\rangle^{\mathrm{CMS}}_{0\text{–}100\%} = 5.61 \pm 0.17$ mb^{-1}, the relative difference between the averaged functions is about 10% and hence the yields would be

p_{T} range	$\frac{1}{\langle T_{\mathrm{AA}}\rangle}\frac{\mathrm{d}^2 Y_{\Upsilon(2\mathrm{S})\to\mu^+\mu^-}}{\mathrm{d}y\mathrm{d}p_{\mathrm{T}}}$ [pb/(GeV/c)]
$0 < p_{\mathrm{T}} < 4$ GeV/c	2.61 ± 0.82 (31.4%) $\pm\, 0.68$ (26.1%)
$4 < p_{\mathrm{T}} < 15$ GeV/c	1.35 ± 0.35 (25.6%) $\pm\, 0.12$ (9.1%)

Table 4.11: p_{T}-differential measurement of the $\Upsilon(2\mathrm{S})$ production within the $2.5 < y < 4.0$ interval in Pb–Pb collisions at $\sqrt{s_{\mathrm{NN}}} = 5.02$ TeV.

shifted by the same amount. The spectra look similar to the ones of the cross sections in proton–proton collisions. The $\Upsilon(1\mathrm{S})$ production decreases from the approximate plateau reached at midrapidity towards the forward rapidity. For $\Upsilon(2\mathrm{S})$, the situation is less clear. Based on the rapidity dependencies of the interpolated cross sections in Figure 4.3, we could expect a trend similar to the one observed for the ground state. It seems to be the case from $y = 0$ to 3.3 but not beyond. The effective cross section measured in the most forward rapidity interval is compatible with all the other results within uncertainties. Therefore, we cannot conclude on any rapidity dependence for the production of $\Upsilon(2\mathrm{S})$ given the size of the current uncertainties.

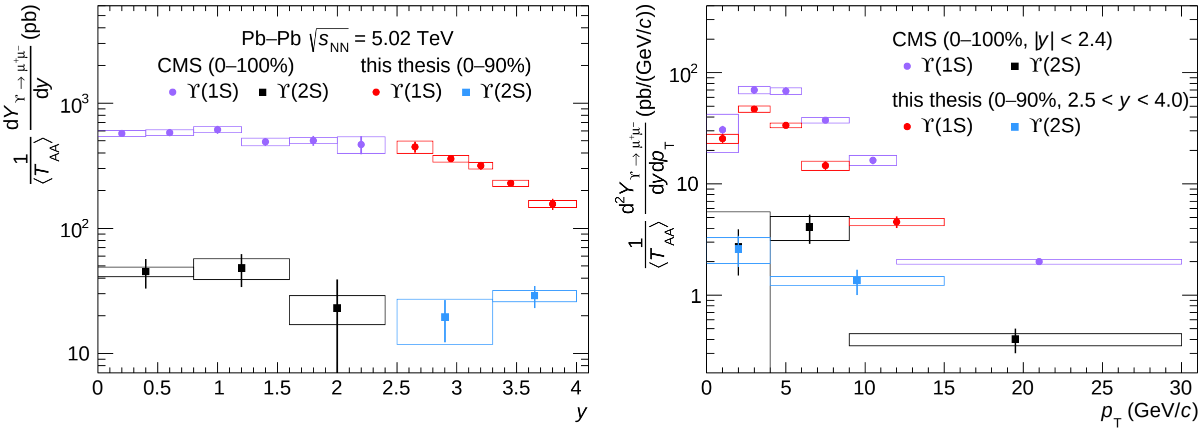

Figure 4.4: (left) rapidity and (right) p_{T}-differential yields of Υ production in Pb–Pb collisions at $\sqrt{s_{\mathrm{NN}}} = 5.02$ TeV. The yields are divided by the nuclear overlap function averaged over the total centrality range. The global uncertainties on the nuclear overlap function and on the number of MB events, not represented in the figures, amount to 1.5% for the ALICE results and 3.6% for the CMS measurement points (available at this link).

Regarding the p_{T} spectrum of $\Upsilon(1\mathrm{S})$ production, the measurement within the forward acceptance is slightly softer than at midrapidity: the average transverse momentum $\langle p_{\mathrm{T}}\rangle$ is found to be 4.0 ± 0.1 GeV/c, while $\langle p_{\mathrm{T}}\rangle_{\mathrm{CMS}} = 4.6 \pm 0.2$ GeV/c when summing the uncertainties in quadrature. The significance of this difference is 2.9σ.

$\Upsilon(2\mathrm{S})$-to-$\Upsilon(1\mathrm{S})$ yield ratio

In view of the investigation of the relative suppression between the two states, we evaluate the ratio of the $\Upsilon(1\mathrm{S})$ and $\Upsilon(2\mathrm{S})$ production yields based on the equation 4.6. The results are reported in Table 4.12. A global uncertainty of 9.6% from the branching fractions

Centrality class	$\langle N_{\text{part}} \rangle$	$N_{\Upsilon(2S)}/N_{\Upsilon(1S)}$ ± stat ± syst
0–30%	269.1	0.100 ± 0.025 (25.2%) ± 0.020 (20.4%)
0–90%	125.9	0.116 ± 0.022 (19.2%) ± 0.018 (15.2%)
30–90%	54.3	0.165 ± 0.042 (25.6%) ± 0.018 (10.9%)

Table 4.12: Yield ratio between the Υ(2S) and Υ(1S) states within centrality classes in Pb–Pb collisions. The systematic uncertainties do not include the global uncertainty from the branching fractions.

must be accounted for. The ratios measured for the 0–30% and 30–90% centrality classes are compatible with each other within the large statistical uncertainties.

These results can be compared with first predictions from the statistical hadronisation model [21] introduced in Section 1.1.3. This approach has been extended to the heavy-flavour sector by assuming that charm and bottom quarks could reach a kinetic equilibration through scattering with QGP's degrees of freedom. Historically, this *thermalisation scenario* led to the prediction for J/ψ regeneration before any experimental evidence [75]. The calculations require the charm and bottom production cross sections as input parameters, coming with relatively important uncertainties. That is why the Υ(2S)-to-Υ(1S) yield ratio is a good observable to test the applicability of the model for heavy-flavour production.

Our measurements are displayed as a function of $\langle N_{\text{part}} \rangle$ in Figure 4.5 with the results from the statistical hadronisation model. The latter come with two curves representing the uncertainty from the contribution of the corona formed by the nuclear overlap area. The predictions start from a value consistent with the ratio found in proton–proton collisions, slightly above 0.3, and drop rapidly to a plateau around 0.05 for central collisions. This steep dependence is due to the modification of the contribution from the corona as the impact parameter tends towards zero. It seems that the calculations underestimate the experimental result for the 0–30% most central collisions. Taking into account all the uncertainties, the tension between the data and the model is about one standard deviation. It would be interesting to compare this model with other measurements and observables, such as the p_{T} distribution of the absolute production yields.

4.3 Nuclear modification factors

Based on the results in the previous sections, we can already conclude that the production of Υ mesons in Pb–Pb collisions is significantly suppressed with respect to the one in proton–proton collisions. To quantify the magnitude of this suppression, we determine the nuclear modification factor

$$R_{\text{AA}}^{\Upsilon} = \frac{1}{\langle T_{\text{AA}} \rangle_i} \frac{\mathrm{d}^2 Y^i_{\Upsilon\to\mu^+\mu^-}/\mathrm{d}y\mathrm{d}p_{\text{T}}}{\mathrm{d}^2\sigma^{\text{pp}}_{\Upsilon\to\mu^+\mu^-}/\mathrm{d}y\mathrm{d}p_{\text{T}}}, \tag{4.7}$$

where

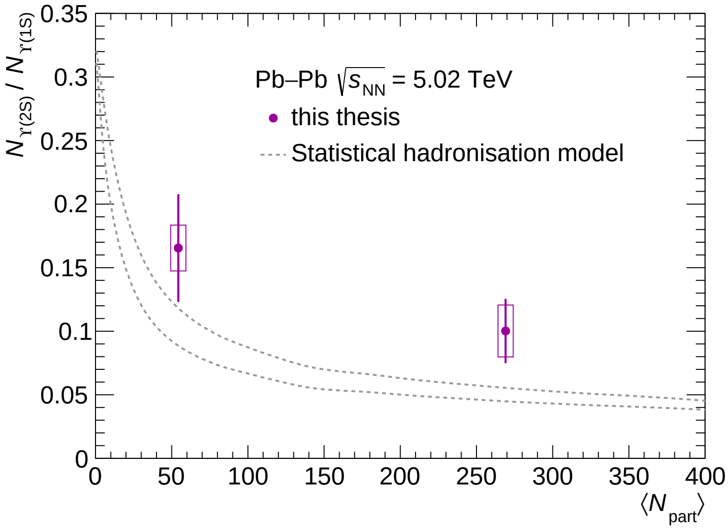

Figure 4.5: Ratio of the $\Upsilon(2S)$ and $\Upsilon(1S)$ yields corrected for branching fractions as a function of the average number of participants. The two dashed curves represent the values from the statistical hadronisation model [21]. The global uncertainties from the branching fractions are not represented.

- $\mathrm{d}^2 Y^i_{\Upsilon\to\mu^+\mu^-}/\mathrm{d}y\mathrm{d}p_{\mathrm{T}}$ is the production yield measured in Pb–Pb collisions for a given centrality class i and a rapidity and p_{T} interval, according to the equation 4.5;
- $\langle T_{\mathrm{AA}}\rangle_i$ represents the nuclear overlap function averaged over the centrality class i. The values considered for this analysis can be found in Table 3.1.
- $\mathrm{d}^2\sigma^{\mathrm{pp}}_{\Upsilon\to\mu^+\mu^-}/\mathrm{d}y\mathrm{d}p_{\mathrm{T}}$ corresponds to the production cross section in pp collisions in the same kinematic regime of the Pb–Pb measurement. For this term, we take the results from the Interpolated cross sections.

The systematic uncertainties entering in the computation of the nuclear modification factor are discussed in Section 4.2.2.

In addition, we evaluate the relative suppression between the $\Upsilon(2S)$ and $\Upsilon(1S)$ states via the *double ratio*, defined as

$$R_{\mathrm{AA}}^{\Upsilon(2S)/\Upsilon(1S)} = \left(\frac{N_{\Upsilon(2S)\to\mu^+\mu^-}}{N_{\Upsilon(1S)\to\mu^+\mu^-}}\right)_i \cdot \frac{(A\times\varepsilon)^i_{\Upsilon(1S)}}{(A\times\varepsilon)^i_{\Upsilon(2S)}} \Big/ \frac{\sigma^{\mathrm{pp}}_{\Upsilon(2S)\to\mu^+\mu^-}}{\sigma^{\mathrm{pp}}_{\Upsilon(1S)\to\mu^+\mu^-}}. \tag{4.8}$$

In the following, we report all the results before comparing them with other measurements in Section 4.3.2 and with model predictions in Section 4.3.3. We compute the deviation of the R_{AA} with respect to 1 in order to estimate how significant the suppression is. For the figures, the global uncertainties correlated with a kinematic variable are represented by a filled box at unity.

4.3.1 Results

The nuclear modification factors within the $2.5 < y < 4.0$ interval and $p_{\mathrm{T}} < 15$ GeV/c, centrality-integrated over the 0–90% class, are

- $R_{\mathrm{AA}}^{\Upsilon(1\mathrm{S})} = 0.353 \pm 0.012\ (\ 3.3\%) \pm 0.029\ (\ 8.2\%)$,
- $R_{\mathrm{AA}}^{\Upsilon(2\mathrm{S})} = 0.128 \pm 0.024\ (18.8\%) \pm 0.026\ (20.4\%)$,
- $R_{\mathrm{AA}}^{\Upsilon(3\mathrm{S})} = 0.010 \pm 0.049 \pm 0.012 < 0.117$ at a 95% confidence level.

Hence, the production of all resonances is significantly suppressed by about 20 standard deviations with respect to pp collisions: Υ(1S) by almost a factor three, Υ(2S) and Υ(3S) by about a factor eight. With a double ratio of 0.371 ± 0.071 (19.2%) $\pm\ 0.057$ (15.2%), the Υ(2S) state is much more strongly suppressed than the ground state by 7.2σ. The nuclear modification factor of the Υ(3S) is compatible with the result for Υ(2S) within less than two standard deviations. Therefore the production of the two excited states are at least similarly suppressed.

Centrality dependence

As the interaction mechanisms between quarkonia and the medium strengthen with the temperature / energy density, we first study the suppression as a function of the centrality of the Pb–Pb collisions. The nuclear modification factor of Υ(1S) can be determined for nine centrality classes reported in Table 4.13, but also for the two intervals considered for the Υ(2S) state. The production is suppressed for all classes except for the 70–90% centrality interval with the fewest Υ events. It is difficult to know whether this suppression varies significantly with the centrality because of the uncertainties. Only considering the signal extraction uncertainties, the difference between the values for the most peripheral and the most central intervals is 2.9σ. The standard deviation is even smaller when considering other intervals: 2.8σ between the 0–30% and 30–90% centrality classes for which the statistical uncertainties are the smallest, or 2.1σ between the 0–5% and 40–50% intervals. Consequently, we cannot confirm the centrality dependence for the suppression of Υ(1S) production from the present measurement.

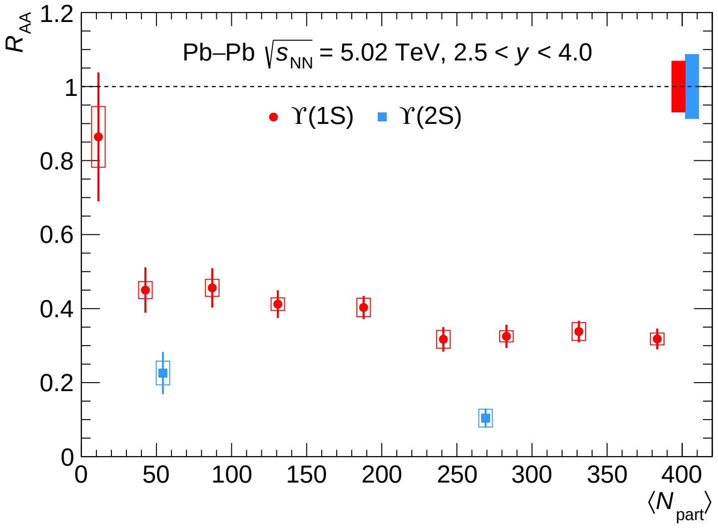

Figure 4.6: Nuclear modification factor of the Υ(1S) and Υ(2S) states as a function of the number of participants in Pb–Pb collisions at $\sqrt{s_{\mathrm{NN}}} = 5.02$ TeV.

Centrality class	$\langle N_{\text{part}} \rangle$	$R_{\text{AA}}^{\Upsilon(1\text{S})} \pm$ stat $\pm$ syst	std dev to 1
0–5%	383.4	0.318 ± 0.028 (8.7%) $\pm\, 0.016$ (5.0%)	17.6σ
5–10%	331.2	0.338 ± 0.029 (8.7%) $\pm\, 0.024$ (7.0%)	14.9σ
10–15%	283.0	0.325 ± 0.031 (9.5%) $\pm\, 0.015$ (4.7%)	16.4σ
15–20%	241.0	0.317 ± 0.033 (10.4%) $\pm\, 0.024$ (7.5%)	14.8σ
20–30%	187.9	0.403 ± 0.031 (7.8%) $\pm\, 0.025$ (6.2%)	12.2σ
30–40%	130.8	0.412 ± 0.037 (8.9%) $\pm\, 0.017$ (4.2%)	11.9σ
40–50%	87.1	0.456 ± 0.053 (11.7%) $\pm\, 0.023$ (5.1%)	8.2σ
50–70%	42.7	0.450 ± 0.061 (13.5%) $\pm\, 0.023$ (5.1%)	7.6σ
70–90%	11.4	0.864 ± 0.174 (20.1%) $\pm\, 0.082$ (9.5%)	0.7σ
0–30%	269.1	0.336 ± 0.013 (3.9%) $\pm\, 0.015$ (4.5%)	21.7σ
30–90%	54.3	0.441 ± 0.027 (6.1%) $\pm\, 0.022$ (4.9%)	12.2σ

Table 4.13: Nuclear modification factor of Υ(1S) for centrality classes. The correlated systematic uncertainty is 6.9%.

Centrality class	$\langle N_{\text{part}} \rangle$	$R_{\text{AA}}^{\Upsilon(2\text{S})} \pm$ stat $\pm$ syst	std dev to 1
0–30%	269.1	0.104 ± 0.026 (24.7%) $\pm\, 0.024$ (23.4%)	24.4σ
30–90%	54.3	0.226 ± 0.057 (25.3%) $\pm\, 0.032$ (14.3%)	11.3σ

Table 4.14: Nuclear modification factor of Υ(2S) for centrality classes. The correlated systematic uncertainty is 8.7%.

Thanks to the relatively large Pb–Pb data sample, we can measure the production of the $\Upsilon(2S)$ excited state for two centrality classes. The nuclear modification factors reported in Table 4.14 show once again that this production is strongly suppressed. The systematic uncertainty correlated with the centrality is 8.7%. With a 1.6σ difference between the measurements within the 0–30% and 30–90% intervals, much more data are needed to conclude on a centrality dependence for the $\Upsilon(2S)$ suppression.

The results are displayed in Figure 4.6 as a function of the average number of participant nucleons. For the ground state, the suppression is more important for central collisions. The R_{AA} of $\Upsilon(1S)$ is compatible with unity for the most peripheral events and saturates to ≈ 0.32 for $\langle N_{\mathrm{part}} \rangle \gtrsim 200$. Visually, the measurements within the two most peripheral intervals indicate a decrease steeper than we can observe for inclusive J/ψ [76]. It would be interesting to see if the models reproduce this centrality dependence.

We evaluate the relative suppression between the two states via the double ratio defined in the equation 4.8 and reported in Table 4.15 for two centrality classes. As we already stated for the $\Upsilon(2S)$-to-$\Upsilon(1S)$ yield ratio, the results are compatible within the statistical uncertainties. The relative production is lower than in proton–proton collisions, especially for central Pb–Pb collisions. Figure 4.7 shows the double ratio as a function of $\langle N_{\mathrm{part}} \rangle$. Thanks to the small uncertainty of the interpolated cross-section ratio in pp collisions, as well as to the cancellation of the other uncertainties correlated with the centrality, the global uncertainty is reduced from 9.2% to 1.2% with respect to the R_{AA} of $\Upsilon(1S)$ and $\Upsilon(2S)$. Moreover, the relative systematic uncertainties are about 4% smaller when accounting for correlations in the signal extraction. The double ratio will be useful to confront the different approaches describing the production of bottomonia in heavy-ion collisions.

Centrality class	$\langle N_{\mathrm{part}} \rangle$	$R_{\mathrm{AA}}^{\Upsilon(2S)/\Upsilon(1S)} \pm$ stat $\pm$ syst	std dev to 1
0–30%	269.1	0.321 ± 0.081 (25.2%) ± 0.065 (20.4%)	6.5σ
30–90%	54.3	0.530 ± 0.136 (25.6%) ± 0.058 (10.9%)	3.2σ

Table 4.15: Double production ratio between the $\Upsilon(2S)$ and $\Upsilon(1S)$ states for centrality classes. The correlated systematic uncertainty is 1.2%.

Transverse momentum dependence

Let us now investigate the suppression features with the kinematic variables over the whole 0–90% centrality class. The nuclear modification factor for the $\Upsilon(1S)$ and $\Upsilon(2S)$ states as a function of their transverse momenta are reported in Tables 4.16 and 4.17 respectively. Their production is significantly suppressed for all p_{T} ranges up to 15 GeV/c. The results shown in Figure 4.8 do not indicate any variation with the transverse momentum.

We notice that the R_{AA} of $\Upsilon(1S)$ does not vary with p_{T} within uncertainties. This observation is in contrast with the dependence measured for J/ψ [77] and represented in Figure 4.9. For the latter bound state, the weaker suppression in the low-momentum region, i.e. for $p_{\mathrm{T}} \lesssim 4$ GeV/c, is one of the evidence for the charmonium regeneration at the LHC. No sign of this phenomenon is visible from the sizeable uncertainties and due to the limited range of our measurement.

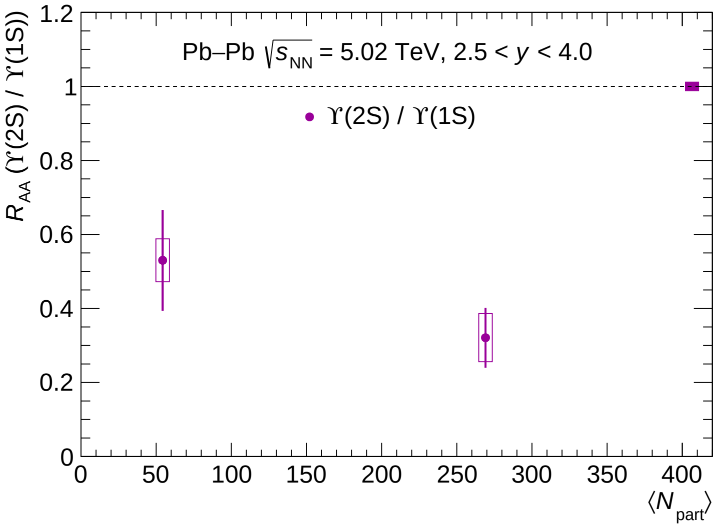

Figure 4.7: Double production ratio between the ϒ(2S) and ϒ(1S) states as a function of the number of participants in Pb–Pb collisions.

p_{T} range	$R_{\mathrm{AA}}^{\Upsilon(1\mathrm{S})}$ ± stat ± syst	std dev to 1
$0 < p_{\mathrm{T}} < 2$ GeV/c	0.345 ± 0.031 (9.0%) ± 0.039 (11.4%)	13.0σ
$2 < p_{\mathrm{T}} < 4$ GeV/c	0.387 ± 0.022 (5.7%) ± 0.035 (9.1%)	14.6σ
$4 < p_{\mathrm{T}} < 6$ GeV/c	0.345 ± 0.021 (6.2%) ± 0.026 (7.6%)	19.1σ
$6 < p_{\mathrm{T}} < 9$ GeV/c	0.298 ± 0.027 (9.0%) ± 0.039 (13.1%)	14.8σ
$9 < p_{\mathrm{T}} < 15$ GeV/c	0.364 ± 0.044 (12.0%) ± 0.065 (17.8%)	8.1σ

Table 4.16: Nuclear modification factor of ϒ(1S) as a function of p_{T} within the 0–90% centrality interval. The correlated systematic uncertainty amounts to 1.5%

Furthermore, it is interesting to note that the production of ϒ mesons in p–Pb collisions is significantly suppressed at low p_{T}, in any rapidity region probed at the LHC [52, 78, 79]. The corresponding nuclear modification factor of ϒ(1S) decreases from unity at intermediate p_{T} down to 0.5 for $p_{\mathrm{T}} \lesssim 5$ GeV/c for forward rapidities [52, 79]. As a result, the R_{AA} measured in the low-p_{T} region could be explained solely by the convolution of effects present in proton–nucleus collisions. This striking difference in the p_{T} spectrum between the two collision systems should receive close attention from a phenomenological point of view.

Rapidity dependence

Thanks to a dedicated interpolation procedure for y-differential reference cross sections, we can determine the nuclear modification factor of ϒ(1S) within the narrow rapidity intervals listed in Table 4.18. At first glance, the R_{AA} is lower in the two most forward intervals with respect to the other results obtained. As for centrality, we would like to know if this potential rapidity dependence is significant. The difference in results between

p_{T} range	$R_{\mathrm{AA}}^{\Upsilon(2\mathrm{S})}$ ± stat ± syst	std dev to 1
$0 < p_{\mathrm{T}} < 4$ GeV/c	0.121 ± 0.038 (31.4%) ± 0.033 (27.2%)	17.5σ
$4 < p_{\mathrm{T}} < 15$ GeV/c	0.139 ± 0.036 (25.6%) ± 0.016 (11.8%)	22.0σ

Table 4.17: Nuclear modification factor of $\Upsilon(2\mathrm{S})$ as a function of p_{T} within the 0–90% centrality interval. The correlated systematic uncertainty amounts to 1.5%

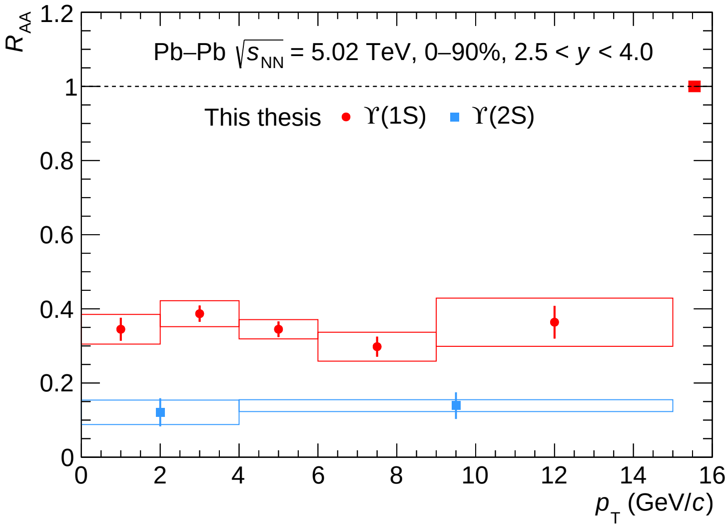

Figure 4.8: Nuclear modification factor of $\Upsilon(1\mathrm{S})$ and $\Upsilon(2\mathrm{S})$ as a function of p_{T} at forward rapidity within the 0–90% centrality interval.

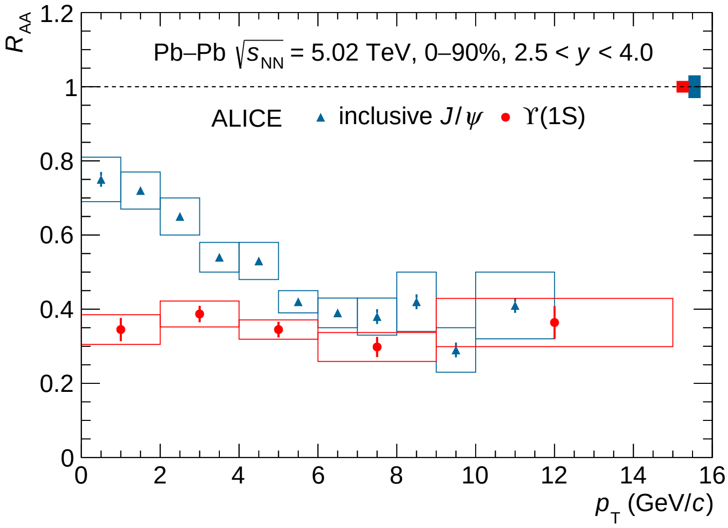

Figure 4.9: Nuclear modification factor of $\Upsilon(1\mathrm{S})$ and inclusive J/ψ [77] as a function of p_{T} at forward rapidity within the 0–90% centrality interval.

Rapidity interval	$R_{\mathrm{AA}}^{\Upsilon(1\mathrm{S})}$ ± stat ± syst	std dev to 1
$2.5 < y < 2.8$	0.433 ± 0.043 (9.9%) ± 0.054 (12.4%)	8.2σ
$2.8 < y < 3.1$	0.396 ± 0.023 (5.8%) ± 0.035 (8.9%)	14.3σ
$3.1 < y < 3.3$	0.398 ± 0.029 (7.3%) ± 0.041 (10.3%)	11.9σ
$3.3 < y < 3.6$	0.338 ± 0.021 (6.2%) ± 0.040 (12.0%)	14.5σ
$3.6 < y < 4.0$	0.305 ± 0.032 (10.6%) ± 0.048 (15.7%)	12.0σ

Table 4.18: Nuclear modification factor of $\Upsilon(1\mathrm{S})$ as a function of rapidity within the 0–90% centrality interval. The global uncertainty is 1.5%.

Rapidity interval	$R_{\mathrm{AA}}^{\Upsilon(2\mathrm{S})}$ ± stat ± syst	std dev to 1
$2.5 < y < 3.3$	0.081 ± 0.030 (37.1%) ± 0.032 (40.1%)	20.2σ
$3.3 < y < 4.0$	0.197 ± 0.040 (20.1%) ± 0.035 (17.7%)	14.4σ

Table 4.19: Nuclear modification factor of $\Upsilon(2\mathrm{S})$ as a function of rapidity within the 0–90% centrality interval. The global uncertainty is 1.5%.

the most forward measurements and the other intervals is always above 1.5 standard deviations, with a maximum of 2σ between the $2.8 < y < 3.1$ and $3.6 < y < 4.0$ intervals. These estimations are limited by our lack of knowledge of the correlation of the reference cross-section uncertainties. Since we assume that the latter are fully uncorrelated with rapidity, we *undervalue* the true significance of the difference between our results. Hence, the current uncertainties prevent any conclusion on a stronger suppression of $\Upsilon(1\mathrm{S})$ with increasing rapidity. The confirmation of such a dependence requires a precise y-differential measurement of the production cross section in pp collisions. Future data takings will make this possible, while at the same time reducing the statistical uncertainties [80].

With the first measurement of the $\Upsilon(2\mathrm{S})$ production in nucleus–nucleus collisions in the forward region comes the first determination of the R_{AA} as a function of rapidity within the same acceptance. The results obtained are reported in Table 4.19. As the comparison of the production cross sections between Pb–Pb and pp collisions already suggested, cf. Section 4.2.3, the suppression is weaker for $3.3 < y < 4.0$. The measurements within the two rapidity ranges differ by 1.9σ but we must keep in mind the sizeable uncertainties from the signal extraction before interpreting this deviation.

Figure 4.10 shows the nuclear modification factor of the $\Upsilon(1\mathrm{S})$ and $\Upsilon(2\mathrm{S})$ states as a function of rapidity. For the ground state, the two most forward measurement points hint of a decrease towards larger rapidity within the ALICE acceptance. Interestingly, we observe an opposite trend for the R_{AA} of $\Upsilon(2\mathrm{S})$. Although these are only indications, the comparison of our data with the models should tell us if rapidity dependencies are expected.

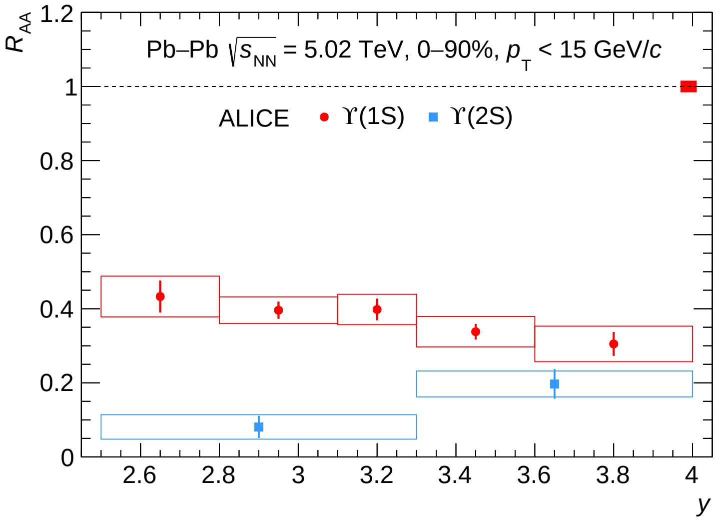

Figure 4.10: Nuclear modification factor of ϒ(1S) and ϒ(2S) as a function of rapidity. The red box at unity represents the global uncertainty (1.5%) common to both states.

4.3.2 Comparison with CMS measurements

In order to put our results into perspective, we will discuss them with the measurements reported by the CMS collaboration [72, 81]. The nuclear modification factors integrated over the respective acceptances are listed in Table 4.20. We find an excellent agreement for the three resonances even though the rapidity coverage is totally different. Our estimation of the upper limit on the $R_{\rm AA}$ of ϒ(3S) is consistent with the value quoted by CMS. No sign of ϒ(3S) production in heavy-ion collisions has been observed to date.

$R_{\rm AA}$	this thesis	CMS (0–100%, $\lvert y\rvert < 2.4$)	standard dev.
ϒ(1S)	$0.353 \pm 0.012 \pm 0.029$	$0.376 \pm 0.013 \pm 0.035$	0.5σ
ϒ(2S)	$0.128 \pm 0.024 \pm 0.026$	$0.117 \pm 0.022 \pm 0.019$	0.2σ
ϒ(2S)/ϒ(1S)	$0.371 \pm 0.071 \pm 0.057$	$0.308 \pm 0.051 \pm 0.019$	0.6σ
ϒ(3S)	$0.010 \pm 0.049 \pm 0.012$	$0.022 \pm 0.038 \pm 0.016$	0.2σ
ϒ(3S)	< 0.117 at a 95% C.L.	< 0.096 at a 95% C.L.	

Table 4.20: Integrated nuclear modification factors reported in Section 4.3.1 and by the CMS collaboration, as well as the standard deviation between the measurements.

The nuclear modification factors as a function of $\langle N_{\rm part}\rangle$ are represented in Figure 4.11. Based on the CMS data, we can now confirm the centrality dependence of the suppression of the ϒ(1S) production. The data are remarkably compatible for $\langle N_{\rm part}\rangle > 150$, i.e. for the 0–30% most central collisions, and start to deviate towards peripheral events.

Both ALICE and CMS measurements show that the $R_{\rm AA}$ of ϒ(1S) saturates to a value around 0.32 for the 0–20% most central collisions. For the excited state, the decrease is only significant for peripheral events. Our results are not sensitive to this feature given the large centrality intervals wherein a ϒ(2S) signal could be measured.

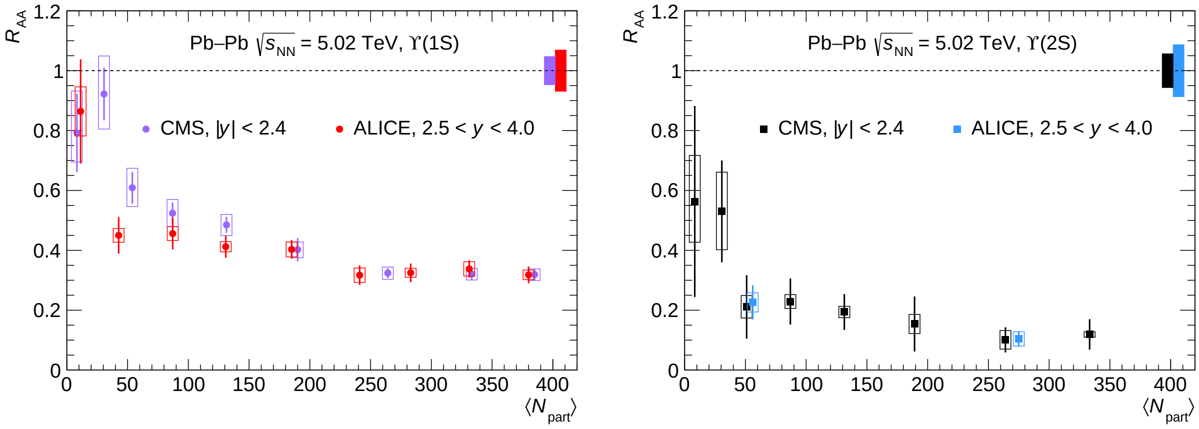

Figure 4.11: Nuclear modification factor of (left) ϒ(1S) and (right) ϒ(2S) as a function of the number of participants in Pb–Pb collisions at $\sqrt{s_{\mathrm{NN}}} = 5.02$ TeV. Some points are deliberately shifted along the abscissa axis to avoid overlapping.

Finally, we comment on the rapidity dependence of the nuclear modification factors displayed in Figure 4.12. The complementarity of the acceptances allows us to notice that the R_{AA} of ϒ(1S) is constant around 0.4 within uncertainties between midrapidity and $y \approx 3.3$. The most forward measurement point is one standard deviation lower than the rapidity-integrated CMS result. The R_{AA} for the ϒ(2S) state is flat as a function of rapidity within the sizeable uncertainties, with values ranging from 0.05 and 0.20.

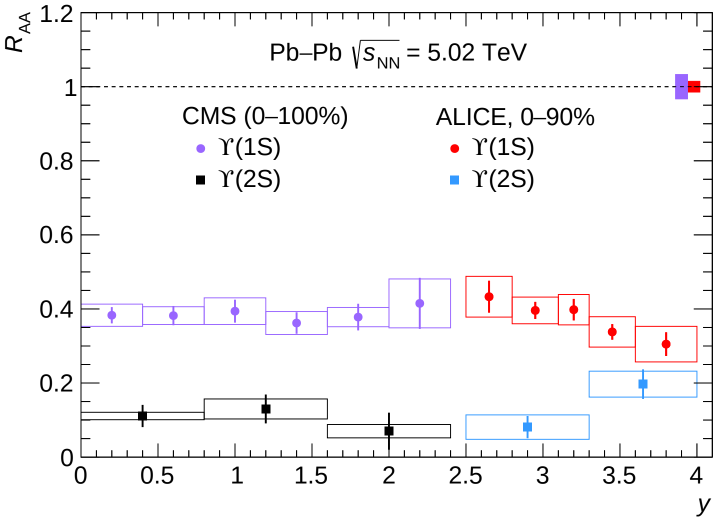

Figure 4.12: Nuclear modification factor of ϒ(1S) and ϒ(2S) as a function of rapidity. The red and violet filled boxes at unity correspond to the global uncertainties common to both states from the ALICE and CMS measurements.

4.3.3 Comparison with model calculations

The nuclear modification factors presented along Section 4.3.1 exhibit intriguing patterns. To interpret these observations, we compare our measurements with available phenomenological predictions. The calculations introduced hereafter are all based on transport or rate equations. All the models account for the modification of the feed-down contributions from the decay of heavier bottomonium states.

Comover interaction model [82]

Within this picture, quarkonia are dissociated by scattering with surrounding *comoving* particles in the final state. Successfully applied for proton–nucleus collisions, the revisited version of this model aims to explain the suppression of bottomonia in both p–Pb and Pb–Pb collision systems with the same assumptions. The calculations take into account the nuclear modification of PDFs using the nCTEQ15 fit parametrisation [83] for the absolute suppressions. Uncertainties from shadowing and comover-Υ interaction cross sections are depicted together in the figures as grids.

Hydrodynamic calculations [84]

The hydrodynamic framework predicts the survival probability of bottomonia inside an anisotropic plasma. The decay rate encodes the thermal modification of a complex-valued heavy-quark potential. The background medium is described with viscous hydrodynamics for three values of the shear-viscosity-to-entropy density ratio η/s. These calculations do not include any modification of nuclear PDFs or any regeneration phenomenon.

Transport approaches [85, 86]

The transport approaches describe an interplay of dissociation and regeneration mechanisms regulating the production of bottomonia at the QGP stage.

For the transport model [85], the medium evolves as an expanding isotropic fireball. Results are provided with and without the presence of a regeneration component. The uncertainty bands denote the shadowing correction on the initial number of $\mathrm{b\overline{b}}$ pairs by a factor varying from 0 to 30% for central collisions.

In the framework of coupled Boltzmann equations [86], the regeneration is dominated by real-time recombinations of correlated heavy quarks. The simulation of the collision system includes the EPPS16 nPDF parametrisation [87] and viscous hydrodynamics. In the figures, the calculations are shown with a band due to the nPDF uncertainty and with three curves from the variation of the coupling constants.

Let us start with the centrality dependence of the nuclear modification factors. The various calculations shown in Figure 4.13 globally reproduce the decreasing trend observed in data. For Υ(1S), the measurement points lie on the lower limit of the predictions from the comover interaction model and from the coupled Boltzmann equations. These predictions come with large uncertainties due to the poorly-constrained nPDF parametrisations used. We notice that all the calculations are in tension with the R_{AA} measured for $\langle N_{\mathrm{part}} \rangle \approx 50$, corresponding to the 50–70% centrality interval. This deviation may be explained by an event-selection bias on multiplicity for peripheral collisions, leading to an apparent stronger suppression as discussed in a recent publication [88]. Surprisingly, this specific point is better described by the models for Υ(2S). The suppression of the excited state is in agreement with the models. The sharp slope expected for the R_{AA} of Υ(2S) in the peripheral region is not measurable because of statistical limitations, as we already mentioned in the Comparison with CMS measurements.

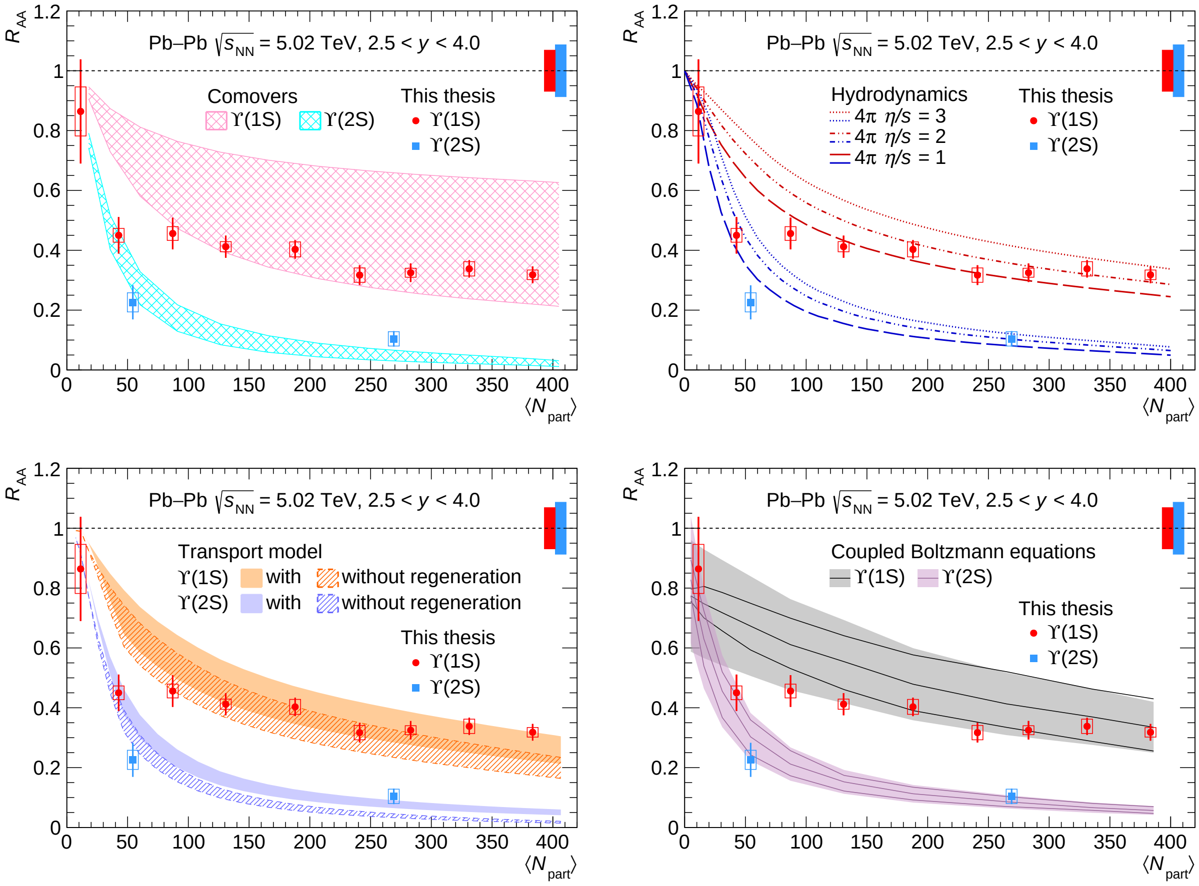

Figure 4.13: Nuclear modification factor of ϒ(1S) and ϒ(2S) as a function of the average number of participants in Pb–Pb collisions at $\sqrt{s_{NN}} = 5.02$ TeV. The four panels show the predictions from (top-left) the comover interaction model [82], (top-right) hydrodynamic calculations [84] and (bottom) the transport approaches [85, 86] described in the text.

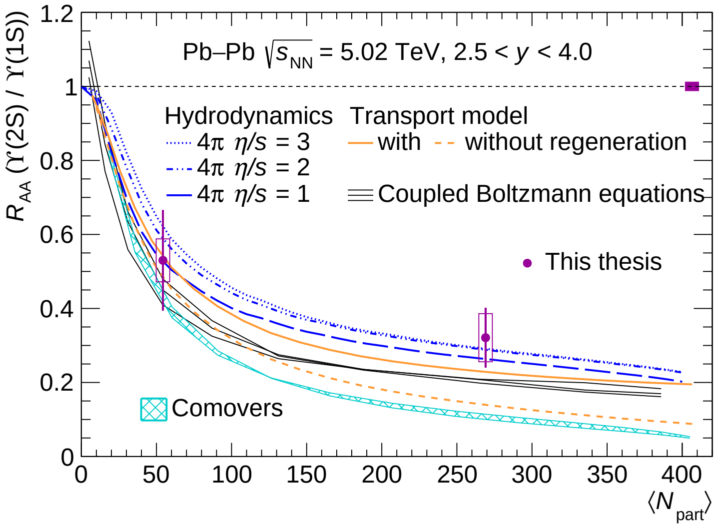

Figure 4.14: Double production ratio between the Υ(2S) and Υ(1S) states as a function of the average number of participants in Pb–Pb collisions at $\sqrt{s_{\mathrm{NN}}} = 5.02$ TeV, along with the calculations introduced previously.

To confront the different approaches, we inspect the relative suppression between the Υ(2S) and Υ(1S) states via the double ratio defined in the equation 4.8. This observable is a powerful tool because effects common to both states are expected to disappear as indicated by the smaller uncertainties in Figure 4.14 compared to Figure 4.13. Nuclear shadowing and PDF parametrisations do not enter in the model calculation of the double ratio. In addition, most of the sources of experimental systematic uncertainty are supposed to cancel out. The various approaches indicate a relative suppression getting stronger towards central collisions but with slightly different slopes as a function of $\langle N_{\mathrm{part}} \rangle$. The data point for peripheral events is compatible with all the curves within a large statistical uncertainty. The comover interaction model shows a deviation of about 2σ with respect to the measurement for the 0–30% most central interval, also noticed in a comparison with CMS data [82]. Interestingly, for the transport approaches, larger values of the double ratio are achieved by the large regeneration component of the Υ(2S) production. The hydrodynamic calculations describe well the data, whatever the value of η/s. With more precise measurements, the excited-to-ground state relative production could serve as a model discriminator thanks to the cancellation of sources of systematic uncertainty.

The nuclear modification factors as a function of transverse momentum are compared with the hydrodynamic and transport calculations in Figure 4.15. No significant variation is observed up to 15 GeV/c, in line with model expectations. The mild p_{T}-dependence of the hydrodynamic predictions originates from the non-relativistic treatment of the heavy-quark model potential [84]. Our measurements for Υ(1S) suppression disfavour the hydrodynamic calculation for the highest shear-viscosity-to-entropy density ratio. For the transport model [85], the presence of a regeneration component would result in a wide bump structure centred at $p_{\mathrm{T}} \sim m_{\Upsilon(1\mathrm{S})}$, and account for approximately 40% of the R_{AA} for Υ(2S) at low p_{T}. The current experimental and theoretical uncertainties do not permit to rule out one of the two scenarios.

Figure 4.16 shows the rapidity dependence of the nuclear modification factors within

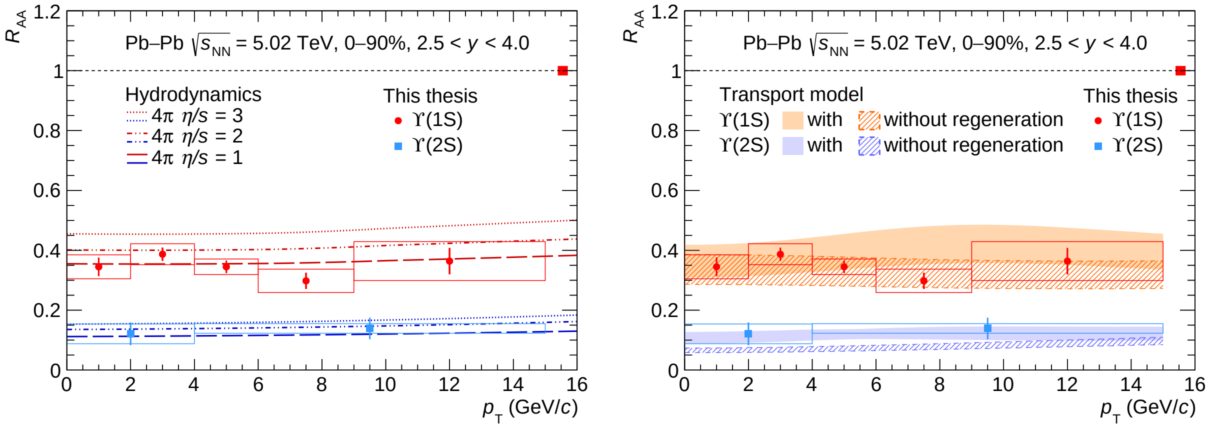

Figure 4.15: Nuclear modification factor of $\Upsilon(1S)$ and $\Upsilon(2S)$ as a function of p_T, together with (left) hydrodynamic and (right) transport model predictions.

$2.5 < y < 4.0$. We compare our results with the hydrodynamic predictions as well as with the calculations based on the coupled Boltzmann equations. These models do not capture the decreasing trend observed for the R_{AA} of $\Upsilon(1S)$. The hydrodynamic calculations indicate an opposite behaviour. In this model, the rapidity profile inherits from the initial conditions of the simulated medium [84]. The most forward measurement point sits three standard deviations below the predictions for $4\pi\ \eta/s = 3$. The results from the coupled Boltzmann equations exhibit a structure induced by the nPDF [86]. None of the curves can describe the measurement consistently over the whole ALICE acceptance, albeit the most forward data points lie on the edge of the uncertainty band. These discrepancies suggest that the presently available models miss a physical mechanism to explain a rapidity-dependent suppression. For $\Upsilon(2S)$, the model shapes are similar to the one observed for the ground state. We notice that the coupled Boltzmann equations predict a suppression two times stronger than the hydrodynamic calculations. The results are compatible with our measurements within the large uncertainties.

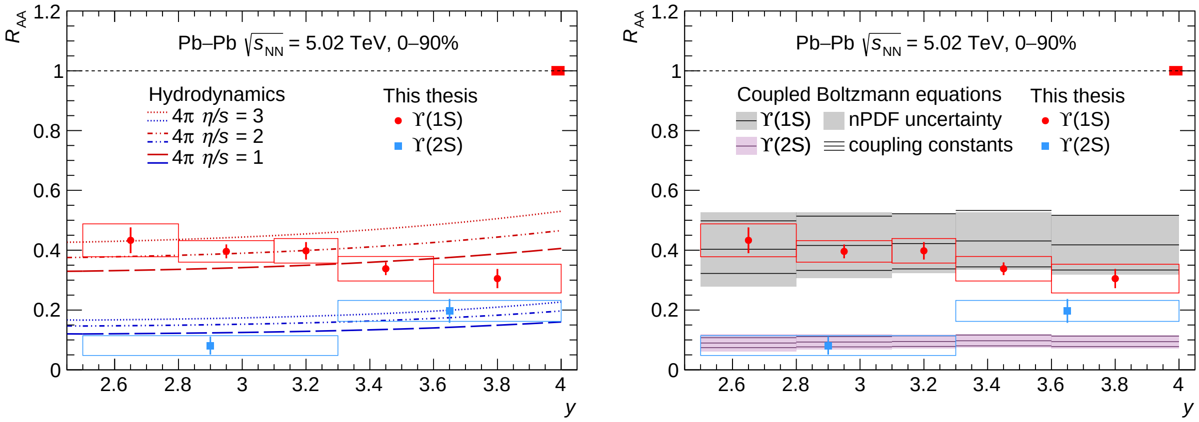

Figure 4.16: Nuclear modification factor of $\Upsilon(1S)$ and $\Upsilon(2S)$ as a function of rapidity. The left panel shows the hydrodynamic calculations while results from the coupled Boltzmann equations are displayed in the right panel.

Conclusions and outlook

Throughout this thesis we have studied the production of Υ mesons in proton–proton and Pb–Pb collisions at the LHC. The signal of individual bound states was measured from their decay into opposite-sign muon pairs reconstructed by the muon spectrometer of the ALICE apparatus. In order to precisely quantify the suppression with the nuclear modification factor R_{AA} observable, we have estimated the reference cross sections from an interpolation procedure based on available experimental data.

Thanks to the total luminosity collected during the Run 2 data takings, we could perform a detailed measurement of $\Upsilon(1\mathrm{S})$ production at forward rapidity ($2.5 < y < 4.0$) in Pb–Pb collisions at $\sqrt{s_{\mathrm{NN}}} = 5.02$ TeV [89]. Nuclear modification factors determined for various centrality classes indicate a strong suppression enhancing with the number of participant nucleons, up to a factor three for the most central events. No variation with the transverse momentum is found within the accessible range of the present data sample. This observation contrasts sharply with the trends notable for J/ψ production [77] and in p–Pb collisions [52, 78, 79]. Combined with the CMS data, these measurements constrain the rapidity dependence of Υ production over four units of rapidity. The results suggest a mild decrease of the R_{AA} towards more forward rapidities, with a 2σ significance within the acceptance of the ALICE muon spectrometer.

We also have investigated the suppression of the excited states. For the first time, the $\Upsilon(2\mathrm{S})$ resonance is observed in the forward rapidity region in heavy-ion collisions. Its production is suppressed by a factor ten for the 0–30% centrality interval, corresponding to a suppression stronger than for $\Upsilon(1\mathrm{S})$ by about a factor three. The limited number of measurement points as well as large uncertainties prevent us from drawing conclusions about any centrality, p_{T} or rapidity dependence. We can nevertheless remark that our findings are consistent with the results obtained at midrapidities by the CMS collaboration [72]. Lastly, no significant $\Upsilon(3\mathrm{S})$ signal could be measured. Based on an estimate of the yield upper limit, we found that the production of the most loosely bound state is at least as suppressed as the $\Upsilon(2\mathrm{S})$ meson.

These results were compared with predictions from diverse modellings of bottomonium production and interactions in nucleus–nucleus collisions. Although the calculations are in general agreement with the data, they do not exhibit certain observed features. For instance, all the approaches manifest a monotonic increase of the $\Upsilon(1\mathrm{S})$ suppression with the collision centrality while the measurements reach a plateau from the 20% most central events. None of the available models is able to reproduce the drop of the R_{AA} at forward rapidity, either because of opposite expectations or inconsistency in the description of the data points. These particularities highlight the relevance of phenomena other than the mere QGP effects advanced so far. Browsing the literature, nuclear modification factors derived from the coherent energy loss model [90] show intriguing similarities with the present measurements, such as a decreasing trend at forward rapidity. It would then be appealing to consider this effect in future theoretical studies in view of establishing a comprehensive picture of quarkonium production in relativistic heavy-ion collisions.

Despite the precision of Run 2 measurements, several factors limit the interpretation of the results. On one hand, we have reached a stage where experimental data for ground-state production are more precise than most of the model predictions. The latter come with large uncertainties induced by poorly-constrained nPDFs when considered in the calculations. On the other hand, differential measurements are dominated by systematic uncertainties, notably from the proton–proton cross sections. In the future it will be crucial to measure the reference cross sections instead of relying on an interpolation procedure. Direct measurements could for instance elucidate the origin of the behaviour observed at forward rapidities, especially if detector effects are involved.

At the dawn of Run 3 we can hope for experimental and theoretical improvements in the upcoming years based on projections for the high-luminosity LHC phase [80]. The heavy-ion physics programme will significantly benefit from the luminosity increase and detector upgrades. In the quarkonium sector, large data samples offer the possibility to study in detail the suppression of excited states and to search for those still unobserved in nuclear collision systems. Precise p_{T}-differential observables may allow to conclude about the relevance of regeneration in bottomonium production. In addition, these improvements should be complemented by a more robust handling of the feed-down contributions as well as a better description of parton distributions in the initial state, achievable with the inclusion of new data in global nuclear PDF fits [91, 92].

Appendix A

Signal extraction functions

This appendix provides the analytical formulation of the different functions employed in the signal extraction procedure, cf. Section 3.2.2. A typical fitting model consists of one extended Crystal Ball distribution per resonance and one or more background functions depending on the complexity of the dimuon continuum.

A.1 Extended Crystal Ball distribution (CB2)

Traditionally, the signal shape is modelled by a Gaussian function centred at the particle pole mass m_0 and with a width σ reflecting the detector resolution. In the present studies, the Υ candidates are reconstructed with muons losing energy along their path. This effect deforms the signal shape towards the lower dimuon invariant mass region. To also account for residual misalignements, the extended Crystal Ball distribution is a Gaussian core prolonged by a power-law tail on each side. The CB2 is written as

$$f(m; m_0, \sigma, N, \alpha, n, \alpha', n') = N \times \begin{cases} \frac{A}{(B-t)^n} & \text{for } t \leq -\alpha \\ \exp\left(-\frac{t^2}{2}\right) & \text{for} -\alpha < t < \alpha' \\ \frac{C}{(D+t)^{n'}} & \text{for } t \geq \alpha' \end{cases}$$

with the reduced variable $t = \frac{m-m_0}{\sigma}$, the normalisation factor N and

$$A = \left(\frac{n}{|\alpha|}\right)^n \times \exp\left(-\frac{\alpha^2}{2}\right), \quad B = \frac{n}{|\alpha|} - |\alpha|,$$

$$C = \left(\frac{n'}{|\alpha'|}\right)^{n'} \times \exp\left(-\frac{\alpha'^2}{2}\right), \quad D = \frac{n'}{|\alpha'|} - |\alpha'|.$$

The α, n, α', n' tail parameters are fixed to the values extracted from the signal shape reconstructed in Monte Carlo simulations. The parameters used for the Pb–Pb analysis as a function of the collision centrality are reported in Table A.1. One can notice that the right tail strongly depends on the centrality class. For the rapidity and p_{T}-differential studies, the values can be found in Table A.2.

Centrality class	α	n	α'	n'
0–5%	0.83	2.41	1.73	2.28
5–10%	0.84	2.40	1.76	2.31
10–15%	0.86	2.37	1.82	2.27
15–20%	0.86	2.35	1.79	2.42
20–30%	0.87	2.36	1.87	2.38
30–40%	0.88	2.34	1.90	2.48
40–50%	0.89	2.31	1.93	2.54
50–70%	0.90	2.32	1.98	2.55
70–90%	0.90	2.31	1.99	2.67
0–30%	0.85	2.37	1.81	2.33
30–90%	0.89	2.32	1.96	2.56

Table A.1: CB2 tail parameters of the Υ signal shape reconstructed with the embedding MC simulations for the centrality classes studied in the Pb–Pb analysis.

Rapidity interval	p_{T} range [GeV/c]	GEANT3				GEANT4				pp $\sqrt{s} = 5.02$ TeV			
		α	n	α'	n'	α	n	α'	n'	α	n	α'	n'
$2.5 < y < 4.0$	$0 < p_{\mathrm{T}} < 15$	0.88	2.34	1.91	2.44	0.98	2.18	2.01	2.73	0.99	2.03	2.07	2.31
$2.5 < y < 2.8$	$0 < p_{\mathrm{T}} < 15$	0.66	2.67	2.08	3.08	0.88	2.24	2.21	3.69	0.73	2.36	2.20	3.33
$2.8 < y < 3.1$		0.86	2.31	2.01	2.73	0.96	2.15	2.10	3.14	0.95	2.06	2.14	2.75
$3.1 < y < 3.3$		0.93	2.24	1.87	2.67	1.00	2.13	1.97	2.89	1.04	1.96	2.03	2.48
$3.3 < y < 3.6$		0.96	2.23	1.76	2.52	1.04	2.13	1.85	2.84	1.09	1.91	1.93	2.29
$3.6 < y < 4.0$		0.98	2.23	1.69	2.36	1.07	2.12	1.78	2.84	1.17	1.79	1.88	2.17
$2.5 < y < 3.3$	$0 < p_{\mathrm{T}} < 15$	0.85	2.35	1.98	2.71	0.96	2.16	2.10	2.96	1.02	2.45	1.97	1.97
$3.3 < y < 4.0$		0.96	2.25	1.75	2.43	1.04	2.14	1.83	2.81	1.10	1.90	1.92	2.25
$2.5 < y < 4.0$	$0 < p_{\mathrm{T}} < 2$	0.82	2.37	1.91	2.86	0.92	2.20	2.07	3.13	0.93	1.99	2.12	2.70
	$2 < p_{\mathrm{T}} < 4$	0.87	2.27	1.92	2.70	0.97	2.11	2.05	2.95	0.96	1.96	2.11	2.56
	$4 < p_{\mathrm{T}} < 6$	0.91	2.28	1.93	2.45	1.00	2.14	2.00	2.81	0.97	2.02	2.10	2.41
	$6 < p_{\mathrm{T}} < 9$	0.91	2.46	1.85	2.31	1.01	2.29	1.93	2.63	0.98	2.20	2.04	2.31
	$9 < p_{\mathrm{T}} < 15$	0.95	2.61	1.79	2.07	1.03	2.51	1.81	2.44	1.02	2.45	1.97	1.97

Table A.2: CB2 tail parameters of the Υ signal shape reconstructed in Monte Carlo simulations.

A.2 Background functions

In the Pb–Pb data, an important combinatorial background dominates the dimuon invariant mass spectrum, more particularly in the low mass region. The description of the background shape requires functions with four parameters.

A.2.1 Sum of two exponentials (2Exp)

The sum of two decreasing exponentials allows to model the low and high mass regions beside the Υ signal *separately.*

$$f(m; N_1, \lambda_1, N_2, \lambda_2) = N_1 \times \exp\left(-\lambda_1 m\right) + N_2 \times \exp\left(-\lambda_2 m\right)$$

with the constraint $\lambda_1 > \lambda_2$ i.e. the background slope is steeper on one side.

A.2.2 Variable-width Gaussian (VWG)

This function is a pseudo-Gaussian defined like

$$f(m; N, \mu, \alpha, \beta) = N \times \exp\left(-\frac{(m-\mu)^2}{2\sigma^2}\right) \text{ with } \sigma = \alpha + \beta \times \left(\frac{m-\mu}{\mu}\right).$$

Appendix B

Interpolation of reference cross sections

A precise evaluation of nuclear modification factors requires a low uncertainty on the production cross section in proton–proton collisions. In Section 4.1.1, we have presented the results of the first direct measurement of Υ production at $\sqrt{s}$ = 5.02 TeV in the forward rapidity region. The statistical uncertainties as well as the differential intervals would limit the potential of the R_{AA} study. To overcome these constraints, we estimate the reference cross sections based on experimental measurements performed at various centre-of-mass energies at the LHC.

This appendix gives the complete description of the interpolation procedures adopted. All the intermediate results and the fit distributions are provided in Section B.1.2 for the $2.5 < y < 4.0$ interval, and in Sections B.1.3 and B.1.4 for the rapidity and p_{T}-differential cross sections, respectively. The study of the nuclear modification factor as a function of rapidity demands an extra step developed in Section B.2.

Since the branching fraction disappears in the computation of the R_{AA}, we consider the product of the dimuon branching fraction and the Υ production cross section, henceforth noted $\sigma_{\Upsilon\to\mu^+\mu^-}$ for the sake of writing.

B.1 Energy interpolation

The goal is to determine the cross sections at $\sqrt{s} = 5.02$ TeV from existing measurements. Given the kinematic region studied, we will exploit the results obtained by ALICE at 7 and 8 TeV [68,69], by LHCb at 2.76, 7, 8 and 13 TeV [62,70,71] as well as the results at 5.02 TeV obtained in this thesis in Section 4.1.1. The statistical and systematic uncertainties are added in quadrature. When both collaborations report a cross section at the same centre-of-mass energy, as is the case at 7 and 8 TeV, in the same p_{T} and rapidity interval, the point is taken as the average of the two results weighted by the inverse of their total uncertainty squared. This operation assumes that the measurements are not correlated between experiments.

B.1.1 Procedure

Our strategy is based on LHCb's approach to determine the reference cross sections of $\Upsilon(1S)$ for p–Pb studies [93]. The number of available data points is sufficient to perform the interpolation with empirical functions only. The selection of the functions employed is guided by the energy dependence of the cross section. Coming back to Figure 4.1, we can observe that the measurements form an almost straight line extending close to the origin. The parametrisations should exhibit monotonous growth and cancel in zero if one neglects threshold effects[†]. In addition, the phase space enlarges as the centre-of-mass energy increases. The p_{T} spectrum gets broader while the forward rapidity region becomes more and more accessible. As a result, the production cross section does not evolve linearly with the energy for certain kinematic intervals so the shapes could have some curvature. Finally, the number of degrees of freedom must be sufficient to guarantee the fit quality. With a minimum of four data points, we can thus consider functions with two free parameters a and b, namely

- linear: $a \times \sqrt{s} + b$
- parabola: $a \times \sqrt{s}^2 + b \times \sqrt{s}$
- exponential: $\sqrt{s} \times \exp\left(a \times \sqrt{s} + b\right)$
- logarithm: $a \times \sqrt{s} \times \log(\sqrt{s}) + b$
- power law: $a \times \sqrt{s}^b$.

The parabola, the exponential and the power law pass by the origin with the possibility to have both negative and positive curvature. The linear and logarithmic trends avoid the constraint on the cancellation of the cross section at $\sqrt{s} = 0$.

Let us go through the steps of this procedure.

1) Each function is fitted to the data points as a function of the centre-of-mass energy. The evaluation of the resulting function at $\sqrt{s} = 5.02$ TeV defines the interpolated cross section σ_i. The fit provides an error ε_i and a reduced chi-square $\tilde{\chi}_i^2 \equiv \chi_i^2 / n_{\text{d.o.f.}}$ where the denominator is the number of degrees of freedom.

2) To ensure the consistency between the fit results, we multiply the error by $\sqrt{\tilde{\chi}_i^2}$.

3) The final result is the average of the interpolated cross sections, weighted by the rescaled fit error like

$$\sigma = \frac{\sum\limits_i w_i \cdot \sigma_i}{\sum\limits_i w_i} \text{ with } w_i = \frac{1}{\varepsilon_i^2}. \tag{B.1}$$

We follow the same procedure to estimate the reference cross sections in $2.5 < y < 4.0$, as a function of p_{T} and rapidity.

We can identify two types of uncertainty. The first one must reflect the uncertainties of the experimental measurements considered. These uncertainties are propagated to the

---

[†] In reality, the production cross section only starts from $\sqrt{s} = m_{\Upsilon}c^2 \sim 10$ GeV, i.e. two orders of magnitude below the LHC energy scale.

errors returned by the fitting functions. Thus, the associated uncertainty can be calculated as the mean of the rescaled fit errors, assuming that the measured cross sections are not correlated with the centre-of-mass energy. The second uncertainty originates from the choice of parametrisations and is taken as the maximum difference between the averaged cross section and each interpolation result. We add the two uncertainties in quadrature.

B.1.2 Integrated results

To estimate the cross sections integrated over $p_{\mathrm{T}} < 15$ GeV/c in $2.5 < y < 4.0$, the LHCb points have first to match the ALICE acceptance. The measurements at 2.76 TeV are extracted from this table. For the 7 and 8 TeV data, we have to sum up all the double-differential cross sections tabulated here, within our kinematic ranges. The 13 TeV points are calculated as the average of the measurements in rapidity intervals. All these intermediate results are provided in Table B.1.

$\sqrt{s}$ [TeV]	Υ(1S)	Υ(2S)	Υ(3S)	Υ(2S)/Υ(1S)
2.76	448 ± 24	106 ± 10	59 ± 8	0.237 ± 0.023
7	1090 ± 36	269 ± 9.2	132 ± 4.6	0.243 ± 0.004
8	1359 ± 41	339 ± 11	160 ± 5.0	0.245 ± 0.004
13	1958 ± 129	472 ± 31	234 ± 16	0.241 ± 0.002

Table B.1: Rapidity-differential cross sections (in pb) of LHCb measurements within $2.5 < y < 4.0$ integrated over $p_{\mathrm{T}} < 15$ GeV/c. The quoted uncertainty is the quadratic sum of the statistical and systematic uncertainties of these measurements.

Next, we can compute the weighted averages of ALICE and LHCb measurements to obtain the points at 7 and 8 TeV. Data used for the interpolation of the integrated cross sections are reported in Table B.2. Following the Procedure, we fit the data points to evaluate the cross sections at $\sqrt{s} = 5.02$ TeV. The results from each function shown in Figure B.1 are listed in Table B.3. The logarithmic parametrisation systematically gives the maximum difference with the weighted average of the integrated cross sections.

$\sqrt{s}$ [TeV]	Υ(1S)	Υ(2S)	Υ(3S)
2.76	448 ± 24	106 ± 10	59 ± 8
5.02	752 ± 85	288 ± 47	71 ± 35
7	1079 ± 35	268 ± 9.1	132 ± 4.6
8	1349 ± 39	339 ± 10	159 ± 5.0
13	1958 ± 129	472 ± 31	234 ± 16

Table B.2: Rapidity-differential cross sections (in pb) within $2.5 < y < 4.0$.

For the Υ(2S)-to-Υ(1S) cross-section ratio, we only consider the LHCb data points reported in Table B.1. As the masses are very close, one does not expect a strong dependence of the ratio with the centre-of-mass energy. We thus apply a constant, a linear and a logarithmic function. The interpolation results can be found in Figure B.2.

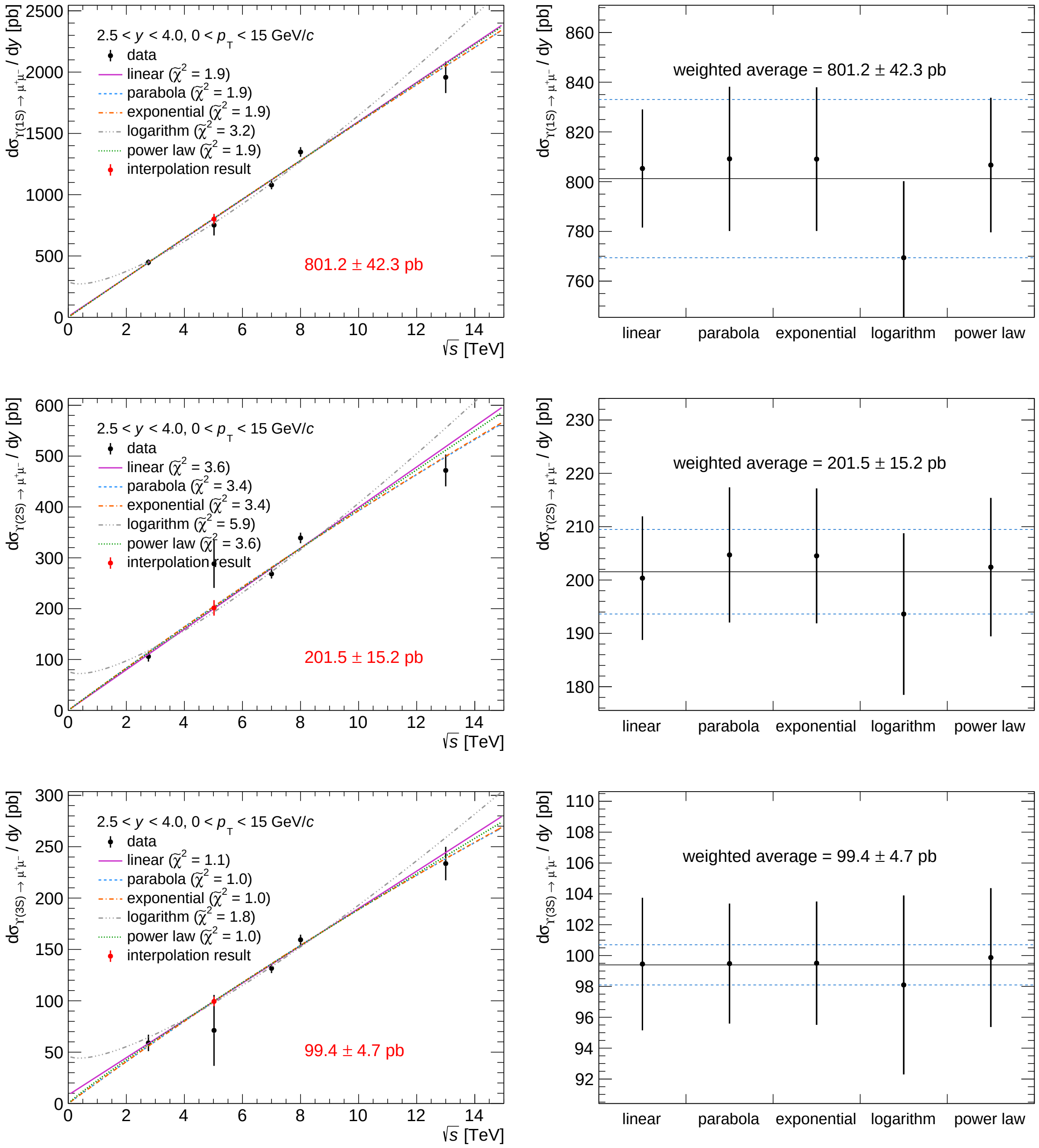

Figure B.1: Rapidity-differential cross section of (top) Υ(1S), (middle) Υ(2S) and (bottom) Υ(3S) production in $2.5 < y < 4.0$, integrated over $p_{\mathrm{T}} < 15$ GeV/c. The left column shows the measurements as a function of the centre-of-mass energy, fitted by the parametrisations listed in the legend. The red point corresponds to the weighted average of the interpolated cross sections as defined by the equation B.1. The distributions of the individual fit results are represented in the right column. The error bars denote the rescaled fit errors. The black solid line is the central value of the final result while the blue dashed lines are the maximum difference between the weighted average and the interpolated cross sections.

Function	$\Upsilon(1S)$	$\Upsilon(2S)$	$\Upsilon(3S)$
Linear	805.3 ± 23.7	200.3 ± 11.6	99.5 ± 4.3
Parabola	809.2 ± 29.0	204.7 ± 12.6	99.5 ± 3.9
Exponential	809.1 ± 28.9	204.5 ± 12.6	99.5 ± 4.0
Logarithm	769.4 ± 30.8	193.6 ± 15.1	98.1 ± 4.3
Power law	806.7 ± 19.6	202.4 ± 13.0	99.9 ± 4.5
Final result	801.2 ± 42.3	201.5 ± 15.2	99.4 ± 4.7

Table B.3: Interpolation results of the cross sections (in pb) in $2.5 < y < 4.0$ and integrated over $p_{\mathrm{T}} < 15$ GeV$/c$. For each function, the uncertainty corresponds to the rescaled fit error. The final result is the weighted average of the individual results, cf. equation B.1, and the uncertainty is the quadratic sum of the mean of the rescaled fit errors, and the maximum difference between the averaged cross section and each interpolation result.

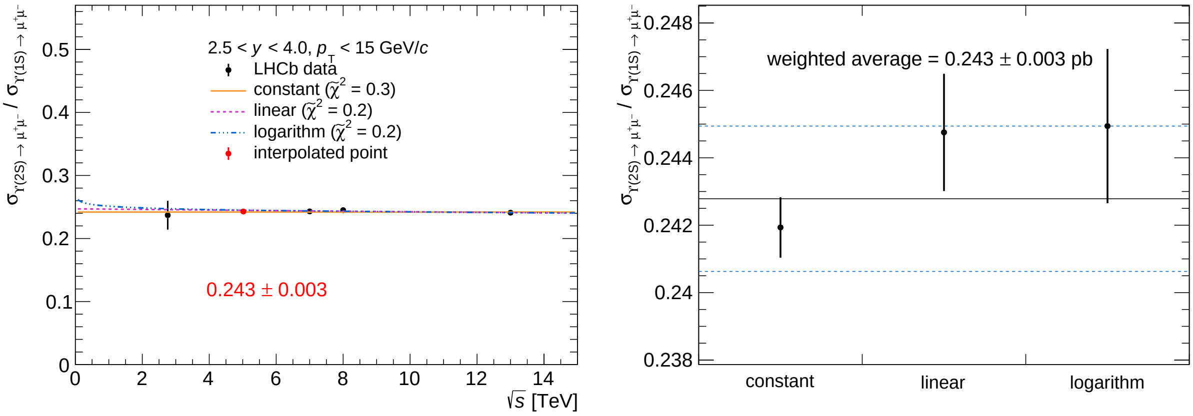

Figure B.2: $\Upsilon(2S)$-to-$\Upsilon(1S)$ cross-section ratio in the $2.5 < y < 4.0$ and $p_{\mathrm{T}} < 15$ GeV$/c$ intervals. The left panel shows the measurements as a function of the centre-of-mass energy, fitted by the parametrisations listed in the legend. The red point corresponds to the weighted average of the interpolated ratios as defined by the equation B.1. The distributions of the individual fit results are represented in the right column. The error bars denote the rescaled fit errors. The black solid line is the central value of the final result while the blue dashed lines are the maximum difference between the weighted average and the interpolated cross-section ratios.

B.1.3 Rapidity-differential cross sections

Up to now, forward Υ production in pp collisions has only been measured in rapidity intervals of 0.5 unit wide. The interpolation of rapidity-differential cross sections in narrower ranges is a two-step operation. First, we estimate the differential cross sections for each interval in $2.0 < y < 4.5$ via the Procedure. The second step, described in Section B.2, consists of integrating the rapidity dependence over the studied ranges.

LHCb measurements at 2.76 and 13 TeV are already integrated over $p_{\mathrm{T}} < 15$ GeV/c. For the 7 and 8 TeV data points, we have to sum up all the double-differential cross sections from $p_{\mathrm{T}} = 0$ to 15 GeV/c, for each rapidity interval.

Υ(1S)

The sums of double-differential cross sections for Υ(1S) are calculated from the tables for the 7 and 8 TeV data. All the numerical values are reported in Table B.4. Given the uncertainties of ALICE measurements, the averaged results are similar to LHCb values. The interpolation results displayed in Figure B.3 are tabulated in Table B.5. Without data points at $\sqrt{s} = 5.02$ TeV, the curvature of the function is poorly constrained. The interpolated cross section in the $2.0 < y < 2.5$ interval suffers from a large uncertainty and will be discarded in the following.

$\sqrt{s}$ [TeV]	$2.0 < y < 2.5$	$2.5 < y < 3.0$	$3.0 < y < 3.5$	$3.5 < y < 4.0$	$4.0 < y < 4.5$
2.76	808 ± 81	642 ± 43	454 ± 31	248 ± 24	70 ± 16
7	1191 ± 42	1274 ± 42	1117 ± 36	863 ± 29	461 ± 17
8	1759 ± 53	1659 ± 49	1371 ± 40	1048 ± 31	583 ± 18
13	2423 ± 152	2247 ± 139	1984 ± 127	1642 ± 119	1078 ± 105

Table B.4: Υ(1S) rapidity-differential cross sections (in pb) of LHCb measurements integrated over $p_{\mathrm{T}} < 15$ GeV/c. The quoted uncertainty is the quadratic sum of the statistical and systematic uncertainties of these measurements.

Function	$2.0 < y < 2.5$	$2.5 < y < 3.0$	$3.0 < y < 3.5$	$3.5 < y < 4.0$	$4.0 < y < 4.5$
Linear	1040 ± 183	1021 ± 68	823 ± 28	580 ± 15	284 ± 8
Parabola	983 ± 171	1028 ± 82	831 ± 32	572 ± 41	260 ± 32
Exponential	984 ± 176	1031 ± 85	831 ± 32	578 ± 41	280 ± 35
Logarithm	1023 ± 176	989 ± 78	788 ± 44	584 ± 30	264 ± 8
Power law	1015 ± 211	1033 ± 78	827 ± 32	568 ± 30	264 ± 24
Final result	1008 ± 186	1020 ± 84	823 ± 48	573 ± 40	274 ± 25

Table B.5: Interpolation of Υ(1S) rapidity-differential cross sections (in pb) integrated over $p_{\mathrm{T}} < 15$ GeV/c. For each function, the uncertainty corresponds to the rescaled fit error. The final result is the weighted average of the individual results, cf. equation B.1, and the uncertainty is the quadratic sum of the mean of the rescaled fit errors, and the maximum difference between the averaged cross section and each interpolation result.

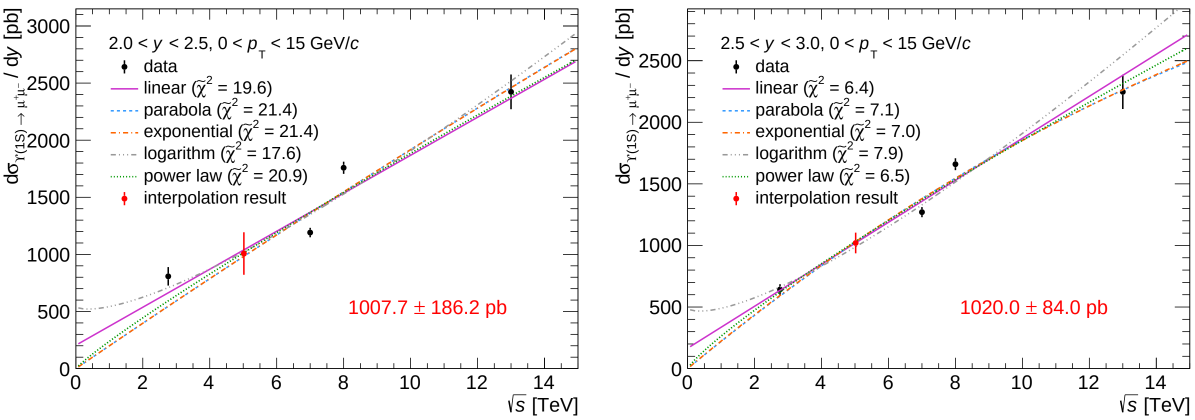

(a) $2.0 < y < 2.5$ (b) $2.5 < y < 3.0$

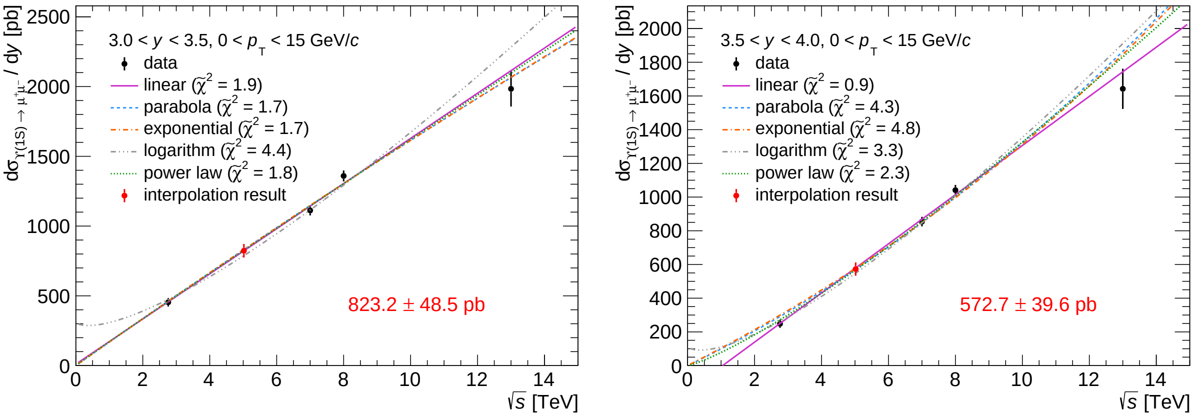

(c) $3.0 < y < 3.5$ (d) $3.5 < y < 4.0$

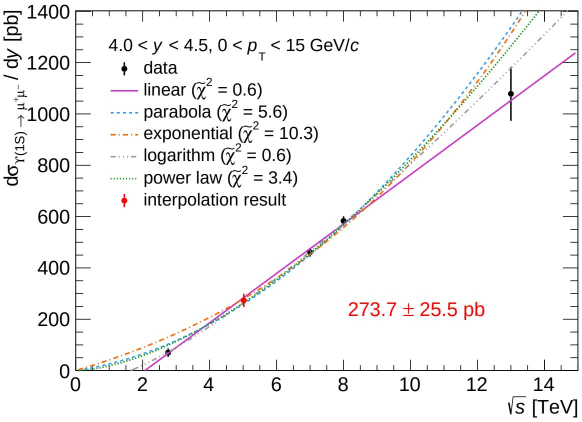

(e) $4.0 < y < 4.5$

Figure B.3: Interpolation of $\Upsilon(1S)$ rapidity-differential cross section integrated over $p_{\mathrm{T}} < 15$ GeV/c. Each panel shows the measurements as a function of the centre-of-mass energy, fitted by the parametrisations listed in the legend. The red point corresponds to the weighted average of the interpolated cross sections as defined by the equation B.1.

Υ(2S)

The rapidity-differential cross section of Υ(2S) is interpolated from LHCb measurements only. The data can be found in Table B.6. The interpolation results are given in Table B.7 and shown in Figure B.4. As for Υ(1S), we discard the $2.0 < y < 2.5$ interval.

$\sqrt{s}$ [TeV]	$2.5 < y < 3.0$	$3.0 < y < 3.5$	$3.5 < y < 4.0$	$4.0 < y < 4.5$
2.76	172 ± 22	100 ± 15	50 ± 10	2 ± 6.3
7	306 ± 11	274 ± 9.3	215 ± 7.9	115 ± 5.0
8	416 ± 13	340 ± 11	261 ± 8.4	145 ± 5.2
13	542 ± 34	478 ± 31	396 ± 29	258 ± 26

Table B.6: Υ(2S) rapidity-differential cross sections (in pb) of LHCb measurements integrated over $p_{\mathrm{T}} < 15$ GeV/c. The quoted uncertainty is the quadratic sum of the statistical and systematic uncertainties of these measurements.

Function	$2.5 < y < 3.0$	$3.0 < y < 3.5$	$3.5 < y < 4.0$	$4.0 < y < 4.5$
Linear	254 ± 33	200 ± 14	141 ± 8.1	63 ± 2.2
Parabola	249 ± 29	206 ± 13	147 ± 16	64 ± 15
Exponential	250 ± 30	206 ± 13	149 ± 14	71 ± 13
Logarithm	253 ± 35	196 ± 21	135 ± 15	59 ± 5.8
Power law	254 ± 35	203 ± 15	143 ± 13	65 ± 11
Final result	251 ± 32	203 ± 16	142 ± 15	63 ± 12

Table B.7: Interpolation of Υ(2S) rapidity-differential cross sections (in pb) integrated over $p_{\mathrm{T}} < 15$ GeV/c. For each function, the uncertainty corresponds to the rescaled fit error. The final result is the weighted average of the individual results, cf. equation B.1, and the uncertainty is the quadratic sum of the mean of the rescaled fit errors, and the maximum difference between the averaged cross section and each interpolation result.

B.1.4 Double-differential cross sections

We now turn to the differential cross sections in p_{T} intervals. For $\sqrt{s} = 2.76$ TeV, the LHCb collaboration reports the measurement as a function of p_{T} within the rapidity acceptance of the experiment. The ranges do not match those of the Pb–Pb analysis but can still be exploited. Figure B.5 shows the p_{T} spectra normalised to the size of the p_{T} and rapidity intervals. We fit the points with a function then integrate over the ranges of interest.

The LHCb data points at 7, 8 and 13 TeV are estimated as the averages of double-differential cross sections within $2.5 < y < 4.0$, for each p_{T} interval. All the numerical values for the interpolation are reported in Table B.8. The results are given in Table B.9 and displayed in Figure B.6. Even though the data points for the two higher p_{T} ranges at 2.76 TeV have large uncertainties, it is important to have at least four points to constrain the fit.

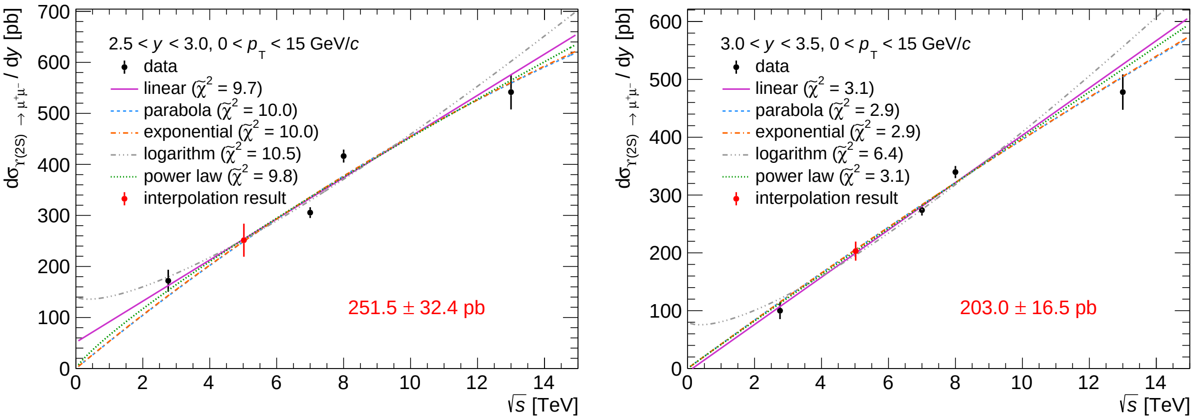

(a) $2.5 < y < 3.0$ (b) $3.0 < y < 3.5$

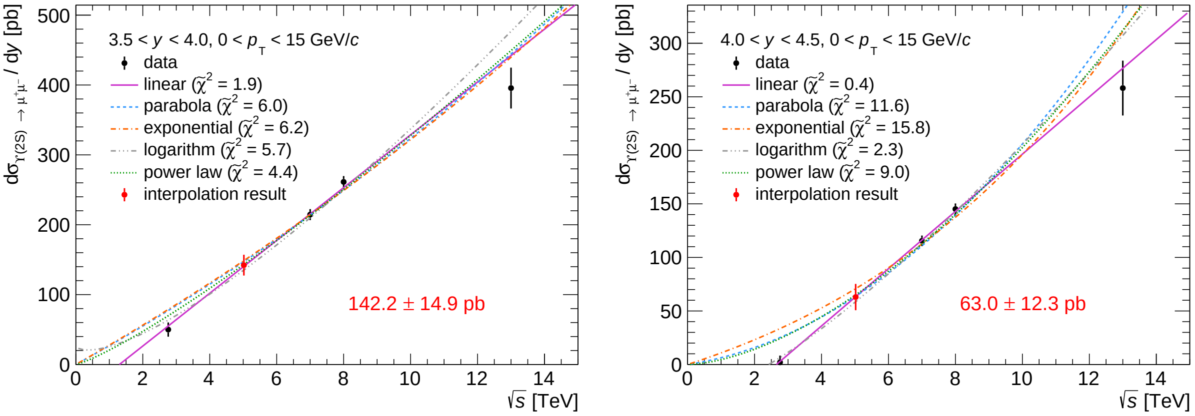

(c) $3.5 < y < 4.0$ (d) $4.0 < y < 4.5$

Figure B.4: Interpolation of $\Upsilon(2S)$ rapidity-differential cross section integrated over $p_T < 15$ GeV/c. Each panel shows the measurements as a function of the centre-of-mass energy, fitted by the parametrisations listed in the legend. The red point corresponds to the weighted average of the interpolated cross sections as defined by the equation B.1.

$\sqrt{s}$ [TeV]	$0 < p_T < 2$	$2 < p_T < 4$	$4 < p_T < 6$	$6 < p_T < 9$	$9 < p_T < 15$
2.76	51 ± 4.7	64 ± 5.4	55.4 ± 5.3	23.1 ± 7.0	5.4 ± 3.6
5.02	53 ± 13	133 ± 21	113 ± 18	–	–
7	92 ± 2.9	166 ± 4.4	128 ± 4.2	67.9 ± 2.3	18.3 ± 0.7
8	112 ± 3.7	203 ± 6.0	160 ± 4.8	86.3 ± 2.6	24.6 ± 0.8
13	146 ± 12	275 ± 19	231 ± 16	134 ± 9.3	41.9 ± 3.1

Table B.8: Double-differential cross sections (in pb) of $\Upsilon(1S)$ within $2.5 < y < 4.0$ in p_T intervals (in GeV/c).

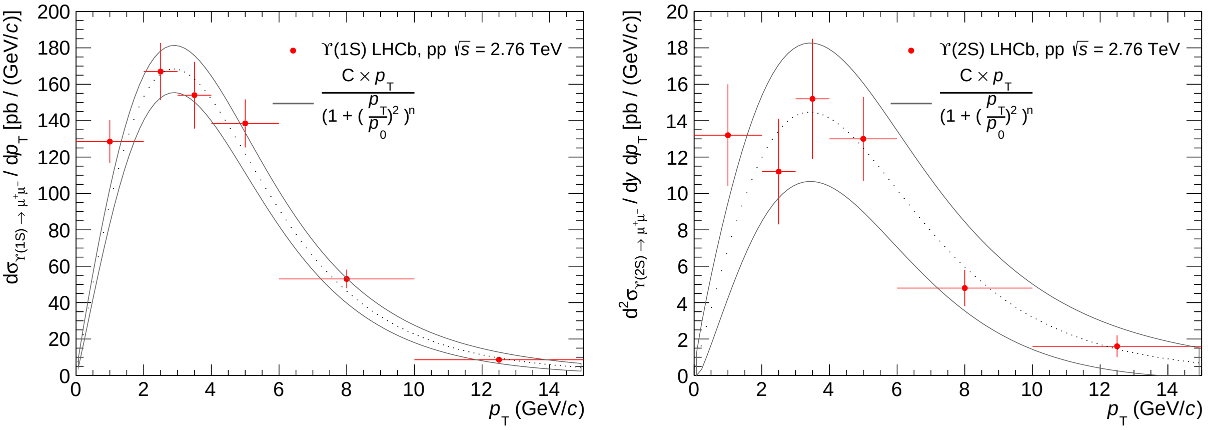

Figure B.5: Double-differential cross section of (left) $\Upsilon(1S)$ and (right) $\Upsilon(2S)$ production at $\sqrt{s} = 2.76$ TeV as a function of p_T. The red points are the LHCb measurements with vertical error bars corresponding to the quadratic sum of the statistical and systematic uncertainties. The grey band represents the fit of the p_T spectrum with the function written in the legend. The dotted curve is the central value obtained from the fit while the two solid lines delimit the error band.

Function	$0 < p_T < 2$	$2 < p_T < 4$	$4 < p_T < 6$	$6 < p_T < 9$	$9 < p_T < 15$
Linear	74.1 ± 4.1	121 ± 5.2	97.4 ± 4.4	47.7 ± 4.4	11.3 ± 2.0
Parabola	73.5 ± 4.6	124 ± 5.5	98.1 ± 4.7	49.7 ± 3.5	12.8 ± 1.4
Exponential	74.1 ± 4.9	124 ± 5.5	98.1 ± 4.8	49.8 ± 3.3	13.0 ± 1.2
Logarithm	73.0 ± 4.8	117 ± 7.6	94.5 ± 5.6	48.4 ± 5.2	11.9 ± 1.9
Power law	75.0 ± 4.5	122 ± 5.7	98.0 ± 4.9	48.7 ± 3.9	12.3 ± 1.4
Final result	74.0 ± 4.7	122 ± 7.7	97.4 ± 5.6	49.1 ± 4.3	12.5 ± 2.0

Table B.9: Interpolation of $\Upsilon(1S)$ double-differential cross sections (in pb) within $2.5 < y < 4.0$ in p_T intervals (in GeV/c). For each function, the uncertainty corresponds to the rescaled fit error. The final result is the weighted average of the individual results, cf. equation B.1, and the uncertainty is the quadratic sum of the mean of the rescaled fit errors, and the maximum difference between the averaged cross section and each interpolation result.

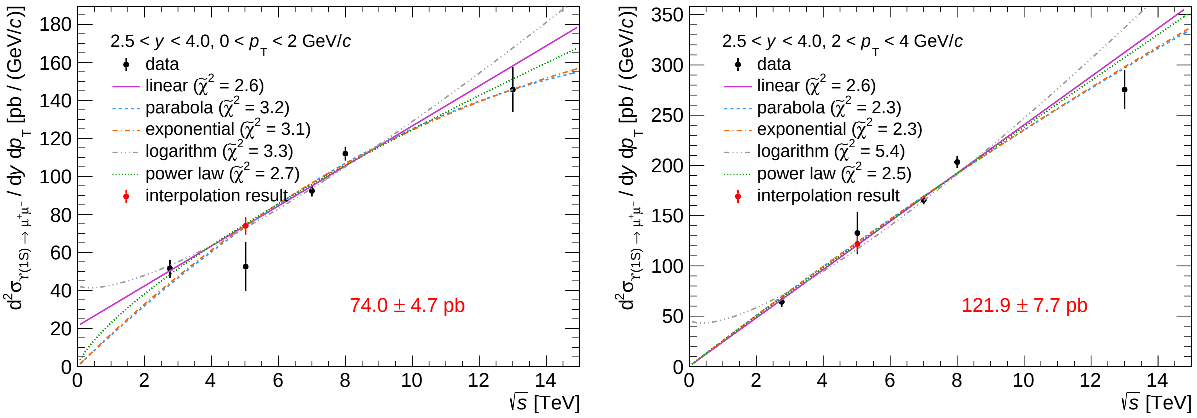

(a) $0 < p_{\mathrm{T}} < 2$ GeV/c

(b) $2 < p_{\mathrm{T}} < 4$ GeV/c

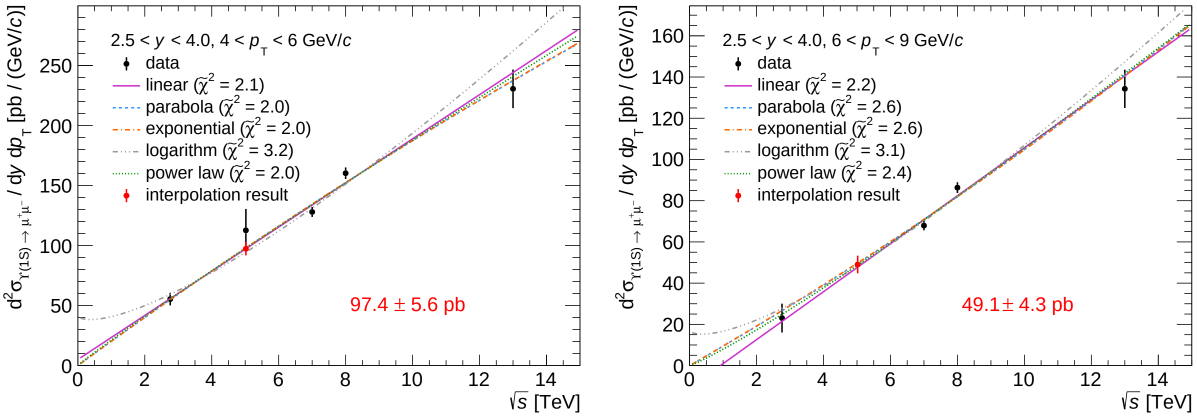

(c) $4 < p_{\mathrm{T}} < 6$ GeV/c

(d) $6 < p_{\mathrm{T}} < 9$ GeV/c

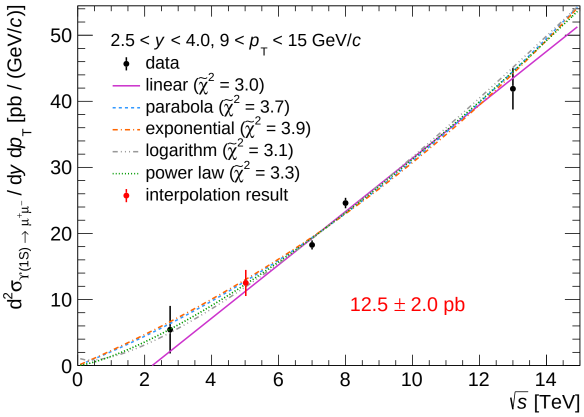

(e) $9 < p_{\mathrm{T}} < 15$ GeV/c

Figure B.6: Interpolation of $\Upsilon(1S)$ double-differential cross section within $2.5 < y < 4.0$ in p_{T} intervals. Each panel shows the measurements as a function of the centre-of-mass energy, fitted by the parametrisations listed in the legend. The red point corresponds to the weighted average of the interpolated cross sections as defined by the equation B.1.

B.2 Rapidity interpolation

After interpolating the Rapidity-differential cross sections in intervals of 0.5 unit wide, still at $\sqrt{s} = 5.02$ TeV, we aim to estimate the cross sections in ranges matching the Pb–Pb analysis. This requires a further interpolation procedure discussed hereafter.

B.2.1 Procedure

For this interpolation, we adopt a strategy similar to the ALICE's one for the determination of J/ψ reference cross sections for p–Pb studies [94]. The purpose is to assess the rapidity dependence of the y-differential measurements. It can studied from Figure 4.2. The production is maximum at midrapidity and decreases towards zero going at forward rapidity. We will include the CMS measurements [72] in order to constrain the dependence down to $y = 0$. The cross sections were not evaluated in $2.0 < y < 2.5$ on purpose since the CMS and LHCb acceptances partially overlap.

With so many points, such rapidity distribution can be interpolated by functions like a

- parabola: $a - b \times y^2$
- 3rd order polynomial: $a + b \times y + c \times y^2 + d \times y^3$
- hyperbolic tangent: $a \times (1 - \tanh(b \times y + c))$.

By construction, the parabola is symmetrical and reaches a global maximum in zero. The number of free parameters in a third-order polynomial enables to reproduce well the distribution. Without measurement point beyond $y = 4.5$, these two functions will extrapolate so that the differential cross section tends quickly towards 0, and even below. The hyperbolic tangent ensures the positivity of the cross section while describing the rapidity shape. A gaussian parametrisation, meeting all the properties mentioned previously, was tested but gave unreliable results.

The steps of the procedure are similar to the one for the energy interpolation. Each function is fitted on the data points as shown in Figure B.7. Then, we integrate the functions over the range of interest. The results are divided by the width of the rapidity interval to get the differential cross sections. As in the energy interpolation procedure, the final result is the weighted average of the interpolated cross sections, cf. equation B.1. Note that we do not rescale the fit error here. The total uncertainty is the quadratic sum of the average of data uncertainties propagated through the integral and the maximum difference between the averaged cross section and each interpolation result.

B.2.2 Υ(1S)

The CMS data points are extracted from the table. The y-differential cross sections of Υ(1S) in narrow rapidity intervals are reported in Table B.10.

B.2.3 Υ(2S)

The CMS data are extracted from the table. The y-differential cross sections of Υ(2S) in rapidity intervals are reported in Table B.11.

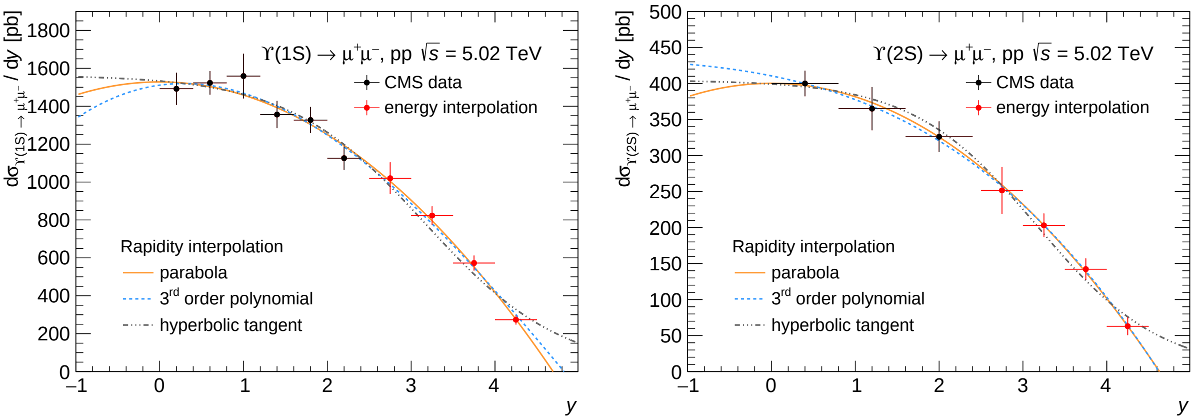

(a) $\Upsilon(1S)$ (b) $\Upsilon(2S)$

Figure B.7: Interpolation of the rapidity dependence of the y-differential cross sections at $\sqrt{s} = 5.02$ TeV. The black points are the CMS measurements [72] while the red points correspond to the results of the energy interpolation in Section B.1.3. The vertical error bars denote the quadratic sum of the statistical and systematic uncertainties of the data points.

Function	2.5–2.8	2.8–3.1	3.1–3.3	3.3–3.6	3.6–4.0
Parabola	1041 ± 36	924 ± 43	818 ± 51	702 ± 60	526 ± 75
3rd order polynomial	1026 ± 57	907 ± 65	801 ± 70	689 ± 71	524 ± 73
Hyperbolic tangent	1021 ± 55	885 ± 56	766 ± 58	648 ± 60	494 ± 65
Final result	1033 ± 51	909 ± 60	796 ± 67	679 ± 71	513 ± 73

Table B.10: Interpolation of $\Upsilon(1S)$ rapidity-differential cross sections (in pb) integrated over $p_T < 15$ GeV$/c$. The final result is the average of the individual results, cf. equation B.1, and the uncertainty is the quadratic sum of the averaged integral uncertainties and the maximum difference between the averaged cross section and each interpolation result.

Function	2.5–3.3	3.3–4.0
Parabola	242 ± 13	151 ± 20
3rd order polynomial	241 ± 22	152 ± 22
Hyperbolic tangent	238 ± 22	140 ± 19
Final result	241 ± 20	147 ± 21

Table B.11: Interpolation of $\Upsilon(2S)$ rapidity-differential cross sections (in pb) integrated over $p_T < 15$ GeV$/c$. The final result is the average of the individual results, cf. equation B.1, and the uncertainty is the quadratic sum of the averaged integral uncertainties and the maximum difference between the averaged cross section and each interpolation result.

Bibliography

[1] Particle Data Group collaboration, *Review of Particle Physics*, PTEP 2020 (2020) 8 p. 083C01. Cited on pages 1, 4, 28, 38, and 50.

[2] B. Pontecorvo, *Neutrino Experiments and the Problem of Conservation of Leptonic Charge*, Sov. Phys. JETP 26 (1968) p. 984–988. Available here. Cited on page 1.

[3] M. E. Peskin and D. V. Schroeder, *An Introduction to quantum field theory.* Addison-Wesley, Reading, USA, 1995. Cited on page 2.

[4] S. Weinberg, *A Model of Leptons*, Phys. Rev. Lett. 19 (1967) p. 1264–1266. Cited on page 2.

[5] F. Englert and R. Brout, *Broken Symmetry and the Mass of Gauge Vector Mesons*, Phys. Rev. Lett. 13 (1964) p. 321–323. Cited on page 2.

[6] P. W. Higgs, *Spontaneous Symmetry Breakdown without Massless Bosons*, Phys. Rev. 145 (1966) p. 1156–1163. Cited on page 2.

[7] J. Beacham et al., *Physics Beyond Colliders at CERN: Beyond the Standard Model Working Group Report*, J. Phys. G 47 (2020) 1 p. 010501, `arXiv:1901.09966 [hep-ex]`. Cited on page 2.

[8] Flavour Lattice Averaging Group collaboration, *FLAG Review 2019: Flavour Lattice Averaging Group (FLAG)*, Eur. Phys. J. C 80 (2020) 2 p. 113, `arXiv:1902.08191 [hep-lat]`. Cited on page 3.

[9] D. J. Gross and F. Wilczek, *Ultraviolet Behavior of Nonabelian Gauge Theories*, Phys. Rev. Lett. 30 (1973) p. 1343–1346. Cited on page 3.

[10] H. Politzer, *Reliable Perturbative Results for Strong Interactions?*, Phys. Rev. Lett. 30 (1973) p. 1346–1349. Cited on page 3.

[11] A. Jaffe and E. Witten, *Quantum Yang-Mills theory.* Description of the Millenium Problem on the existence of the Yang-Mills theory and a mass gap. Cited on page 3.

[12] C. Gattringer and C. B. Lang, *Quantum chromodynamics on the lattice*, vol. 788. Springer, Berlin, 2010. Cited on page 3.

[13] Z. Fodor and C. Hoelbling, *Light Hadron Masses from Lattice QCD*, Rev. Mod. Phys. 84 (2012) p. 449, `arXiv:1203.4789 [hep-lat]`. Cited on page 4.

[14] J. C. Collins and M. Perry, *Superdense Matter: Neutrons Or Asymptotically Free Quarks?*, Phys. Rev. Lett. 34 (1975) p. 1353. Cited on page 5.

[15] N. Cabibbo and G. Parisi, *Exponential Hadronic Spectrum and Quark Liberation*, Phys. Lett. B 59 (1975) p. 67–69. Cited on page 5.

[16] HotQCD collaboration, *Equation of state in (2+1)-flavor QCD*, Phys. Rev. D 90 (2014) p. 094503, `arXiv:1407.6387 [hep-lat]`. Cited on page 5.

[17] W. Busza, K. Rajagopal, and W. van der Schee, *Heavy Ion Collisions: The Big Picture, and the Big Questions*, Ann. Rev. Nucl. Part. Sci. 68 (2018) p. 339–376, `arXiv:1802.04801 [hep-ph]`. Cited on page 5.

[18] J. Bjorken, *Highly Relativistic Nucleus-Nucleus Collisions: The Central Rapidity Region*, Phys. Rev. D 27 (1983) p. 140–151. Cited on page 5.

[19] U. Heinz and R. Snellings, *Collective flow and viscosity in relativistic heavy-ion collisions*, Ann. Rev. Nucl. Part. Sci. 63 (2013) p. 123–151, `arXiv:1301.2826 [nucl-th]`. Cited on page 6.

[20] P. Braun-Munzinger, V. Koch, T. Schäfer, and J. Stachel, *Properties of hot and dense matter from relativistic heavy ion collisions*, Phys. Rept. 621 (2016) p. 76–126, `arXiv:1510.00442 [nucl-th]`. Cited on page 6.

[21] A. Andronic, P. Braun-Munzinger, K. Redlich, and J. Stachel, *Decoding the phase structure of QCD via particle production at high energy*, Nature 561 (2018) 7723 p. 321–330, `arXiv:1710.09425 [nucl-th]`. Cited on pages 6, 7, 62, and 63.

[22] L. Evans and P. Bryant, *LHC Machine*, JINST 3 (2008) p. S08001. Cited on page 9.

[23] J. M. Jowett and M. Schaumann, *Overview of heavy ions in LHC Run 2.* Proceeding for the 9th LHC Operations Evian Workshop, 2019. Cited on page 11.

[24] ATLAS collaboration, *The ATLAS Experiment at the CERN Large Hadron Collider*, JINST 3 (2008) p. S08003. Cited on page 11.

[25] CMS collaboration, *The CMS Experiment at the CERN LHC*, JINST 3 (2008) p. S08004. Cited on page 11.

[26] ATLAS collaboration, *Overview of Heavy Ions from the ATLAS Experiment*, Acta Phys. Polon. B 50 (2019) p. 1217–1228. Cited on page 11.

[27] CMS collaboration, *Review of results using heavy ion collisions at CMS*, in *Workshop of QCD and Forward Physics at the the LHC, the future Electron Ion Collider and Cosmic Ray Physics*, p. 11–22. University of Kansas Libraries, Lawrence, 2020. `arXiv:2006.05556 [nucl-ex]`. Cited on page 11.

[28] LHCb collaboration, *The LHCb Detector at the LHC*, JINST 3 (2008) p. S08005. Cited on page 11.

[29] LHCb collaboration, *First Measurement of Charm Production in its Fixed-Target Configuration at the LHC*, Phys. Rev. Lett. 122 (2019) 13 p. 132002, `arXiv:1810.07907 [hep-ex]`. Cited on page 11.

[30] TOTEM collaboration, *The TOTEM experiment at the CERN Large Hadron Collider*, JINST 3 (2008) p. S08007. Cited on page 11.

[31] LHCf collaboration, *The LHCf detector at the CERN Large Hadron Collider*, JINST 3 (2008) p. S08006. Cited on page 11.

[32] MoEDAL collaboration, *Magnetic Monopole Search with the Full MoEDAL Trapping Detector in 13 TeV pp Collisions Interpreted in Photon-Fusion and Drell-Yan Production*, Phys. Rev. Lett. 123 (2019) 2 p. 021802, `arXiv:1903.08491 [hep-ex]`. Cited on page 11.

[33] FASER collaboration, *FASER: ForwArd Search ExpeRiment at the LHC*, `arXiv:1901.04468 [hep-ex]`. Cited on page 11.

[34] FASER collaboration, *Detecting and Studying High-Energy Collider Neutrinos with FASER at the LHC*, Eur. Phys. J. C 80 (2020) 1 p. 61, `arXiv:1908.02310 [hep-ex]`. Cited on page 11.

[35] ALICE collaboration, *The ALICE experiment at the CERN LHC*, JINST 3 (2008) p. S08002. Cited on pages 12 and 14.

[36] ALICE collaboration, *Performance of the ALICE Experiment at the CERN LHC*, Int. J. Mod. Phys. A 29 (2014) p. 1430044, `arXiv:1402.4476 [nucl-ex]`. Cited on pages 12 and 16.

[37] ALICE collaboration, *Alignment of the ALICE Inner Tracking System with cosmic-ray tracks*, JINST 5 (2010) p. P03003, `arXiv:1001.0502 [physics.ins-det]`. Cited on page 13.

[38] ALICE collaboration, *ALICE technical design report on forward detectors: FMD, T0 and V0*, 2004. `https://cds.cern.ch/record/781854`. Cited on page 13.

[39] ALICE collaboration, *Performance of the ALICE VZERO system*, JINST 8 (2013) p. P10016, `arXiv:1306.3130 [nucl-ex]`. Cited on pages 13 and 22.

[40] ALICE collaboration, *ALICE Zero-Degree Calorimeter (ZDC): Technical Design Report*, 1999. `https://cds.cern.ch/record/381433`. Cited on page 13.

[41] ALICE collaboration, *ALICE dimuon forward spectrometer: Technical Design Report*, 1999. `https://edms.cern.ch/document/470838/1`. Cited on pages 13, 15, 16, and 17.

[42] ALICE collaboration, *ALICE dimuon forward spectrometer: addendum to the Technical Design Report*, 2000. `http://cds.cern.ch/record/494265`. Cited on page 13.

[43] ALICE collaboration, *Numerical Simulations and Offline Reconstruction of the Muon Spectrometer of ALICE*, 2009. `https://edms.cern.ch/document/1054937/1`. Cited on page 16.

[44] M. Tarhini, *Measurement of Z-boson and J/ψ Production in p-Pb and Pb-Pb Collisions at $\sqrt{s_{NN}}$ = 5.02 TeV with ALICE at the LHC*. PhD thesis, Université Paris-Saclay, 2017. `https://tel.archives-ouvertes.fr/tel-01691725`. Cited on pages 20 and 25.

[45] ALICE collaboration, *Centrality determination in heavy ion collisions*, Aug 2018. `https://cds.cern.ch/record/2636623`. Cited on pages 20, 21, and 56.

[46] M. L. Miller, K. Reygers, S. J. Sanders, and P. Steinberg, *Glauber modeling in high energy nuclear collisions*, Ann. Rev. Nucl. Part. Sci. 57 (2007) p. 205–243, `arXiv:nucl-ex/0701025`. Cited on page 20.

[47] ALICE collaboration, *Centrality dependence of the charged-particle multiplicity density at midrapidity in Pb-Pb collisions at $\sqrt{s_{\mathrm{NN}}}$ = 5.02 TeV*, Phys. Rev. Lett. 116 (2016) 22 p. 222302, `arXiv:1512.06104 [nucl-ex]`. Cited on page 20.

[48] V. Kumar, P. Shukla, and R. Vogt, *Components of the dilepton continuum in Pb+Pb collisions at $\sqrt{s_{NN}} = 2.76$ TeV*, Phys. Rev. C 86 (2012) p. 054907, `arXiv:1205.3860 [hep-ph]`. Cited on page 25.

[49] W. Verkerke and D. P. Kirkby, *The RooFit toolkit for data modeling*, eConf C0303241 (2003) p. MOLT007, `arXiv:physics/0306116`. Cited on page 26.

[50] R. Brun, F. Bruyant, F. Carminati, S. Giani, M. Maire, A. McPherson, G. Patrick, and L. Urban, *GEANT: Detector Description and Simulation Tool*. CERN Program Library. CERN, Geneva, 1993. `http://cds.cern.ch/record/1082634`. Long Writeup W5013. Cited on pages 31 and 39.

[51] GEANT4 collaboration, *GEANT4: A Simulation toolkit*, Nucl. Instrum. Meth. A 506 (2003) p. 250–303. Cited on page 31.

[52] ALICE collaboration, *Υ production in p-Pb collisions at $\sqrt{s_{\mathrm{NN}}} = 8.16$ TeV*, Phys. Lett. B 806 (2020) p. 135486, `arXiv:1910.14405 [nucl-ex]`. Cited on pages 32, 67, and 77.

[53] ALICE collaboration, *Quarkonium signal extraction in ALICE*, 2015. `https://cds.cern.ch/record/2060096`, accessed ALICE-PUBLIC-2015-006. Cited on page 34.

[54] G. J. Feldman and R. D. Cousins, *A Unified approach to the classical statistical analysis of small signals*, Phys. Rev. D 57 (1998) p. 3873–3889, `arXiv:physics/9711021`. Cited on page 38.

[55] V. Feuillard, *Measurement of the ψ(2S) production in presence of a Quark-Gluon Plasma*. PhD thesis, Université Clermont Auvergne, 2017. `https://hal-cea.archives-ouvertes.fr/tel-01682850`. Cited on page 38.

[56] CDF collaboration, Υ *Production and Polarization in $p\overline{p}$ Collisions at $\sqrt{s} = 1.8$ TeV*, Phys. Rev. Lett. 88 (Apr 2002) p. 161802. Cited on page 39.

[57] CMS collaboration, *Upsilon Production Cross-Section in pp Collisions at $\sqrt{s} = 7$ TeV*, Phys. Rev. D 83 (2011) p. 112004, `arXiv:1012.5545 [hep-ex]`. Cited on page 39.

[58] CMS collaboration, *Measurement of the $\Upsilon(1S), \Upsilon(2S)$ and $\Upsilon(3S)$ Polarizations in pp Collisions at $\sqrt{s} = 7$ TeV*, Phys. Rev. Lett. 110 (2013) 8 p. 081802, `arXiv:1209.2922 [hep-ex]`. Cited on page 39.

[59] LHCb collaboration, *Measurement of the Υ polarizations in pp collisions at $\sqrt{s} = 7$ and 8 TeV*, JHEP 12 (2017) p. 110, `arXiv:1709.01301 [hep-ex]`. Cited on page 39.

[60] D. Lange, *The EvtGen particle decay simulation package*, Nucl. Instrum. Meth. A 462 (2001) p. 152–155. Cited on page 39.

[61] P. Golonka and Z. Was, *PHOTOS Monte Carlo: A Precision tool for QED corrections in Z and W decays*, Eur. Phys. J. C 45 (2006) p. 97–107, `arXiv:hep-ph/0506026`. Cited on page 39.

[62] LHCb collaboration, *Measurement of Υ production in pp collisions at $\sqrt{s} = 13$ TeV*, JHEP 07 (2018) p. 134, `arXiv:1804.09214 [hep-ex]`. [Erratum: JHEP 05, 076 (2019)]. Cited on pages 42, 52, and 83.

[63] K. Eskola, V. Kolhinen, and C. Salgado, *The Scale dependent nuclear effects in parton distributions for practical applications*, Eur. Phys. J. C 9 (1999) p. 61–68, `arXiv:hep-ph/9807297`. Cited on page 42.

[64] K. Eskola, H. Paukkunen, and C. Salgado, *EPS09: A New Generation of NLO and LO Nuclear Parton Distribution Functions*, JHEP 04 (2009) p. 065, `arXiv:0902.4154 [hep-ph]`. Cited on page 42.

[65] B. Audurier, *Étude de la production inclusive de J/ψ dans les collisions pp et Pb-Pb à $\sqrt{s_{NN}} = 5.02$ TeV avec le spectromètre à muons de l'expérience ALICE au LHC.* PhD thesis, Université de Nantes (UNAM), 2017. `https://tel.archives-ouvertes.fr/tel-01970506`. Cited on pages 43, 47, and 57.

[66] O. Bugnon, *Muon tracking efficiency for LHC18q and LHC18r.* Presentation at the International ALICE Muon Workshop, April 2019. Figure included with the courtesy of the author. Cited on page 44.

[67] ALICE collaboration, *ALICE 2017 luminosity determination for pp collisions at $\sqrt{s} = 5$ TeV*, Nov 2018. `http://cds.cern.ch/record/2648933`. Cited on pages 48 and 50.

[68] ALICE collaboration, *Measurement of quarkonium production at forward rapidity in pp collisions at $\sqrt{s} = 7$ TeV*, Eur. Phys. J. C 74 (2014) 8 p. 2974, `arXiv:1403.3648 [nucl-ex]`. Cited on pages 52 and 83.

[69] ALICE collaboration, *Inclusive quarkonium production at forward rapidity in pp collisions at* $\sqrt{s} = 8$ *TeV*, Eur. Phys. J. C 76 (2016) 4 p. 184, `arXiv:1509.08258 [hep-ex]`. Cited on pages 52 and 83.

[70] LHCb collaboration, *Measurement of* Υ *production in pp collisions at* $\sqrt{s} = 2.76$ *TeV*, Eur. Phys. J. C 74 (2014) 4 p. 2835, `arXiv:1402.2539 [hep-ex]`. Cited on pages 52 and 83.

[71] LHCb collaboration, *Forward production of* Υ *mesons in pp collisions at* $\sqrt{s} = 7$ *and 8 TeV*, JHEP 11 (2015) p. 103, `arXiv:1509.02372 [hep-ex]`. Cited on pages 52 and 83.

[72] CMS collaboration, *Measurement of nuclear modification factors of* Υ*(1S),* Υ*(2S), and* Υ*(3S) mesons in PbPb collisions at* $\sqrt{s_{\mathrm{NN}}} = 5.02$ *TeV*, Phys. Lett. B 790 (2019) p. 270–293, `arXiv:1805.09215 [hep-ex]`. Cited on pages 52, 60, 70, 77, 94, and 95.

[73] V. Cheung and R. Vogt, *Production and polarization of prompt* $\Upsilon(nS)$ *in the improved color evaporation model using the* k_T*-factorization approach*, Phys. Rev. D 99 (2019) 3 p. 034007, `arXiv:1811.11570 [hep-ph]`. Cited on page 52.

[74] J.-P. Lansberg, H.-S. Shao, N. Yamanaka, Y.-J. Zhang, and C. Noûs, *Complete NLO QCD study of single- and double-quarkonium hadroproduction in the colour-evaporation model at the Tevatron and the LHC*, Phys. Lett. B 807 (2020) p. 135559, `arXiv:2004.14345 [hep-ph]`. Cited on page 53.

[75] P. Braun-Munzinger and J. Stachel, *(Non)thermal aspects of charmonium production and a new look at* J/ψ *suppression*, Phys. Lett. B 490 (2000) p. 196–202, `arXiv:nucl-th/0007059`. Cited on page 62.

[76] ALICE collaboration, J/ψ *suppression at forward rapidity in Pb-Pb collisions at* $\sqrt{s_{\mathrm{NN}}} = 5.02$ *TeV*, Phys. Lett. B 766 (2017) p. 212–224, `arXiv:1606.08197 [nucl-ex]`. Cited on page 66.

[77] ALICE collaboration, *Studies of* J/ψ *production at forward rapidity in Pb-Pb collisions at* $\sqrt{s_{\mathrm{NN}}} = 5.02$ *TeV*, JHEP 02 (2020) p. 041, `arXiv:1909.03158 [nucl-ex]`. Cited on pages 66, 68, and 77.

[78] ATLAS collaboration, *Measurement of quarkonium production in proton–lead and proton–proton collisions at 5.02 TeV with the ATLAS detector*, Eur. Phys. J. C 78 (2018) 3 p. 171, `arXiv:1709.03089 [nucl-ex]`. Cited on pages 67 and 77.

[79] LHCb collaboration, *Study of* Υ *production in pPb collisions at* $\sqrt{s_{\mathrm{NN}}} = 8.16$ *TeV*, JHEP 11 (2018) p. 194, `arXiv:1810.07655 [hep-ex]`. [Erratum: JHEP 02, 093 (2020)]. Cited on pages 67 and 77.

[80] Z. Citron et al., *Report from Working Group 5: Future physics opportunities for high-density QCD at the LHC with heavy-ion and proton beams*, CERN Yellow Rep. Monogr. 7 (2019) p. 1159–1410, `arXiv:1812.06772 [hep-ph]`. Cited on pages 69 and 78.

[81] CMS collaboration, *Suppression of Excited Υ States Relative to the Ground State in Pb-Pb Collisions at* $\sqrt{s_{\mathrm{NN}}}$*=5.02 TeV*, Phys. Rev. Lett. 120 (2018) 14 p. 142301, `arXiv:1706.05984 [hep-ex]`. Cited on page 70.

[82] E. G. Ferreiro and J.-P. Lansberg, *Is bottomonium suppression in proton-nucleus and nucleus-nucleus collisions at LHC energies due to the same effects?*, JHEP 10 (2018) p. 094, `arXiv:1804.04474 [hep-ph]`. [Erratum: JHEP 03, 063 (2019)]. Cited on pages 72, 73, and 74.

[83] K. Kovarik et al., *nCTEQ15 - Global analysis of nuclear parton distributions with uncertainties in the CTEQ framework*, Phys. Rev. D 93 (2016) 8 p. 085037, `arXiv:1509.00792 [hep-ph]`. Cited on page 72.

[84] B. Krouppa and M. Strickland, *Predictions for bottomonia suppression in 5.023 TeV Pb-Pb collisions*, Universe 2 (2016) 3 p. 16, `arXiv:1605.03561 [hep-ph]`. Cited on pages 72, 73, 74, and 75.

[85] X. Du, R. Rapp, and M. He, *Color Screening and Regeneration of Bottomonia in High-Energy Heavy-Ion Collisions*, Phys. Rev. C 96 (2017) 5 p. 054901, `arXiv:1706.08670 [hep-ph]`. Cited on pages 72, 73, and 74.

[86] X. Yao, W. Ke, Y. Xu, S. A. Bass, and B. Müller, *Coupled Boltzmann Transport Equations of Heavy Quarks and Quarkonia in Quark-Gluon Plasma*, JHEP 01 (2021) p. 046, `arXiv:2004.06746 [hep-ph]`. Cited on pages 72, 73, and 75.

[87] K. J. Eskola, P. Paakkinen, H. Paukkunen, and C. A. Salgado, *EPPS16: Nuclear parton distributions with LHC data*, Eur. Phys. J. C 77 (2017) 3 p. 163, `arXiv:1612.05741 [hep-ph]`. Cited on page 72.

[88] ALICE collaboration, *Analysis of the apparent nuclear modification in peripheral Pb–Pb collisions at 5.02 TeV*, Phys. Lett. B 793 (2019) p. 420–432, `arXiv:1805.05212 [nucl-ex]`. Cited on page 72.

[89] ALICE collaboration, *Υ production and nuclear modification at forward rapidity in Pb–Pb collisions at* $\sqrt{s_{\mathrm{NN}}} = 5.02$ *TeV*, Phys. Lett. B 822 (2021) p. 136579, `arXiv:2011.05758 [nucl-ex]`. Cited on page 77.

[90] F. Arleo and S. Peigné, *Quarkonium suppression in heavy-ion collisions from coherent energy loss in cold nuclear matter*, JHEP 10 (2014) p. 073, `arXiv:1407.5054 [hep-ph]`. Cited on page 77.

[91] A. Kusina, J.-P. Lansberg, I. Schienbein, and H.-S. Shao, *Gluon Shadowing in Heavy-Flavor Production at the LHC*, Phys. Rev. Lett. 121 (2018) 5 p. 052004, `arXiv:1712.07024 [hep-ph]`. Cited on page 78.

[92] K. J. Eskola, P. Paakkinen, and H. Paukkunen, *Non-quadratic improved Hessian PDF reweighting and application to CMS dijet measurements at 5.02 TeV*, Eur. Phys. J. C 79 (2019) 6 p. 511, `arXiv:1903.09832 [hep-ph]`. Cited on page 78.

[93] ALICE and LHCb collaboration, *Reference pp cross-sections for* $\Upsilon(1S)$ *studies in proton-lead collisions at* $\sqrt{s} = 5.02$ *TeV and comparisons between ALICE and LHCb results*, Aug 2014. `https://cds.cern.ch/record/1748460`. ALICE-PUBLIC-2014-002, LHCb-CONF-2014-003. Cited on page 84.

[94] ALICE and LHCb collaboration, *Reference pp cross-sections for* J/ψ *studies in proton-lead collisions at* $\sqrt{s} = 5.02$ *TeV and comparisons between ALICE and LHCb results*, Dec 2013. `https://cds.cern.ch/record/1639617`. LHCb-CONF-2013-013, ALICE-PUBLIC-2013-002. Cited on page 94.

UNIVERSITE / MATIERE
BRETAGNE \ MOLECULES
LOIRE / ET MATERIAUX

IMT Atlantique
Bretagne-Pays de la Loire
École Mines-Télécom

Titre : Mesure de la production des mésons Υ dans les collisions proton–proton et Pb–Pb à $\sqrt{s_{\mathrm{NN}}}$ = 5.02 TeV avec l'expérience ALICE au LHC

Mots clés : méson Υ, quarkonia, facteur de modification nucléaire, collisions d'ions lourds, plasma de quarks et de gluons, ALICE, LHC

Résumé : Les collisions d'ions lourds ultra-relativistes mène à l'émergence d'un état extrême de la matière, le plasma de quarks et de gluons ou QGP. Formés aux premiers instants de la collision, les quarkonia, resonances de deux quarks de même saveur lourde, interagissent avec le milieu tout au long de son évolution. Selon l'intensité des mécanismes en jeu, les paires sont dissociées et le taux de production est donc supprimé. La mesure de cette suppression offre un accès privilégié aux caractéristiques du QGP. En particulier, la production de quarkonia dans les collisions d'ions lourds est communément avancée comme une observable clé de la modification de l'interaction forte. Cette thèse porte sur l'étude de la production du méson Υ en collisions Pb–Pb à $\sqrt{s_{\mathrm{NN}}}$ = 5.02 TeV au LHC. Les mésons $\Upsilon(\mathrm{nS})$ sont reconstruits à travers leur désintégration en paire de muons détectés par le spectromètre à muon d'ALICE. Les résultats montrent une forte suppression de la production de $\Upsilon(1\mathrm{S})$, augmentant des collisions périphériques aux plus centrales. L'état excité $\Upsilon(2\mathrm{S})$ est pour la première fois mesuré à rapidité avant dans des collisions noyau–noyau. La comparison avec des predictions de modèles phénoménologiques permettent d'interpréter les mesures et de contraindre les mécanismes de suppression des quarkonia.

Title: Measurement of Υ-meson production in proton–proton and Pb–Pb collisions at $\sqrt{s_{\mathrm{NN}}}$ = 5.02 TeV with the ALICE experiment at the LHC

Keywords: Υ meson, quarkonia, nuclear modification factor, heavy-ion collisions, quark-gluon plasma, ALICE, LHC

Abstract: Ultrarelativistic heavy-ion collisions lead to the emergence of an extreme state of matter, the quark-gluon plasma or QGP. Formed at the early stage of the collision, quarkonia, resonances of two quarks of the same heavy flavour, interact with the medium throughout its evolution. Depending on the intensity of the mechanisms at play, the pairs are dissociated and the final-state production rate is thus suppressed. The measurement of this suppression offers a privileged access to QGP features. In particular, the production of quarkonia in heavy-ion collisions is commonly advertised as a key observable of the modification of the strong interaction. This thesis is devoted to the study of the Υ production in Pb–Pb collisions at $\sqrt{s_{\mathrm{NN}}}$ = 5.02 TeV at the LHC. The $\Upsilon(\mathrm{nS})$ mesons are reconstructed via their decay into muon pairs detected by the ALICE muon spectrometer. The results indicate a strong suppression of the $\Upsilon(1\mathrm{S})$ production, increasing from peripheral towards more central collisions. For the first time, the $\Upsilon(2\mathrm{S})$ excited state can be measured at forward rapidity in nucleus–nucleus collisions. The comparison with predictions by phenomenological models allows to interpret the measurements and to constrain the suppression mechanisms of quarkonia.